Economic, System, and Community-Based Optimization of Off-Grid Wave Energy Conversion

Trent Dillon

A dissertation

submitted in partial fulfillment of the

requirements for the degree of

Doctor of Philosophy

University of Washington
2023

Reading Committee:
Brian Polagye, Chair
Ben Maurer
Michelle DiBenedetto

Program Authorized to Offer Degree:
Mechanical Engineering

University of Washington

Abstract

Economic, System, and Community-Based Optimization of Off-Grid Wave Energy Conversion

Trent Dillon

Chair of the Supervisory Committee:

Professor Brian Polagye
Mechanical Engineering

The growing economic feasibility of renewable energy, caused in large part by the climate crisis, has expanded the number of locations in which humans can feasibly harness and use electricity. Wave energy, in particular, has the potential to power oceanographic measurements, remote communities, and other applications that may lack sufficient electricity due to limited grid access in ocean or coastal areas. However, as a relatively nascent renewable energy technology, less is known about the suitability and optimal characteristics of wave energy in off-grid applications. This thesis explores off-grid wave energy by focusing on its potential contributions to ocean observation, in which autonomous instrument packages can be powered by a wave energy converter (WEC) to collect information on metocean, biogeochemical, and ecological processes. Historically, constraints associated with battery-, vessel-, and cable-powered observations have limited the range, endurance, continuity, persistence and flexibility of these measurements, in turn restraining our understanding of marine ecosystems. This has driven decades of innovation to add "in-situ" power generation, such as wave energy, that enables new opportunities for ocean research. Aiding these efforts, this thesis presents optimization frameworks that simulate off-grid wave energy systems and identify cost-optimal system design, as well as potential enhancements that may improve the suitability of wave energy for ocean observation and, consequently, off-grid applications in general.

Chapter 1 describes the context of wave energy at a high level, including how the technology may be used at scales smaller than for megawatt-scale utility power, such as ocean observation. In Chapter 2, I

present a techno-economic model for powering ocean observation that compares the system characteristics and cost drivers of four battery-backed sources of in-situ electrical power: solar photovoltaics, wind, wave, and diesel generation. Our model utilizes time-domain simulation and optimization to identify cost-optimal system characteristics (e.g., generation and battery storage capacities). Using this model, I evaluate the cost of in-situ generation sources to power a 200 W ocean observation system deployed for five years at three unique geographic locations. I find that cost-optimal system characteristics to meet this load depend on resource and location, such that generation capacities are lower for the wave and wind resources (< 1 kW at locations with strong resources, up to a maximum of 3.3 kW) and larger for the solar and diesel resources (> 3 kW, in certain cases exceeding 7.5 kW). Cost-optimal battery storage requirements are generally < 55 kWh, with exception of the energy storage required for solar at the highest latitude location, which exceeds 175 kWh. I contextualize these results by performing a sensitivity analysis of key model parameters and identifying the potential economic impact of future technology advancements. Overall, our results indicate that the financial suitability of the resources evaluated in our study—solar, wind, wave and diesel—vary foremost by factors involving geographical location and resource availability, as well as factors that influence the cost of vessel intervention. This analysis establishes a foundation for future exploration of hybrid generation solutions, which may help to further optimize the generation and storage capacities required for persistent ocean observation. Another approach for reducing these capacities, involving resource forecasting, is explored in the subsequent chapter.

In Chapter 3, I consider an ocean observation system that also uses in-situ wave energy generation and battery storage, but meets *flexible* loads for oceanographic instrumentation and uses wave *forecasts* to manage this load in real time. By using wave forecasts to optimize power consumption, I hypothesize that it may be possible reduce the size of WEC and battery bank needed, thereby reducing the overall system's cost and complexity. I model an observation platform that can switch between four power states (full power: 600 W, medium power: 450 W, low power: 45 W, and survival mode: 1 W). To determine which power state to enter over time, I present a stochastic optimization method that interprets wave forecasts and system information to select a power state on an hourly basis, and simulate over two months of consecutive decisions. Using this simulation framework, I compare eight power management strategies across a range of WEC sizes (3 - 5 meter diameter) and battery capacities (2.5 - 35 kWh). I find that it is possible to maintain full (600 W) power consumption over the entire simulation window with a 5 meter diameter WEC and 25 kWh battery bank, which is on the upper end of the ranges evaluated. To employ a smaller WEC or battery, load flexibility is required. Forecast-based methods for this power management handle tradeoffs in performance (e.g., cumulative power consumption, reducing intermittencies and meeting scheduled load targets) more effectively than power management strategies that do not use forecasting. Overall, our results indicate that forecasting for wave-powered ocean observation is most impactful in handling these tradeoffs when some loads must be met on or within a defined schedule.

Although not described in the body of this dissertation, I adapted the analytical tools described in Chapters 2 and 3 to clarify how a tribal community may consider exercising its sovereign interests and authority over its marine space by using locally-available wave energy resources to address their priorities related to emergency preparedness, environmental change and freshwater shortages. In my concluding remarks, I discuss this project at a high level and recommend that, in addition to the characteristics and technology opportunities identified in Chapters 2 and 3, transdisciplinary and community-based approaches that empower denigrated populations and ecosystems are needed to truly “optimize” off-grid wave energy.

Acknowledgements

The work in this dissertation was funded by the National Science Foundation, the National Renewable Energy Laboratory (NREL), the U.S. Department of Energy's Water Power Technologies Office, and the U.S. Navy's Naval Facilities Engineering Systems Command (NAVFAC). My co-authors, Ben Maurer (NREL), Michael Lawson (NREL), Dale Scott Jenne (NREL), Dana Manalang (University of Washington Applied Physics Laboratory), Elena Baca (NREL), Sarah May Palmer (University of Washington), Marco Gunawan (University of Washington), and Brian Polagye (University of Washington) were instrumental in producing various aspects of the techno-economic model presented in Chapter 2. In particular, Sarah May Palmer helped by conducting a comprehensive literature review, drafting the introduction section (Section 2.1), and producing Figure 2.1. Marco Gunawan supported our analysis by designing and evaluating mooring systems in a MATLAB-based mooring dynamics software environment. Dana Manalang's expertise in ocean observation systems and cabled observatories helped to contextualize the use cases and applications used in and relevant to our models. While a visiting researcher at NREL, Dale Scott Jenne advised me on economic modeling, Elena Baca contributed through kilowatt-scale wave energy converter modeling, and Michael Lawson provided consistent advisory in using high performance computing resources to improve the speed and precision of our model outputs. Finally, Ben Maurer and Brian Polagye were supportive in every stage of these projects' developments, providing guidance and feedback as needed based on week-to-week challenges.

Beyond my co-authors, I gratefully acknowledge Bolun Xu (Columbia University) for providing insight on battery degradation under irregular cycling, as well as his source code for incorporation in our techno-economic model. I thank Elena Baca, Yi-Hsiang Yu (NREL) and David Ogden (NREL) for executing simulations that identify WEC hydrodynamics, used in our approach to kilowatt-scale WEC modeling

throughout this dissertation. Conversations regarding mooring design with Senu Sinirvas (NREL), Matt Hall (NREL), Richard Dewey (Ocean Networks Canada), Joe Talbert (University of Washington Applied Physics Laboratory) and Marco Gunawan were important to the completion of this analysis, as were conversations regarding optimization with Nathan Kutz (University of Washington). I thank Devin Mackenzie (University of Washington) and Fabien Koppes (Oceans of Energy) for guidance regarding solar energy modeling, and Robert Preus (NREL) for informing our wind energy models. In Chapter 3, I present an analysis of a forecast-based method for wave energy conversion that was influenced by Archis Ghate (University of Washington) and his course on Markov Decision Processes, which provided essential inspiration for our methodology and objective function design. I also thank Geoff Hollinger (Oregon State University) and Nathan Kutz (University of Washington) for recommendations on the design of our objective function. I thank Ning Li and Patrick Cross (University of Hawai'i) for providing the measured and forecasted datasets used in our study. Conversations regarding the design of the Wave-Powered Adaptable Monitoring Package (WAMP) with James Joslin (University of Washington) and Robert Cavagnaro (Pacific Northwest National Laboratory) were important for the development of forecast-based method, which used the WAMP as a case study.

I'd like to express my appreciation to the Makah Tribe for enabling and welcoming our collaboration, which I am hopeful will continue on beyond my doctorate. In particular, I would like to thank my project mentor and Makah staff Haley Kennard as well as Washington Sea Grant Marc Hershman Fellow Natalie Lowell for providing weekly feedback. My advisors at the University of Washington, Brian Polagye and Shana Hirsch, were also supportive in every stage of the project. I would also like the acknowledge the following 'key personnel' for providing important perspective and feedback throughout: Councilman Chad Bowechop, Chairman Timothy J. Greene Sr. and Councilman Glenn Ellis Jr. (Makah Tribal Council), David Lucas (Makah Public Works), Patty Manuel (Makah Operations, Office of the General Manager), Bud Denney and Ben Maxson (Makah Community Planning and Economic Development), Steve Joner, Stephanie Martin, Ryan Erhart, and Will Jasper (Makah Fisheries Management), Jasper Bruner (Neah Bay Public Safety), Rebekah Monette (Makah Cultural and Research Center) and Carol Reamer (Port of Neah Bay). Finally, I would like to thank Vince Cooke (Makah General Manager) who sadly passed away during the project, but was a kind and knowledgeable presence who included and welcomed me into the office building that we shared.

Within the Mechanical Engineering Department, I would like to thank Wanwisa Kisalang (University of Washington) for her exuberant administrative guidance, my advisor, Brian Polagye, for his unwavering support for me and my research, my committee member Michelle DiBenedetto (University of Washington) for taking curiosity in my research and career goals upon her arrival in the department, and Andy Stewart, who served as my co-advisor for the first three years of my PhD. Additionally, I appreciate the many students, staff and faculty who supported the events and conversations presented by a student group I co-organized, Mechanical Engineering Students Against Racism. Similarly, I appreciate the students involved with me in Global Renewables Infrastructure Development, a student group aiming to advance renewable energy toward equitable outcomes.

Throughout my doctoral studies, I was involved in a local ultimate frisbee team, Seattle Sockeye, that provided immense camaraderie, growth, accountability, and support, and I'd like to thank the dozens of teammates I have played with and coaches I have been coached by during this time. Finally, I'd like to thank the musical artists—including, but not limited to, Daniel Goldstein, Lupe Fiasco, Nas, and Carly Rae Jepsen—that powered me through late nights, early mornings, and everything in between to complete this dissertation.

DEDICATION

To my Grandmother, Frances Gibson

Contents

List of Figures

List of Tables

Chapter 1

Introduction

As human society develops, we continue to search for ways to exploit natural phenomena and resources for perceived humanitarian, national, and economic objectives. One example is the growing availability of electricity for humans and human-built systems, particularly in light of the climate crisis, which has motivated developments in renewable energy. Renewables can exploit natural processes to produce electricity at various scales. For example, wave energy conversion can provide megawatt-scale power for coastal areas, decarbonizing grid-connected regions, as well as kilowatt-scale power for oceanographic observation buoys that monitor underwater ecosystems, rural and coastal populations lacking electricity infrastructure, and other energy-consumptive applications in off-grid and ocean-adjacent settings.

As a relatively nascent renewable energy technology, less is known about the economics and optimal system design of wave energy. This is particularly true at the off-grid scale, as prior efforts to develop and understand wave energy have focused primarily on its potential contribution to the utility grid. Addressing this, the principal goal of this thesis is to improve our understanding of off-grid wave energy conversion from various perspectives, including its economic requirements, system features, and possible end uses. The thesis presents optimization software that simulates wave energy systems to identify cost-optimal system design and potential enhancements that may aid the impact and feasibility of off-grid wave energy. My analysis focuses primarily on the use of wave energy for ocean observation, which, through providing continuous and remote power at sea, may help to improve the flexibility, range, longevity and capabilities of instruments used for ocean science.

In Chapter 2, I present a comparative techno-economic analysis of resource options for powering in-situ ocean observations, including solar, wind, wave and diesel generation, therefore evaluating the "cost competitiveness" of these options. This is accomplished through a techno-economic model that uses time domain simulation and optimization to identify cost-optimal generation and storage capacities and total estimated costs across these resources at three geographic locations and for two ocean observation use cases. In this work, we find that it may be possible to further optimize system design by incorporating flexible instrument loads and resource forecasts for real-time decision making. In Chapter 3, I present a stochastic optimization method that accomplishes this, and demonstrate it in simulation for the power consumption of a wave-powered, battery-storage backed ocean observation system with flexible instrument loads. In both works, we present baseline results, as well as sensitivity analyses that help to describe the potential impact of technology advancements and evaluate assumptions made during model development.

Together, these two Chapters comprise three journal articles. *Cost-optimal wave-powered persistent oceanographic observation* [Dillon et al., 2022] was published in *Renewable Energy* in 2022 and describes our techno-economic model's application to wave-powered observation specifically (absent the other resources). We build on these findings in *Techno-economic comparison of resources for powering ocean observation* [Dillon et al., 2023b], which incorporates models for solar, wind and diesel. This article is currently under internal review and will be submitted to *Renewable Energy*. *Forecast-based stochastic optimization for wave energy conversion and storage* [Dillon et al., 2023a] is also under internal review and will be submitted to *Renewable Energy*. This work describes our analysis of the benefits using resource forecasts for real-time decision-making of flexible instrument loads for ocean observation. The two chapters in this dissertation have corresponding open-source codesets, intended to assist continued analysis and further clarify our methods: https://github.com/tmaxdillon/OO-TechEc (techno-economid analysis), and https://github.com/tmaxdillon/WAMP-MDP (forecast-based stochastic optimization).

Finally, this analysis was complemented and further advanced during a one-year fellowship at the end of my PhD, in which I adapted the described methodologies to clarify decision-making for a federally-recognized Washington State Tribal Community (the Makah Tribe) interested in understanding the possibility of harnessing their wave energy resources for community-based interests. This work is ongoing and the details of the project are not included in this dissertation. Nevertheless, this serves as a valuable example of how this analysis may help to orient off-grid wave energy technologies toward responsible and equitable end uses, and is therefore discussed at a high level in the concluding remarks of the dissertation.

Chapter 2

Techno-Economic Comparison of Resources for Powering Oceanographic Observation

2.1 Introduction

This chapter contains content from two journal articles that evaluate the economic suitability and cost-optimal characteristics of resources for powering ocean observations. Our first work, [Dillon et al., 2022], focuses on wave-powered ocean observation specifically. We built upon this by developing commensurate models for solar-, wind- and diesel-powered observation in [Dillon et al., 2023b], providing a comparative analysis of "in-situ" resources. This chapter therefore presents an integrated, comprehensive review of our techno-economic research.

Ocean sensing has a variety of end uses that are important to humans and the environment, including monitoring tsunamis [Kesavakumar et al., 2013] [Bernard and Meinig, 2011], weather and climate [Kohler et al., 2015], ocean acidification [Sastri et al., 2019], overfishing [Klemas, 2013], and biodiversity [Goodwin et al., 2019] [Sheehan et al., 2020] [Vonnahme et al., 2020] [Van Dover et al., 2017] [Van Dover, 2014]. The richest data streams originate from vessel-based field campaigns [Bottenheim et al., 2009] and cabled observatories [Kelley et al., 2016] [Smith et al., 2018] [Barnes and Tunnicliffe, 2008], where power is not a constraining factor, as well as globally-dispersed floats [Roemmich et al., 2009], gliders [Meinig et al., 2019] [Rynne and von Ellenrieder, 2008] [Daniel et al., 2011], and AUVs [Whitt et al., 2020]. However, each these methods has limitations that constrain the range, endurance, and/or scope of ocean observations. For example, sensors deployed on drifters, gliders, and AUVs must have relatively low power consumption, which restricts the breadth of sensors that can be deployed and/or measurement continuity and longevity [Copping et al., 2020]. Cabled observatories (e.g., Ocean Observatories Initiative Regional Cabled Array [Kelley et al., 2016] [Smith et al., 2018], Ocean Networks Canada [Barnes and Tunnicliffe, 2008]) offer kW-scale continuous power, but their high cost and inflexibility inherently restricts the number of locations where observations are possible. Field campaigns conducted from vessels are geographically flexible and avoid power or payload limitations, but are high cost, weather-dependent, pose risks to the crew, and are limited in duration.

A survey of ocean observation experts [Green et al., 2019] found that power availability is a consistent limitation for ocean sensing systems, and that if more power were available, systems could gather more data and/or increase deployment duration. This has driven decades of iteration to increase in-situ energy generation capacity for observing platforms, such as solar, wind, wave and diesel.

Several existing observation systems harvest solar energy [Kohler et al., 2015] [Kesavakumar et al., 2013] [Pettigrew et al., 2006], as solar photovoltaic panels are relatively low-cost [Ramasamy et al., 2022] and durable [Jordan et al., 2017]. However, when used in ocean applications, solar harvesting may suffer from seasonal asymmetry at relatively high latitudes [Chew et al., 2002], sea ice accumulation [Pettigrew et al., 2006], soiling (e.g., salt, bird droppings) [McLeod and Ringwood, 2022], and vandalism [Teng et al., 2010]. The resource also has relatively low power density (maximum of 1 kWm^{-2}), which increases the required platform space to achieve equivalent generation capacities relative to resources with higher power density.

In oceanographic applications, wind energy has been used primarily for propulsion (e.g., Saildrone [Meinig et al., 2019] [Gentemann et al., 2020], WASP [Rynne and von Ellenrieder, 2008]). Although wind turbines have been demonstrated in hybrid systems (e.g., FLiDAR Wind Sentinel, Arctic Research Centre – Mobile Observatory [Rysgaard et al., 2022]), and for redundant back-up power [Kesavakumar et al., 2013], at this time we are not aware of ocean observation buoys that use wind turbines for their primary power generation.

Wave energy may be an advantageous resource for powering ocean observations due to the resource's high power density and availability in high latitude locations [Gunn and Stock-Williams, 2012] [Copping et al., 2020] [Dillon et al., 2022] [McLeod and Ringwood, 2022]. Like wind, waves can be used for propulsion (e.g., Wave Glider [Daniel et al., 2011] [Manley and Willcox, 2010], PRAWLER [Osse et al., 2015], WireWalker [Pinkel et al., 2011]). Several wave energy converters (WECs) have been designed or tested as primary power sources for ocean observation buoys, including an oscillating water column [Pattanaik et al., 2021], a horizontal pendulum WEC [Dizon et al., 2021], and a rocking WEC [Wang et al., 2022]. Additionally, a WEC has been utilized to power a prototype observing system with a peak power consumption of 600 W [Joslin et al., 2019]. However, relative to other generation technologies, WECs are unproven and high-cost. To-date, most research and development of wave energy has centered on its potential contribution to terrestrial utility grids [Teillant et al., 2012] [Astariz and Iglesias, 2015] [Chang et al., 2018], which requires WECs with fundamentally different scales and operational characteristics than ocean observation.

Diesel generators were used to provide in-situ power for early ocean observation systems [Greer and Niederman, 1975]. Among modern systems, diesel generators have been useful for high power applications, such as collecting data from sea floor sensors [Clark and Sekino, 2001]. As an "on demand" resource, diesel generation has the benefit of not being constrained by daily or annual resource variations. However, although multiple generators can be utilized for redundancy [Clark and Sekino, 2001], autonomous diesel generation can be challenging in terms of maintenance, refueling and automated operation. Diesel generators also have a risk of chemical pollution if fuel storage tanks are ruptured.

These examples demonstrate the technical feasibility and challenges of using in-situ generation from solar, wind, wave or diesel to enable distributed, flexible ocean measurements with fewer power or payload constraints. However, there is a lack of understanding about the practical and economic considerations associated with each of these approaches. To date, most studies comparing the suitability and cost of various resources for off-grid power have centered on terrestrial applications [Baharudin et al., 2012] [Setiawan et al., 2009] [Thirunavukkarasu and Sawle, 2021] [Li et al., 2020] [Robertson et al., 2020] [Li et al., 2020], which fundamentally differ in scale and operational requirements from ocean observation. In our first work [Dillon et al., 2022], we quantified the cost-optimal characteristics of wave-powered ocean observation, but those conclusions would benefit from context through a direct comparison to the location-specific cost-optimal performance of other in-situ power options.

Building on the techno-economic model described in [Dillon et al., 2022], we incorporated economic and generation models for solar, wind, and diesel generation in [Dillon et al., 2023b]. The techno-economic model is driven by global resource data, economic benchmarks, kilowatt-scale in-situ generation modeling, and battery degradation estimation. Using time-domain simulation and optimization, our model identifies cost-optimal solar, wind, wave, or diesel generation and battery storage capacities for two categories of persistent ocean observation with differential service intervals. The model also estimates capital and operational expenditures required for each scenario, allowing us to identify and investigate the economic drivers and tradeoffs for powering persistent ocean observation with a range of resources.

The paper is organized as follows. Section 2.2 describes the locations and use cases included in our analysis. Section 2.3 lays out the details of the economic and power systems models, as well as the approach to cost optimization. Section 2.4 presents the model results, with an emphasis on sensitivity to baseline modeling assumptions. The implications of the results for ocean observing power systems are discussed in Section 2.5.

2.2 Locations and Use Cases

To capture cost variations driven by observation location and type, we assess three specific locations with different renewable resource characteristics and two observation use cases with different servicing intervals.

2.2.1 Geographic Scope and Site Properties

In setting geographic scope, our primary objective is to observe how geographically-varying aspects of system deployment influence cost. While a comprehensive, global analysis would be preferred, our simulation requires time-resolved, co-located and co-temporal information about solar irradiance, wind speed, and sea state. This significantly restricts the number of locations with available data. Consequently, we selected three specific locations from the National Science Foundation's Ocean Observatories Initiative (OOI) with similarly continuous, temporally-resolved resource data, but contrasting distance to coast, water depth, and resource power densities (Figure 2.1). We emphasize that our purpose in choosing these sites is not to evaluate the suitability of each generation type (solar, wind, wave and diesel) for these specific locations, but to conduct an evaluation across a set of representative, contrasting locations. Across the sites, distance to coast

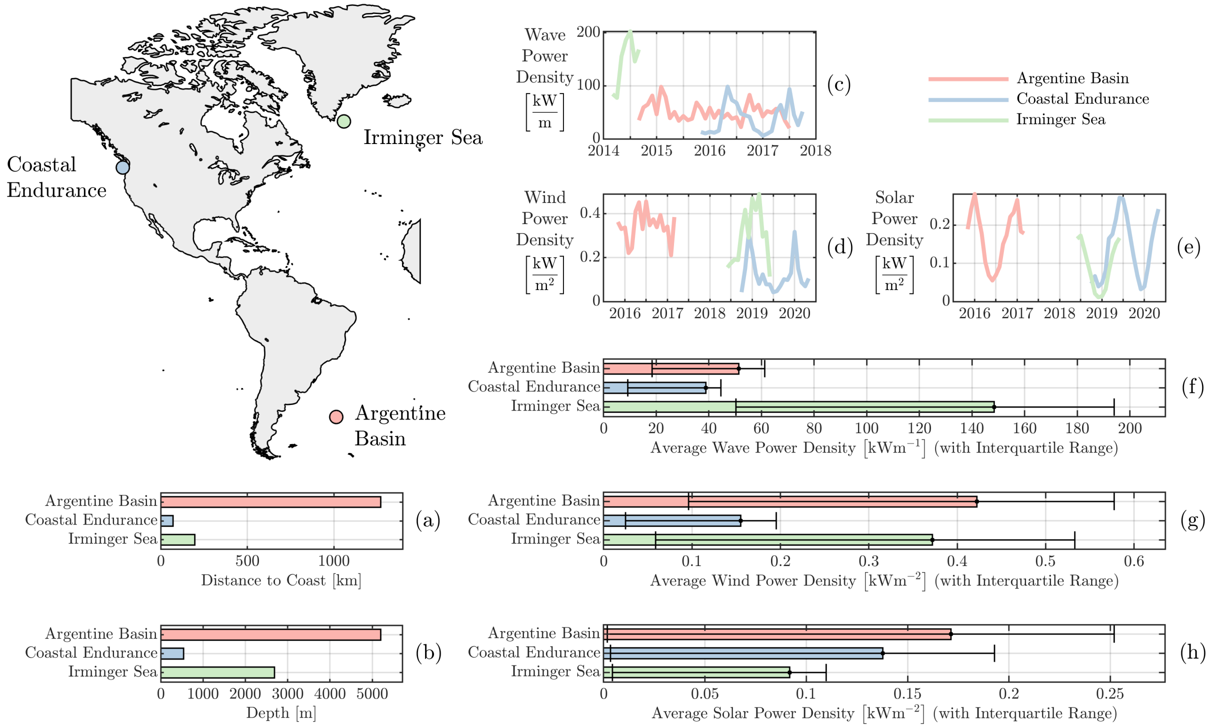

Figure 2.1: The three study locations have contrasting properties that influence system cost. Linear distance to coast (a), an approximation for distance from deployment location to port, influences the cost of vessel operations. Water depth (b) influences mooring cost. Resource power density, shown as monthly average power density over time (c-e) and average power density (f-h), influences power availability and, therefore, required storage and generation capacities. Note that the axes scale for (f-h) varies by resource and that, because of resource definition conversions, the wave resource is not directly comparable to solar and wind.

ranges from 70 to 1270 km, and depth from 540 to 5200 meters. The average solar power density ranges from 0.09 to 0.17 $\mathrm{kWm^{-2}}$, wind power density from 0.16 to 0.42 $\mathrm{kWm^{-2}}$ and wave power density from 39 to 150 $\mathrm{kWm^{-1}}$. Each of these properties have significant implications for overall system cost.

At each location, OOI measured shortwave irradiance using a pyranometer, wind speed using a sonic anemometer, and sea state using wave measurement buoys (TRIAXYS Next Wave buoy). Solar irradiance, wind speed, and statistical quantities describing the sea state (significant wave height, H_s, and peak period, T_p) were reported at one-hour intervals. In time domain simulations (Section 2.3.2), we assume that resources are constant between these discrete measurements. Time series were quality controlled by limiting start and end times to periods of continuous data availability and replacing short (e.g., 1-3 hour) measurement gaps and obvious outliers with interpolated values. Because solar, wind, and wave resources have significant intra-annual variability, we prioritized locations where time-series durations exceeded a year for all resources (Figure 2.1c). We made an exception for the sub-annual wave time-series available at Irminger Sea, due to this location's unique characteristics as a site with moderate depth and relatively short distance to shore. For this reason, this is also the only dataset in which the three resource measurements are not co-temporal. To evaluate the influence of long-term battery degradation on system economics, which is nonlinear (Section 2.3.2), we extend (i.e., concatenate) data from each location to produce a time series equal to the system lifetime, which has a baseline value of five years. In doing so, we assume that these measured durations are sufficiently representative of the resource over longer time frames. For the Irminger Sea location, we note that the dataset is primarily from the winter months and, consequently, overestimates the annual average wave and wind power density, while underestimating the annual average solar resource.

We note that [Dillon et al., 2022] contained two additional locations: Coastal Pioneer and Southern Ocean. These locations were removed from our comparative analysis [Dillon et al., 2023b] and this chapter to reduce the dimensionality of our results and improve interpretability. We selected these locations for removal because they contain imperfect wind and solar measurement time series data and have characteristics that are redundant in comparison to the other locations (e.g., Coastal Pioneer and Coastal Endurance have similar site proprieties).

2.2.2 Ocean Observation Use Cases

We explore the suitability of in-situ generation for ocean observation under two generalized use cases: short- and long-term instrumentation. Short-term instrumentation represents instrument platforms that must be serviced or replaced on a semi-annual basis, while long-term instrumentation represents platforms intended to operate without intervention over a multi-year lifetime and therefore have no planned service interval for instrumentation. This service interval dictates how frequently the site is accessed and, therefore, whether *additional* vessel mobilization is needed to maintain the power system. As discussed in Sections 2.3 and 2.4, our analysis identifies the cost of vessel operations as a significant cost driver, such that these use cases demonstrate distinct economic regimes.

Examples of short-term instrumentation platforms include coastal arrays and moored systems. Such arrays are likely to include physical, chemical, and biological sensors (e.g., CTD sensors, current meters, chlorophyll, CO_2, O_2), and are often positioned in coastal zones to monitor phenomena affecting and affected by coastal industries such as fisheries [Akhter et al., 2021], vessel traffic, and offshore energy installations [Griffin et al., 2016]. Instrumentation is often located higher in the water column, such that biofouling often necessitates service intervals between six and twelve months.

Examples of long-term instrumentation include biogeophysical sensors (e.g., ocean bottom seismometers, active sonars, hydrophones) and unique research instrumentation powered by cabled infrastructure. Many of these instruments can operate for years, until sensors require recalibration. The advent of cabled ocean observatories has enabled high-power and unique research instrumentation [Fischer et al., 2020], such as HD cameras, novel uses of multibeam sonars, instrumentation with onboard motors, actuators or lights [Marcon et al., 2019], and real-time processing of data streams [Whitt et al., 2020] [Polagye et al., 2020].

Specific use cases have varying sensing objectives, and a corresponding range of power requirements and service intervals. By generalizing use cases, rather specifying sensors and duty cycles, we generalize our results for a range of existing and future observing platforms. As our focus is evaluating the cost to power ocean sensing, we define four use case parameters (Table 2.1) that are dominant in influencing power system requirements and economics in our model.

Table 2.1: Generalized ocean observation use cases

Parameter	Short-Term Instrumentation	Long-Term Instrumentation
Service Interval	6 months	no service interval
Mean Power Requirement	200 W	200 W
Persistence Requirement	99%	99%
Lifetime	5 years	5 years

To differentiate the economic influence of service interval—6 months in short-term instrumentation and no service interval in long-term instrumentation—other parameters are held constant across use cases. The mean power requirement (200 W) is relatively large in comparison to routinely-deployed oceanographic instrumentation [Green et al., 2019], reflecting the potential for in-situ generation to deliver higher power levels than has been historically feasible in non-cabled settings—a requirement for the next generation of ocean sensing systems [Whitt et al., 2020]. The persistence requirement (99%) represents the percentage of time during which power is available to instruments, reflecting the priority for continuous time series measurements. We chose a five-year system lifetime to evaluate the extended operation enabled by in-situ generation, without making unrealistic assumptions about instrument durability. The sensitivities of model results to these use case parameters are presented in Section 2.4.1.

2.3 Methods

The techno-economic model was developed and implemented in MATLAB (Mathworks, 2020a). Here, we describe the model software at a high level. For greater detail and for re-use, our code is open source, available at https://github.com/tmaxdillon/OO-TechEc.

Through techno-economic modeling, we determine cost-optimal energy system capacities required to meet the defined persistence requirement at a specific location using four energy resources: solar, wind, wave, and diesel. In doing so, we also estimate costs to procure, deploy, and maintain the *power system* for each of these resources. We do not explicitly account for the cost to procure, deploy, and maintain *instrumentation* as we assume that this is independent of the power system used and, therefore, has no influence on the present analysis. Figure 2.2 shows this modeling procedure at a high level.

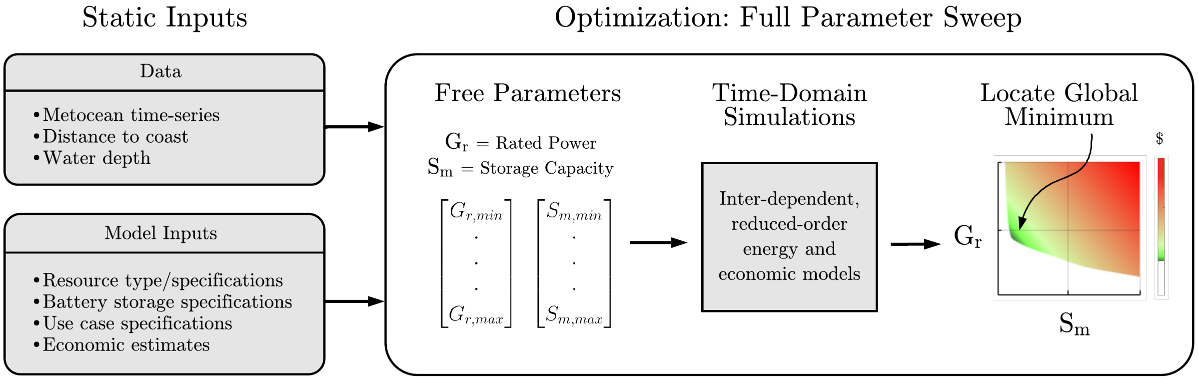

Figure 2.2: Optimization procedure for techno-economic model. The model uses a set of static inputs to drive the time-domain simulations that identify the generation and storage capacities (free parameters) that correspond to the minimum energy cost.

Each of the four energy resources in our study (solar, wind, wave, and diesel) undergo the same optimization procedure. Resource type, metocean resource data, power system, and load specifications, and economic parameters are static inputs. Rated generation capacity in kW (G_r) and storage capacity (i.e., maximum capacity) in kWh (S_m) are free parameters for optimization. These inputs drive interdependent reduced-order models, including energy models that simulate power conversion and storage in the time-domain, and economic models that estimate capital and operational costs. To find a global cost minimum for a given location and resource, we conduct a full parameter sweep of G_r and S_m, exclude combinations that do not meet the observation persistence (a_{sim}) requirement of 99%, and identify the lowest cost from the remaining options. Symbolically, this optimization is represented as

$$\min_{G_r,S_m} \Big[\mathrm{CapEx}(G_r, S_m) + \mathrm{OpEx}(G_r, S_m)\Big] \tag{2.1}$$

$$\text{s.t. } a_{\mathrm{sim}} \geq 0.99$$

where $\mathrm{CapEx}(G_r, S_m)$ and $\mathrm{OpEx}(G_r, S_m)$ are power system capital and operational expenditures. Capital expenditures are the sum of up-front costs for mooring ($\mathrm{CapEx_M}$), storage ($\mathrm{CapEx_S}$), and generation ($\mathrm{CapEx_G}$). Operational expenditures are the sum of storage ($\mathrm{OpEx_S}$), generation ($\mathrm{OpEx_G}$), and vessel ($\mathrm{OpEx_V}$) operating costs. How each of these cost categories are calculated depends on the type of energy resource being evaluated, as the resources have unique design requirements and cost relationships. Costs for each category are shown in Table 2.2 and resource-specific costs are provided in Table 2.3.

Table 2.2: Cost categories and sub-costs

Capital Costs	Mooring ($\mathrm{CapEx_M}$)	Acoustic release Anchor Chain, shackles, links & swivels Nylon line Subsurface buoyancy Installation Platform
	Storage ($\mathrm{CapEx_S}$)	Lithium iron phosphate (LFP) cells Housing & internal support
	Generation ($\mathrm{CapEx_G}$)	(see Table 2.3)
Operational Costs	Storage ($\mathrm{OpEx_S}$)	Battery replacement(s)
	Generation ($\mathrm{OpEx_G}$)	(see Table 2.3)
	Vessel ($\mathrm{OpEx_V}$)	Vessel charter Mobilization & demobilization Fuel

Table 2.3: Resource-specific costs

Resource	$\mathrm{CapEx_G}$	$\mathrm{OpEx_G}$
Solar	PV system Assembly	N/A
Wind	Turbine Assembly	Turbine refurbishments
Wave	WEC Assembly	WEC refurbishments
Diesel	Generator Enclosure & assembly	Generator repair Fuel

At a high level, we consider the following configurations for the generation resources:

- **Solar**: Solar photovoltaic panels with fixed orientation
- **Wind**: Stall-regulated wind turbine with passive yaw
- **Wave**: Point-absorber wave energy converter
- **Diesel**: Diesel generator operated intermittently at rated power, with periodic fuel replenishment

For all of these cases, mooring systems are required to hold the generation platforms in place (Appendix A.1) and battery storage is required to buffer intermittent power generation. Economic modeling requires information about rated generation capacities, mooring configurations (Appendix A.1), and vessel intervention for routine or unplanned maintenance of the power systems. We begin by presenting the economic models, followed by energy generation models. As these are interconnected concepts, some cross-referencing is unavoidable. We conclude by summarizing the cost optimization procedure.

2.3.1 Economic Modeling

Here we describe our models for capital and operational costs, which include mooring system ($\mathrm{CapEx_M}$), storage ($\mathrm{CapEx_S}$, $\mathrm{OpEx_S}$), generation ($\mathrm{CapEx_G}$, $\mathrm{OpEx_G}$ for solar, wind, wave, and diesel), and vessel operations ($\mathrm{OpEx_V}$).

All costs are given in 2023 U.S. dollars. Throughout the section, absolute costs are denoted by C, unit costs (e.g., cost per kW) by α, and failure rates by λ, with subscripts denoting specific categories and resources. Reflecting model uncertainties, input costs are rounded to the nearest ten dollars and output costs are rounded to the nearest hundred dollars. In each cost category, our goal is to estimate costs as a function of static inputs, G_r, S_m, and the output from the time-domain simulation. The costs described here are not comprehensive and neglect financing, environmental and regulatory compliance, and cost of non-recurring engineering for design and labor for assembly. To reduce model complexity, certain cost drivers, such as vessel availability, geographical cost variations, and weather windows or seasonal delays are similarly neglected. For simplicity and because system components have varying and generally short ($\leq$ 5 year) lifetimes, we assume a simple payback model with no discount rate. In Section 2.4.1, we present a sensitivity to input parameter analysis that explores how our assumptions impact cost projections.

Mooring

The mooring system maintains the energy generation platform's position against metocean forcing. Depending on the types of instrumentation being powered, the energy system might require a separate mooring and, therefore, we conservatively assume a stand-alone mooring system is required for all resource types. Because the system lifetime is short ($\leq$ 5 years), we assume there is no cost to maintain the mooring system. Therefore, mooring costs are only capital ($\mathrm{CapEx_M}$), and include the cost of in-line elements (C_{lineel}), the cost to install the mooring system ($C_{\mathrm{inst,moor}}$), and the material cost of the platform for the generator (C_{plat}).

C_{lineel} includes the cost of an acoustic release, anchor, chain, shackles, links, swivels, polyethylene fiber line, and subsurface flotation (e.g., "false bottom" configuration for the surface expression). We parameterize this cost as a function of surface float diameter and water depth, which influence both the length and minimum breaking strength of the line, as well as the forcing on the entire mooring system. Using Mooring Design and Dynamics (MDD [Dewey, 1999]), for each resource we designed a matrix of surface float diameters and water depths with the objective of minimizing mooring cost while maintaining sufficient element strength. We modeled WECs as cylindrical elements that can submerge or "blow down" in extreme conditions. Due to a lack of published information on solar, wind and diesel mooring systems at this scale, we made several assumptions to estimate C_{lineel} for these resources, which are described at a high level here and more comprehensively in Appendix A.1.

Surface floats for solar and diesel generation share functional and geometric similarities (e.g., we assume that these generation options cannot blow down to protect equipment, and, unlike wind turbines, do not need to resist significant thrust loads to remain upright). Consequently, solar and diesel generation share the same model for C_{lineel}. In the case of wind generation, we similarly assume that the turbine cannot blow down, but assume that a counter-balancing spar is required to keep the turbine upright due to the thrust loading on the rotor. However, as discussed in Appendix A.1, we found that for expected spar form factors (height-to-diameter ratio of five), the forces imposed by currents or waves on the mooring drives the diameter required to prevent blow down. Consequently, a spar diameter of 0.8 meters is sufficient for all turbine sizes evaluated in this study and, for wind, C_{lineel} can be modeled solely a function of water depth. The parametric cost matrices used to calculate C_{lineel} for each resource are provided in Tables 2.4 to 2.6. Because MDD requires an iterative, human-in-the-loop, approach to mooring design, during cost optimization, the values in each matrix are linearly interpolated to approximate C_{lineel} for combination of float diameter and water depth. Water depth is determined by the deployment location. WEC and solar platform diameters are a function of G_r (Section 2.3.2 and Section 2.3.2, respectively).

Table 2.4: Cost matrix of in-line mooring elements (C_{lineel}) for wave resource

		WEC Diameter [m]		
		1	**3**	**6**
Water Depth [m]	**5500**	\$129,310	\$130,220	\$136,200
	3000	\$68,170	\$85,720	\$91,700
	1000	\$47,830	\$54,880	\$59,840
	500	\$38,510	\$43,990	\$49,660
	120	\$10,650	\$11,560	\$20,130

Table 2.5: Cost matrix of in-line mooring elements (C_{lineel}) for solar and diesel resources

		Platform Diameter [m]			
		2	**4**	**8**	**12**
Water Depth [m]	**5500**	\$128,520	\$130,840	\$243,200	\$729,590
	3000	\$87,520	\$90,330	\$155,900	\$467,710
	1000	\$53,940	\$62,130	\$83,090	\$249,270
	500	\$38,960	\$46,480	\$71,580	\$214,740
	120	\$11,530	\$16,220	\$26,670	\$80,020

We assume the primary driver of $C_{\text{inst,moor}}$ is the cost of the installation vessel. Because mobilizing two deployment vessels is not cost-effective, we assume instrumentation platform and power system mooring installation occur simultaneously, executed by a specialized global-class vessel. Based on UNOLS global-class vessels (e.g., R/V Atlantis, R/V Thomas G Thompson), we assume a day rate of $\$57,500/\text{day}$. We

Table 2.6: Cost matrix of in-line mooring elements (C_{lineel}) for wind resource

		Spar Diameter [m]
		0.8
Water Depth [m]	**5500**	\$128,520
	3000	\$87,750
	1000	\$54,690
	500	\$38,960
	120	\$11,530

expect the power system mooring installation to vary with water depth, requiring an additional 12 hours on site in deep (5000 m) water (i.e., $C_{\text{inst,moor}} = \$28,750$) and 6 hours on site in shallow (500 m) water (i.e., $C_{\text{inst,moor}} = \$14,380$) [Talbert, 2021]. We linearly interpolate or extrapolate between these two values to find installation time and cost as a function of water depth.

We find C_{plat} by assuming that the platform's material is fabricated steel priced at \$2000 per metric ton (source: CostOwl). We assume platform mass is five times the generation system mass, which is an assumption that has high uncertainty that we, therefore, evaluate as a sensitivity parameter (Appendix A.7). Generation system mass is calculated from G_r assuming that solar panels are 30 kgm^{-2} [Lisell et al., 2009] and wind turbines are 15 kgkW^{-1} [Corbus et al., 1999]. Diesel generator mass is found through a non-negative linear regression of mass versus rated power for nine sub-20 kW diesel generators used as inputs (Appendix A.2). For the wave resource, we assume that the mooring system is coupled directly to the WEC and that a separate platform is not required (i.e., C_{plat} = 0 for the wave resource).

Storage

Because solar, wind, wave and diesel resources are intermittent, energy storage is necessary to achieve the required power availability. We assume this cost has capital (CapEx_S) and operational (OpEx_S) components, and base estimates on the cost of lithium iron phosphate (LFP) batteries. In determining battery chemistry, we compared LFP cells with lead-acid absorbed glass mat (AGM) cells. AGM batteries are roughly half cost (per unit energy storage) of LFP batteries, are durable, exhibit low self-discharge, and have long service life even when deep-cycled. However, LFP batteries have similar performance properties and are smaller and lighter per unit energy storage. Commercially available LFP battery banks report energy densities ($\mathrm{Ahm^{-3}}$) 360-400$\%$ and specific energies ($\mathrm{Ahkg^{-1}}$) 250-400$\%$ that of AGM counterparts. This selection is partially driven by necessity, as preliminary simulations with AGM batteries resulted in battery bank weights that could be difficult to handle at sea. The selection of LFP over AGM chemistry should improve handling and reduce costs during deployment and battery replacement, as well as improve ability to fit cells entirely within the surface platform hull or, in the case of the wave resource, WEC. In comparison to other lithium-ion chemistries, LFP batteries have slightly lower energy density and specific energy, but are much safer in thermal runaway [Feng et al., 2018], providing benefits in regulatory and environmental compliance. LFP cells have also demonstrated improved lifetimes relative to lithium-ion counterparts [Xu et al., 2016]. We recognize that—in contrast to AGM—LFP is currently an uncommon choice in ocean applications. However, given the chemistry's positive attributes, we anticipate that LFP use will increase over the next decade.

We assume capital expenditures for energy storage ($\mathrm{CapEx_S}$) includes the cost of battery cells (C_{batt}), and housing (C_{hous}). C_{batt} is computed by multiplying S_m by \$470$\mathrm{kWh^{-1}}$, the unit cost of LFP batteries [IRENA, 2020]. For simplicity, we estimate the cost of a waterproof pressure housing and internal supports (C_{hous}) as linearly dependent on cell cost (i.e., $C_{\mathrm{hous}} = m_{\mathrm{hous}} C_{\mathrm{batt}}$). As a baseline assumption, we assume housing cost is equal to cell cost (i.e., m_{hous} = 1), which is likely inflated, given the manufacturing cost differential between batteries and mechanical structure. We note, however, that battery capital cost is a relatively small component of total cost, such that results are not sensitive to this simplification.

Operational expenditures for storage ($\mathrm{OpEx_S}$) are dependent on C_{batt} and battery lifetime. Due to the maintenance-free characteristic of LFP batteries, we assume the battery system will not fail unexpectedly, and will be replaced on a schedule in response to long-term degradation. Therefore, $\mathrm{OpEx_S}$ is the product of C_{batt} and the estimated number of battery replacements required throughout system operation (n_{br}). The latter term is found as

$$n_{br} = \left\lceil \frac{L_{\mathrm{dep}}}{L_{\mathrm{batt}}} - 1 \right\rceil \tag{2.2}$$

where L_{dep} is the length of the deployment (i.e., 60 months for the baseline assumptions) and L_{batt} is the lifetime of the battery bank in months, which is determined directly from the output of the time-domain simulation and is described in Section 2.3.2. We note that n_{br} is rounded up to the nearest whole number to account for the full cost of the partial usage of the last battery.

Solar Cost Model

We base solar equipment costs on residential, rooftop units [Ramasamy et al., 2022], which are of similar generation capacity to those evaluated here. $\mathrm{CapEx_G}$ for solar generation, therefore, includes photovoltaic modules (α_{mod}, \$480/kW), electrical infrastructure (α_{elec}, \$310/kW), structural infrastructure (α_{struct}, \$90/kW), and assembly ($\alpha_{\mathrm{assem,solar}}$, \$160/kW) [Ramasamy et al., 2022]. We apply a "marinization factor" of 1.2 (i.e., an increase to account for the added cost of water-sealed, corrosion- and fouling-resistant components) to α_{mod}, α_{elec} and α_{struct} and, therefore compute $\mathrm{CapEx_G}$ for the solar resource as

$$\mathrm{CapEx_G} = (1.2(\alpha_{\mathrm{mod}} + \alpha_{\mathrm{elec}} + \alpha_{\mathrm{struct}}) + \alpha_{\mathrm{assem,solar}})G_r. \tag{2.3}$$

We note that α_{elec} does not include the cost of an inverter, as unlike grid-connected systems, there is not a need to convert from direct to alternating current in our application. The lack of an inverter not only reduces cost, but also reduces maintenance requirements and increases durability [Walker, 2018]. Photovoltaic module failures are extremely rare, typically occurring for $<0.1\%$ of modules per year [Jordan et al., 2017]. In terrestrial settings, photovoltaic systems have operational lifetimes of 25 to 40 years [Jordan and Kurtz, 2013] and we, therefore, assume that there are no costs associated with the maintenance, replacement and/or refurbishment of the solar systems (i.e., $\mathrm{OpEx_G}$ = 0 for the solar resource). The number of vessel interventions (n_{vi}) for the solar resource depends on panel soiling and cleaning assumptions (Section 2.3.2).

Wind Cost Model

We base wind costs on distributed and "small" (<100 kW) wind projects [Orrell et al., 2022], and available cost information for commercially-available turbines. We, therefore, define $\mathrm{CapEx_G}$ for the wind resource as the sum of turbine (C_{turb}) and assembly ($C_{\mathrm{assem,wind}}$) (i.e., cost of installation prior to loading the deployment vessel) costs. We compute C_{turb} by estimating the unit cost of small-scale distributed wind turbines (α_{turb}), found through a non-negative linear regression of market cost versus rated power for 18 sub-10 kW wind turbines (Appendix A.3), resulting in α_{turb} = \$2,850/kW. As for solar, we apply a marinization factor of 1.8 to turbine cost, with the larger value reflecting the need to marinize the rotary seal between the rotor and nacelle containing the gearbox and generator.

We compute $C_{\text{assem,wind}}$ using the average “installed” cost from small-scale distributed wind projects, defined as \$5120/kW in [Orrell et al., 2022], less turbine unit cost, resulting in an assembly unit cost ($\alpha_{\text{assem,wind}}$) of \$2,270/kW. This assumes that a small-scale wind installation for oceanographic sensing will incur all of the costs associated with a terrestrial installation. We further assume CapEx_{G} for the wind resource should include the cost of two wind turbines (spares provisioning) such that

$$\text{CapEx}_{\text{G}} = 2(1.8\alpha_{\text{turb}} + \alpha_{\text{assem,wind}})G_r. \tag{2.4}$$

We define OpEx_{G} for the wind resource as the cost of turbine refurbishment following recovery. To reduce the risk of unexpected failure, we assume the turbine is replaced if battery storage replacement is required (regardless of turbine condition) and further assume replacements due to wind turbine equipment failures at a rate of λ_{wind} per year. Because turbine failure rates in this application are unknown, we consider two durability scenarios, optimistic (λ_{wind} = 0) and conservative (λ_{wind} = 1) durability. We assume refurbishment is half the cost of an individual turbine. Therefore, we compute OpEx_{G} as

$$\text{OpEx}_{\text{G}} = \frac{1}{2}\frac{\text{CapEx}_{\text{G}}}{2}[\lambda_{\text{wind}}L_{\text{dep}} + n_{br}] \tag{2.5}$$

where L_{dep} is the length of the deployment (i.e., 5 years for the baseline assumptions) and n_{br} is the number of battery replacements. Total number of vessel interventions (n_{vi}) for the wind resource is defined as $\lambda_{\text{wind}}L_{\text{dep}}$ + n_{br}. We note that, as discussed in Section 2.5.4, battery replacements are not anticipated. Therefore, n_{vi} is typically set by the number of generation device failures.

Wave Cost Model

Because wave energy conversion is a relatively unproven technology, cost estimates have significant implicit uncertainty, particularly for kW-scale WECs. This is because, to date, most economic evaluation of wave energy conversion has centered on systems designed for utility scale applications [Astariz and Iglesias, 2015]. Due to lack of reliable cost estimates for wave energy at smaller scales, we base economic estimates on multiplies applied to the wind cost model. While wind generators have different hardware requirements, they are, at this time, the closest mature energy generation comparable to wave energy conversion. We, therefore, base our comparison on three hypothetical scenarios where WEC economics exhibit contrasting cost and durability benchmarks. These scenarios, which define WEC unit cost (α_{wec}), unit cost of assembly ($\alpha_{\text{assem,wec}}$) (i.e., installation prior to loading the deployment vessel), and unexpected WEC failures per year (λ_{wec}), are shown in Table 2.7.

Table 2.7: WEC scenario costs and durability

Scenario	α_{wec}	$\alpha_{\text{assem,wec}}$	λ_{wec}
Optimistic Cost	$\frac{\$11{,}390}{\text{kW}}$	$\frac{\$2{,}270}{\text{kW}}$	$\frac{\text{1 failure}}{\text{year}}$
Optimistic Durability	$\frac{\$28{,}480}{\text{kW}}$	$\frac{\$2{,}270}{\text{kW}}$	$\frac{\text{0 failures}}{\text{year}}$
Conservative	$\frac{\$28{,}480}{\text{kW}}$	$\frac{\$2{,}270}{\text{kW}}$	$\frac{\text{1 failure}}{\text{year}}$

WEC unit cost (α_{wec}) is defined as a multiple of α_{turb}, 4x for the optimistic cost scenario and 10x for the optimistic durability and conservative scenarios. We believe that these multipliers are conservative given the higher energy density of waves relative to wind. Assembly cost ($\alpha_{\text{assem,wec}}$) is estimated to be the same as for wind. As WEC failure rates are unknown, λ_{wec} is provisional, reflecting possible upper and lower bounds of WEC durability. As with instrumentation (Section 2.2.2), we note that biofouling may be a driver of WEC service intervals. This uncertainty is also evaluated as part of the sensitivity analysis, which includes the effect of a higher failure rate.

Like the wind cost model, we assume CapEx_{G} for the wave resource includes the cost of two WECs for spares provisioning such that

$$\text{CapEx}_{\text{G}} = 2(\alpha_{\text{wec}} + \alpha_{\text{assem,wec}})G_r \tag{2.6}$$

and compute OpEx_{G} for the wave resource as

$$\text{OpEx}_{\text{G}} = \frac{1}{2}\frac{\text{CapEx}_{\text{G}}}{2}[\lambda_{\text{wave}}L_{\text{dep}} + n_{br}] \tag{2.7}$$

assuming that the cost of refurbishment is half the cost of an individual WEC. Total number of vessel interventions (n_{vi}) for the wave resource, like wind, is defined as $\lambda_{\text{wave}}L_{\text{dep}}$ + n_{br}.

Diesel Cost Model

We base diesel cost estimates on commercially available marinized diesel generators. We assume $\mathrm{CapEx_G}$ for the diesel resource includes the cost of the generator, as well as the generator's enclosure and assembly. We compute kW-scale generator cost ($C_{\mathrm{dgen}}(G_r)$) through a non-negative linear regression of market cost versus rated power for nine sub-20 kW diesel generators used as inputs (Appendix A.2). We include the cost of an auto-start feature, as the generator would need to be switched on and off remotely, and price this at \$3,450 based on a vendor quote. We base the cost of an enclosure to protect generator from the marine environment and assembly cost on the cost of a similar enclosure and assembly for the Wave-Powered Adaptable Monitoring Package [Joslin et al., 2019], which was designed to protect batteries and a computer and required \$5,950 for a volume of 1.5 m^3 (\$3,970/m^3). For the nine sub-20 kW diesel generators, generator volume (0.22 m^3) is independent of power rating (Appendix A.2), such that the estimated and enclosure and assembly cost is \$890 and independent of G_r.

Like the wind and wave resources, we assume two generators are purchased for spares provisioning during required replacement. $\mathrm{CapEx_G}$ for the diesel resource is, therefore,

$$\mathrm{CapEx_G} = 2(C_{\mathrm{dgen}}(G_r) + \$3450 + \$890). \tag{2.8}$$

$\mathrm{OpEx_G}$ for the diesel resource includes the cost of fuel (assumed to be $\$1.4\mathrm{L}^{-1}$) and generator repair. As failure rates for autonomous diesel generators in marine applications are uncertain [Marqusee and Don II, 2020], we assume a generator failure rate per year (λ_{dgen}) of 0.2. Like the wind and wave resources, we assume the cost of generator repair is half the cost of the initial investment, such that, for the diesel resource

$$\mathrm{OpEx_G} = \frac{1}{2}\frac{\mathrm{CapEx_G}}{2}[\lambda_{\mathrm{dgen}} L_{\mathrm{dep}} + n_{br}]. \tag{2.9}$$

We assume diesel generators, in addition to intervention following unexpected failures, would require scheduled interventions to change oil and replace fuel. Therefore, number of vessel interventions (n_{vi}) for the diesel resource depends on our approach to diesel generation energy modeling (Section 2.3.2).

Vessel Operations

Vessel operations are necessary for power system maintenance (e.g., generator repair, battery replacement), as well as sensor maintenance (e.g., calibration). Here, we include only *additional* vessel costs required for the power system ($\mathrm{OpEx_V}$). Because site access and service interval vary by use case, estimation of $\mathrm{OpEx_V}$ varies similarly. Both formulations depend on the number of vessel interventions required throughout system operation (n_{vi}), which is defined for each resource in Sections 2.3.1 to 2.3.1.

For the long-term instrumentation use case, we assume the instrumentation has no planned service interval. Therefore, dedicated vessel mobilization is required for power system maintenance or replacement. We assume an Offshore Supply Vessel (OSV) is sufficient for transporting components (e.g., battery bank, replacement generator) to and from remote locations, and estimate cost from OSV operating rates and transit specifications. The cost of vessel operations for long-term instrumentation ($\mathrm{OpEx_V}$) is

$$\mathrm{OpEx_V} = n_{vi}\alpha_{\mathrm{v,osv}}\left[t_{\mathrm{m,osv}} + \frac{2d_{\mathrm{s}}}{v_{\mathrm{osv}}}\right] \tag{2.10}$$

where the first term is number of vessel interventions required for power system components, $\alpha_{\mathrm{v,osv}}$ is the day rate for OSV charter ($\$17,250/\mathrm{day}$, estimated conservatively to account for fuel, mobilization and demobilization [Boget, 2020]), d_{s} is distance from shore to deployment location in km (Figure 2.1), v_{osv} is OSV transit speed (10 knots, or 444 km/day) and $t_{\mathrm{m,osv}}$ is amount of time spent on site for maintenance (0.25 days).

In the short-term instrumentation use case, we assume there is a 6-month service interval for sensor maintenance. Further we assume that unexpected power system maintenance would not trigger mobilizing a dedicated vessel, such that power system maintenance would occur during the next regularly-scheduled instrumentation cruise. Therefore vessel operations for short-term instrumentation does not include transit and Eq. 2.10 reduces to

$$\mathrm{OpEx_V} = n_{vi}\alpha_{\mathrm{v,spec}}[t_{\mathrm{m,spec}}] \tag{2.11}$$

where $\alpha_{\mathrm{v,spec}}$ is the estimated cost of a specialized, global-class vessel used for instrumentation maintenance ($\$57,500/\mathrm{day}$), and $t_{\mathrm{m,spec}}$ is the additional amount of time spent on site to execute power system maintenance (2 hours or 0.084 days). Note that we assume $t_{\mathrm{m,spec}} < t_{\mathrm{m,osv}}$, based on the expectation that planned intervention is more time-efficient and that power system maintenance can be executed alongside instrumentation maintenance to save time.

2.3.2 Energy Modeling

To identify combinations of G_r and S_m that can provide *persistent* power for oceanographic instrumentation, we model the temporal variability in generated and stored power across resources. Energy transfer between the generator (solar, wind, wave, or diesel), battery bank, and instrumentation platform are simulated in the time domain as

$$S_{t+1} = S_t + (P_t - L_t)\Delta t - D_t - \Gamma(S_t) \tag{2.12}$$

where the t and $t+1$ subscripts denote the current and next time step, Δt is time step interval (1 hour), S is battery storage, P is generator power output, L is power consumed by the instrumentation platform (assumed to be constant in time), D is energy discarded, and $\Gamma(S)$ is self-discharge of the battery as a function of battery storage (3% loss per month). We constrain S_{t+1} to a maximum of $(S_m - S_m\sigma(S_{1:t}))$, where $S_m\sigma(S_{1:t})$ is battery capacity lost over time due to degradation, and discard any excess generation through a resistive load (represented by D). We allow S_{t+1} to drop to 0 kWh, as LFP batteries can be fully discharged. If there is insufficient power available (P or S) at a given time step to meet the load, L is reduced to zero.

The time series of power consumed ($L(t)$) is used to determine whether the 99% persistence requirement is met. We compute the persistence achieved in simulation (a_{sim}) as

$$a_{\mathrm{sim}} = \frac{\sum_{t=1}^{N} L(t) = L_{fp}}{N} \tag{2.13}$$

where N is the number of simulation time steps and L_{fp} is the full power consumption of 200 W. If $a_{\mathrm{sim}} \geq$ 0.99, this combination of G_r and S_m meets the persistence requirement.

Battery Degradation

Battery degradation (i.e., the loss of storage capacity over time or "capacity fading") determines whether battery replacements are required throughout the system's lifetime. In addition to the cost of new battery cells, replacement also incurs costs for vessel operations (Sections 2.3.1 and 2.3.1). Battery degradation is, therefore, an important consideration for overall system economics.

Battery degradation is a nonlinear process dependent on battery age, depth and frequency of discharge/recharge (or "cycling"), discharge rate, average state of charge, temperature, and maintenance [Birkl et al., 2017]. To date, most studies quantifying the degradation of LFP batteries focus principally on capacity losses due to routine cycling (i.e., the number of cycles the battery is subjected to) [Omar et al., 2014] [Ye et al., 2012]. However, the cycling in our application is irregular due to the intermittent nature of the energy resources compared to the constant power draw by the instrumentation platform. We therefore use a model specifically designed to estimate degradation of lithium-ion batteries under irregular cycling. Xu et al. [Xu et al., 2016] use empirically-derived stress models to estimate capacity fading due to battery temperature, average state of charge, depth and number of discharge cycles, and calendar aging (i.e., time). To count irregular cycles, the authors utilize the rainflow counting algorithm [Downing and Socie, 1982], which is widely used in structural fatigue analysis. Xu et al.'s model also captures two nonlinear effects: (1) solid electrolyte interphase (SEI) film formation, which causes fast initial degradation at early cycles [Laresgoiti et al., 2015] and (2) the dependence of degradation rate on the number of active lithium ions remaining in the battery [Millner, 2010], which causes the degradation rate to slow until the battery approaches its end of life (EoL).

We adapted Xu et al.'s code for use in our model by incorporating LFP-specific empirical coefficients from [Millner, 2010] and making minor updates for compatibility. The battery degradation model inputs are the battery's state of charge profile ($S_{1:t}$) and temperature (T_{batt}). Previous assessments have identified 15-20 °C as an optimal operating temperature, while warmer and colder temperatures exhibit different, yet similarly accelerating degradation effects [Xu et al., 2016] [Lam et al., 2011]. As our study locations (Figure 2.1) are at high latitudes (> 40 °), we expect that battery temperatures between 2 and 10 °C are possible. However, because Xu et al. caution against extrapolating their model to temperatures below 15 °C due to limited experimental data, we assume T_{batt} = 15 °C across all scenarios. We assess the influence of warmer battery temperatures as an approximation for the potential impact of accelerated degradation due to *colder* battery temperature and discuss the implications of this in Section 2.5.4.

The battery degradation model output, σ, represents capacity fading normalized between 0 and 1 (with 0 corresponding to a new battery and 1 corresponding to a battery with no capacity remaining). Consistent with Xu et al.'s formulation, as a baseline, we assume that battery EoL occurs when 80% of the battery's capacity remains ($\sigma_{\mathrm{EoL}} = 0.2$). In time domain simulation, we explicitly account for slow changes in capacity by updating the battery capacity every month (730 hours). This reduces computational expense relative to updating every time step. If the battery reaches its end of life ($\sigma(S_{1:t}) \geq \sigma_{\mathrm{EoL}}$), we assume it is replaced with a new battery and set battery lifetime (L_{batt}, Eq. 2.2) to t.

Solar Generation Model

To estimate solar power output, we must consider instantaneous conversion efficiency as well as long-term efficiency losses. We assume that solar panels deployed in this application would be fixed (i.e., not use a solar tracking system to orient panels toward the sun) to reduce cost, complexity and risk of failure. We, therefore assume a conservative static panel efficiency of 18%, and a degradation rate of 0.5% per year [Jordan and Kurtz, 2013] [Whaley, 2016].

While operating remotely at sea, panels may be exposed to various soiling mechanisms (e.g., bird droppings, salt encrustation) without cleaning. Soiling is exacerbated by humidity, hot climates, high winds, hail, salty air and high insolation, [Whaley, 2016] all of which could be expected in this application. At this time, marine soiling rates are not available and we base our soiling calculation on terrestrial reports. Terrestrial soiling rates are typically between 0.04% and 0.08% loss per day and can be 4-8 times this, reporting at 0.36% loss per day in agricultural settings [Whaley, 2016]. To find an *annual* soiling rate, we assume a similar increase upon common annual soiling rates, which are between 4.3% and 7.5% loss per year [Whaley, 2016]. We therefore assume an annual soiling rate of 35% loss per year. Cleaning effects due to rainfall are ignored.

A 35% loss per year soiling rate causes efficiency to decline critically within the deployment lifetime, such that, if no intervention is taken, required platform sizes regularly exceed the scope and scale of our mooring cost analysis (> 12 meters). We, therefore, consider and compare two panel cleaning strategies: automated and human. In automated cleaning, we assume that, with a 2x increase in module unit cost

(α_{mod}, Section 2.3.1) it is possible to keep panels clean without human intervention (e.g., robotic wipers, soiling-resistant coatings), such that soiling rate is negligible (i.e., 0% loss per year). For human cleaning, we assume that a vessel would be mobilized every other fall to clean panels manually, thereby resetting efficiency losses due to soiling to 0% prior to the months of least sunlight. In the case of short-term instrumentation (Section 2.2.2), where site access occurs every six months, under the human cleaning scenario we assume instead that panels would be cleaned during each of these visits and that cleaning would not add time to vessel charter (i.e., $t_{\mathrm{m,spec}}$ = 0).

To find solar generation over time, we assume a rated (i.e., maximum) panel irradiance of $1\ \mathrm{kWm}^{-2}$ and compute power output as follows

$$P_t = \begin{cases} \eta_{\mathrm{soil,t}} \eta_{\mathrm{deg,t}} G_r \frac{i_t}{i_r} & i_t \leq i_r \\ \eta_{\mathrm{soil,t}} \eta_{\mathrm{deg,t}} G_r & i_t > i_r \end{cases} \tag{2.14}$$

where subscript t denotes time step, $\eta_{\mathrm{soil,t}}$ is efficiency loss due to soiling over time, $\eta_{\mathrm{deg,t}}$ is efficiency loss due to module degradation over time, i_t is shortwave irradiance in Wm^{-2}, and i_r is rated irradiance in Wm^{-2}. The available i_t at each location was measured using a pyranometer, which captures direct and diffuse components of irradiance incident on a planar surface. We assume this measurement is equivalent to the irradiance that would be incident on a photovoltaic panel or array.

To find platform diameter for the solar resource, which is necessary to calculate C_{linel} (Section 2.3.1), we find panel area (A) as

$$A = \frac{G_r}{i_r \eta_{PV}} \tag{2.15}$$

where η_{PV} is unsoiled panel conversion efficiency. Platform diameter (d_{solar}) is then found through the circular area afforded by panel area as

$$d_{\mathrm{solar}} = 2\sqrt{\frac{A}{\pi}}. \tag{2.16}$$

Wind Generation Model

Wind turbines operate in four regions, dictated by the cut-in speed (u_{ci} = 3 m/s) (i.e., wind speed at which power generation begins), the rated speed (u_r = 11 m/s) (i.e., the speed at which the turbine reaches its rated power) and the cut-out speed (u_{co} = 30 m/s) (i.e., the speed at which power generation ceases for survival reasons). These parameters are selected in accordance with American Wind Energy Association (AWEA) standards [Standard, 2009] and values commonly seen in practice at this scale, and are held constant across all locations, turbine sizes and use cases. Wind generation over time is, therefore, found by

$$P_t = \begin{cases} 0 & u_t \leq u_{ci} \\ G_r \left(\frac{u_t}{u_r}\right)^3 & u_{ci} < u_t \leq u_r \\ G_r & u_r < u_t \leq u_{co} \\ 0 & u_t > u_{co} \end{cases} \tag{2.17}$$

where u_t is wind speed at time step t in m/s.

We assume a logarithmic vertical profile for wind speed [Tennekes, 1973] to adjust from measurement height to rotor height (Appendix A.4). The effects of yaw misalignment are ignored.

Wave Generation Model

To approximate the performance of an ocean observation-scale WEC, we geometrically-scaled the U.S. Department of Energy Reference Model 3 (RM3) WEC [Neary et al., 2014] and evaluated its performance in WEC-Sim, an open source computational tool for WEC simulation [Lawson et al., 2014]. The RM3 WEC, shown in Figure 2.4, is a full-scale floating point absorber with a 20 meter diameter float and 286 kW peak power output, which exceeds the generation capacity required for our use cases.

We scaled the RM3 WEC to characteristic diameters (B) of 1, 2, 3, 4, 5 and 6 meters, and analyzed these in WEC-Sim over a range sea states (i.e., significant wave heights, H_s, and peak wave periods, T_p). For each sea state, the damping coefficient (a WEC-Sim input) that resulted in the most power generated was chosen from a set of five values shown in Appendix A.5, loosely reflecting a passive optimal control strategy. While these scaled versions of the RM3 WEC are not necessarily optimized for hydrodynamic performance (e.g., a different aspect ratio might be optimal as absolute size decreases), this approach captures variations in hydrodynamic performance due to changes in WEC scale for a given sea state, which is needed for the optimization process.

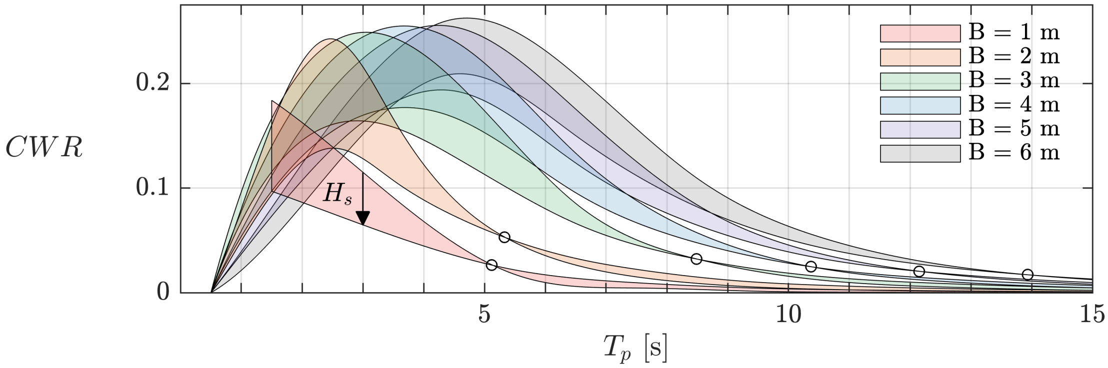

Figure 2.3: RM3 WEC-Sim results are shown by CWR as a function of T_p (x-axis), H_s (arrow, indicating upper and lower bounds) and B (color). At low T_p, CWR decreases with increasing H_s. At higher T_p (beyond inflection points denoted by $\circ$) CWR increases with increasing H_s. CWR at discrete T_p are shown as smooth contours for ease of interpretation.

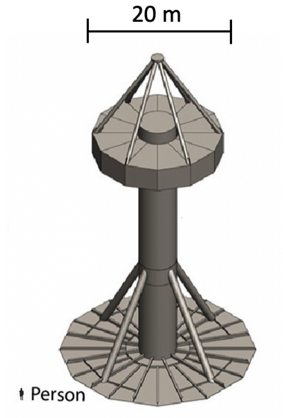

Figure 2.4: Reference Model 3 (RM3) floating point absorber WEC. Source: Sandia National Laboratories.

Figure 2.3 presents the WEC-Sim results and, therefore, performance of WECs considered in this study. These results are parameterized by the capture width ratio (CWR), a measure of hydrodynamic efficiency defined as the mechanical power generated by the WEC divided by the incident wave power. Peak CWR and resonant period increase with B, and CWR has a trivariate dependence on T_p, H_s and B. These results are linearly interpolated at unique combinations of T_p, H_s, and B to calculate CWR as a function of sea state and characteristic diameter.

P is calculated as the product of cumulative efficiencies and the wave energy flux

$$P = \eta * CWR * B\left[\frac{\rho g^2 {H_s}^2 T_p}{64\pi}\right] - hG_r \tag{2.18}$$

where η is electrical conversion efficiency (assumed to be 0.6), ρ is density of seawater (1025 kgm^{-3}), g is the gravitational constant (9.81 ms^{-2}), h is the percentage of the WEC's rated capacity used to power "house loads" (assumed to be 10%), and G_r is in W for dimensional consistency. Regardless of sea state, WEC generation is capped at G_r. We note that the deep water wave energy flux term should properly be the energy period (T_e), but this quantity is not tabulated for the available datasets and statistical corrections between T_p and T_e are site-specific [Cahill et al., 2014]. As T_p is often within 10 % of T_e, we feel that this approximation is reasonable compared to other model simplifications. We assume that biofouling does not appreciably change the WEC's response, as demonstrated for a Datawell Waverider buoy in [Thomson et al., 2015]. With exception to the parasitics of a house load and the use of T_e as opposed to T_p, this formulation is identical to the International Electrotechnical Commission technical specification for wave energy calculation [Commission, 2012].

B is calculated from Eq. 2.18 by assuming the WEC must be large enough to produce its rated power ($P = G_r$) when H_s = 4 meters and T_p = 9 s, yielding capacity factors (defined as the mean electrical power output divided by G_r) between 19% and 51%.

Diesel Generation Model

We assume the diesel generator would intermittently charge a battery storage bank that meets the 200 W instrumentation load. Specifically, we model this such that the generator switches on when S_t = $0.1S_m$, provides P_t = G_r until S_t = S_m, and switches off (P_t = 0). Diesel generators with capacities for continuous generation are uncommon and, as discussed below, continuous operation would increase the number of necessary interventions to change lubrication oil.

The temporal dynamics of diesel generation, including fuel depletion, fuel spoilage, and oil change intervals are likely to drive requirements for vessel intervention, which, in turn, have a significant effect on the cost of diesel generation. We highlight this dependence through a sensitivity analysis in Section 2.4.1.

For the baseline case, we assume fuel is stored in an 800 liter tank is used to store fuel. Rather than explicitly modeling engine efficiency, we find a relationship for diesel consumption as a function of G_r through a non-negative linear regression of consumption rate versus rated power for nine sub-20 kW diesel generators (Appendix A.2). This allows the refueling interval to be calculated directly from G_r and the logic governing P_t. An excessively large tank, however, is not feasible because diesel fuel eventually spoils [Koenig, 1999]. We, therefore, assume diesel fuel can remain in the tank for 18 months before spoiling occurs and replacement is required. Finally, we assume that the generator's lubrication oil must be changed after 250 total hours of run time, which is again calculated through the logic governing P_t based on S_m. These decisions were based on conversations with a collection of diesel generation vendors. As discussed in Section 2.5.3, through our sensitivity analysis, we find that our cost estimates are not strongly dependent on any singular assumption made here, suggesting that the assumptions are in parity with one another in terms of their influence on system operation and, consequently, cost.

We find the number of vessel interventions (n_{vi}) for the diesel resource by comparing battery replacement interval (n_{br}), refueling interval, fuel spoilage interval, and oil change interval based on temporal dynamics defined by P_t and S_m. We assume that the shortest of these intervals will set the vessel intervention interval and that tasks with longer intervals would be attended to on this defined interval. As discussed in Section 2.3.1, n_{vi} also includes unexpected interventions in addition to the identified service interval.

To calculate C_{linel} (Section 2.3.1) for the diesel resource, we must define diesel platform diameter. As mentioned in Section 2.3.1, we find that diesel generator volume is independent of G_r, such that volume is 0.22 m^3 (Appendix A.2), equating to a cubical edge length of 0.60 meters. We, therefore, assume a platform diameter of 2 meters is more than adequate for the diesel resource, which is the smallest diameter evaluated for C_{linel} (Table 2.5).

2.3.3 Optimization

The economic and energy models are used to find the lowest possible system cost for each combination of location, use case, and resource, including scenarios for each resource (e.g., automated solar cleaning), as shown in Table 2.8.

To identify a global minimum for each resource and scenario, we conduct a full parameter sweep of G_r and S_m, where each parameter is discretized into 500 evenly spaced elements, resulting in 250,000 (500^2)

Table 2.8: Resource scenario summary

Resource	Scenario	Description
Solar	Automated	Automated cleaning or soil-resistant panels
Solar	Human	Vessel intervention for cleaning
Wind	Optimistic	No failures over system lifetime
Wind	Conservative	One failure per year
Wave	Opt. Durability	No failures, 10x cost increase relative to wind
Wave	Opt. Cost	One failure per year, 4x cost increase relative to wind
Wave	Conservative	One failure per year, 10x cost increase relative to wind
Diesel	-	-

evaluation candidates. Due to differences between resources and how they are modeled, we vary the bounds of G_r and S_m. We identified these bounds iteratively, balancing output resolution against model robustness to input changes that change the location of the cost minimum. These bounds and the corresponding discretization of each axis bound are provided in Table 2.9.

Table 2.9: Optimization bounds and discretization across resources

Optimization Axis	Lower Bound	Upper Bound	Discretization
Battery	1 kWh	500 kWh	1 kWh
Solar	0.5 kW	20.36 kW	0.040 kW
Wind	0.1 kW	8 kW	0.016 kW
Wave	0.215 kW	8 kW	0.016 kW
Diesel	1 kW	15 kW	0.028 kW

Identifying the global minimum through a full parameter sweep is computationally tractable using a standard workstation. However, to reduce code development and iteration time, we executed our code on a single node of the National Renewable Energy Laboratory's High Performance Computing System. Prior to using a High Performance Computing System, we attempted using Nelder-Mead simplex optimization, a direct search local minimum finder [Lagarias et al., 1998] that should enable faster optimization. However, we found that the discontinuities in our objective spaces caused by the persistence requirement rendered the Nelder-Mead optimization unreliable.

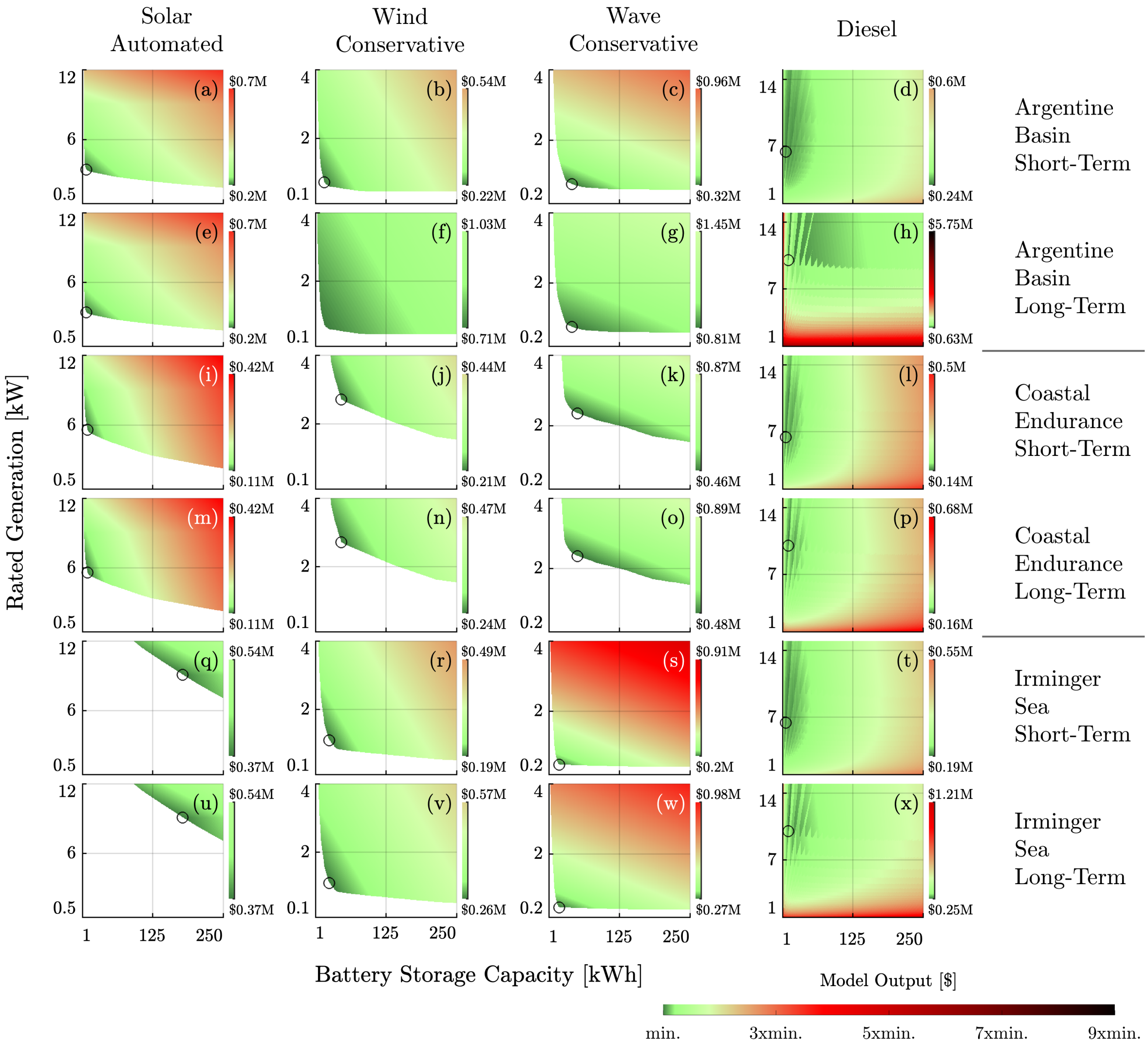

Figure 2.5: Objective spaces for four resource scenarios (columns) across all combinations of location and use case (rows). In each subplot, the axes indicate the free parameters in optimization: battery storage capacity (x-axis) and rated generation (y-axis) and the color denotes the cost difference between points in the objective space and the minimum cost (open black circle), with multiples shown on the global colorbar. For improved visualization, axes limits are smaller than the bounds of optimization provided in Table 2.9 and the colorbars are nonlinear to emphasize the gradient around the local cost minimum. Energy system capacities that cannot meet the persistence requirement are denoted by white space. Locations and resources that satisfy the persistence requirement with relatively low energy system capacities have a larger objective space gradient (i.e., wider relative cost differences between minimum and maximum costs). Total system cost in absolute terms is presented for the objective space minima in Figure 2.6 and the colorbars on individual subplots.

2.4 Results

In Figure 2.5, we present the objective spaces for total system cost (Tables 2.2 and 2.3) to power short- and long-term instrumentation use cases (Table 2.1) using four of the eight resource scenarios (Table 2.8) at all three study locations (Figure 2.1). We find that, due to the location-specific resource time series, each location has a unique objective space "perimeter" for each resource. For example, Coastal Endurance has weaker wave and wind resources and, therefore, has fewer G_r and S_m combinations that can meet the persistence requirement. Similarly, the latitude of the Irminger Sea location produces seasonal asymmetry in its solar resource, causing this location to require larger G_r and S_m combinations to meet the persistence requirement. Because the diesel resource is "on demand" and not constrained by resource availability, all combinations of G_r and S_m are possible. However, high storage and low generation combinations incur extreme costs due to the required number of vessel interventions (small generation capacities increase the oil change interval, necessitating more regular vessel intervention). The discontinuities present in the diesel objective spaces (i.e., diagonal lines) are due to G_r and S_m combinations that cause unoptimized misalignment in the possible diesel service intervals described in Section 2.3.2, causing step changes in total cost due to integer changes in the number of vessel interventions required. On the contrary, the cost for solar, wind, and wave resources monotonically increase with G_r and S_m, meaning that the global minimum always lies along the lower-left edge of the objective space perimeter. For these resources, relaxing the persistence requirement would reduce required generation and storage capacities for all combinations and, therefore, reduce total costs. Finally, we note that the influence of instrumentation service interval (i.e., short- versus long-term instrumentation) has minimal influence on the layout of the resulting objective objective spaces. This does, however, have a larger impact on the value of the minimum cost in certain situations, and the influence of various modeling assumptions, as identified in the ensuing sections.

In Figure 2.6, we present the minimum estimated costs for all combinations of use cases, resource scenarios, and locations. Cost-optimal generation and storage capacities, as well as diagnostics from time-domain simulations are also provided. The costs presented are simply the results of the model, and given the uncertainty in model inputs and the model itself, only order of magnitude comparisons and conclusions are relevant. Depending on the location, use-case, and resource scenario, total costs range between \$107,000 and \$808,000. The lowest costs correspond to the solar resource (particularly the automated cleaning scenario)

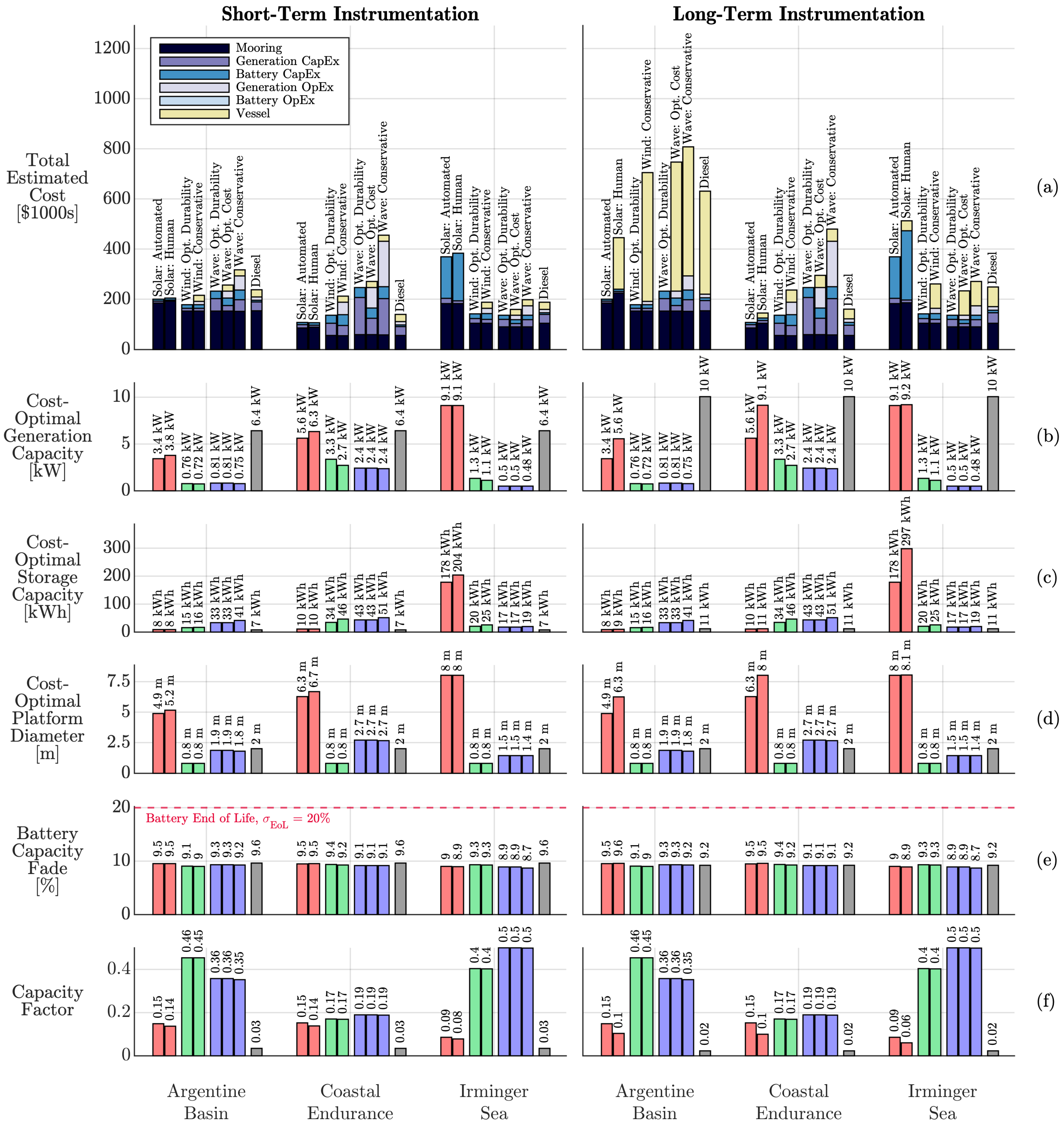

Figure 2.6: Cost and performance of cost-optimal in-situ generation for short-term instrumentation (left) and long-term instrumentation (right), across all study locations (x-axis), for all eight resources and scenarios (annotated). Total estimated cost in thousands (a) is broken into six cost categories. Beneath this panel, the resources are indicated by color (solar: red, wind: green, wave: blue, diesel: grey). Cost-optimal generation (b), storage capacities (c) and platform diameter (d) are provided. Selected time-domain diagnostics, including the amount of capacity fading endured by the battery bank relative to the battery's end of life (e) and capacity factors (f) are provided. Numerical values for (a) are provided in Appendix A.6.

at the Coastal Endurance location, a location that is less prone to seasonal solar asymmetry due its latitude and has lower mooring costs due to its shallow water depths. Costs to power short-term instrumentation for each combination of location and resource are lower than for long-term instrumentation due to the additional vessel intervention necessary to maintain the power system (i.e., long-term instrumentation has no service interval to leverage). As consequence, the greatest cost variability between the short- and long-term instrumentation use cases occurs in Argentine Basin, which is the location that is furthest from shore. In addition to the cost of vessel intervention, mooring system costs often comprise a high proportion of total estimated cost, particularly for the solar resource and short-term use case.

We find that cost-optimal power system capacities vary significantly across the eight resource scenarios and, to a lesser extent, across locations and use cases. Cost-optimal generation capacities are lower for the wave and wind resources (< 3.5 kW for all cases, and < 1 kW at locations with strong resources) and larger for the solar and diesel resources (> 3 kW, in certain cases exceeding 9 kW). In general, cost-optimal energy storage capacities are less than 55 kWh—which is roughly similar to the capacity of the current generation of electric passenger vehicles—and are smallest (< 12 kWh) for the diesel and solar resources. The sole exception to this is for solar in Irminger Sea, which requires battery banks > 175 kWh for seasonal storage in winter months.

Across all combinations of use case, resource and location, we find that battery capacity degradation ("fading") as a percentage of nominal capacity (Figure 2.6d) is well under the baseline for end of life, σ_{EoL}, meaning battery replacements are not required ($n_{br} = 0$) and battery-related operational costs ($\mathrm{OpEx}_{\mathrm{S}}$) are, therefore, zero for all combinations. The implications of this are discussed in Section 2.5.4. Capacity factor (Figure 2.6e), a diagnostic proxy for generation uptime, varies predominantly by resource, such that the solar resource ranges from 6% to 15%, the wind resource from 16% to 45%, the wave resource from 19% to 50%, and the diesel resource between 2% and 3%. With exception to diesel, the upper limits of these ranges are consistent with capacity factors commonly found or expected in terrestrial and utility scale applications. However, the lower limits fall below common capacity factors due to the misalignment between resource availability and deployment location inherent to our selected datasets, which is less likely to occur in utility settings.

2.4.1 Sensitivity Analysis

As shown in Figure 2.6, locations, resource and assumptions about resource conversion (e.g., durability) influence total cost. Here, we present a sensitivity analysis that describes the influence of other assumptions underpinning our economic and energy models. Figures 2.7 to 2.10 show model sensitivity across all combinations of location and use case for the solar resource (Figure 2.7), wind resource (Figure 2.8), wave resource (Figure 2.9), and diesel resource (Figure 2.10). Costs are referenced to the "baseline" value in Figure 2.6. To differentiate the effect of sensitivities by use case, the short- and long-term instrumentation sensitives are shown in distinct colors. An exception is the solar resource, where color differentiates the automated versus human cleaning scenarios under the long-term use case. For the wind and wave resource, these figures show sensitivities under the conservative scenarios, as these scenarios are more sensitive to model input assumptions than the more optimistic cost and/or durability scenarios.

The top row of each figure shows sensitivities to input parameters that are specific to that resource (e.g., solar panel efficiency). The subsequent rows show sensitivities to input parameters that apply to all resources, such as ones involving the battery (e.g., battery cell cost), instrumentation (e.g., persistence requirement), vessel intervention (e.g., maintenance time), and the mooring system (e.g., water depth). These parameters were selected to assess assumptions, as well as to identify the influence of potential innovations that could enable significant future cost reductions. All parameters are discussed in Section 2.3. The "WEC Cost Multiplier" refers to the multiplier applied to the cost of wind energy to find α_{wec}, which has a baseline conservative value of 10. To evaluate sensitivity, each parameter was evenly discretized into ten values and all other parameters were held constant at their baseline value. In Appendix A.7, we present sensitivities to additional sensitivity parameters that have less impact on total estimated costs.

Across use cases, locations and resources, total cost is most sensitive to assumptions about the number of generation system failures, lifetime, and instrumentation power draw. Due to the distinction between regular (i.e., six-month) site access (short-term instrumentation) and no site access (long-term instrumentation), described in Sections 2.2.2, we note that some sensitivities are specific to use case. For example, vessel cost and maintenance time are important sensitivities for short-term use cases, while offshore support vessel cost and distance to coast are important for long-term use cases, as detailed in 2.3.1.

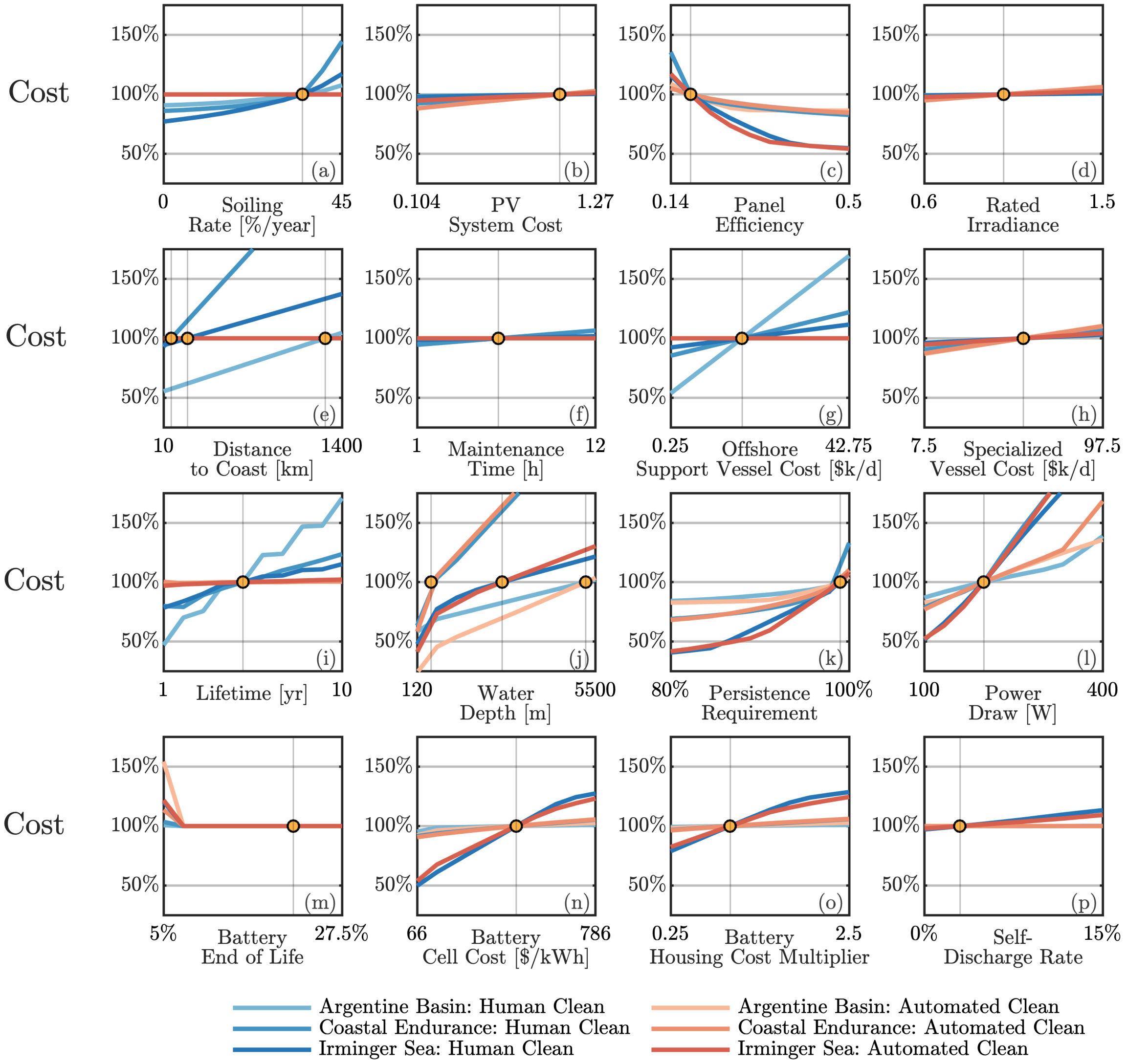

Figure 2.7: Cost sensitivities for powering the long-term instrumentation use case at all locations with solar under the automated and human cleaning scenarios. Sensitivities are shown by changes in select parameters (x-axes) versus percentage of baseline cost (y-axes). Baseline values are indicated by orange data points. Certain sensitivity parameters—depth, maintenance time, distance to coast—have a different baseline value for each location.

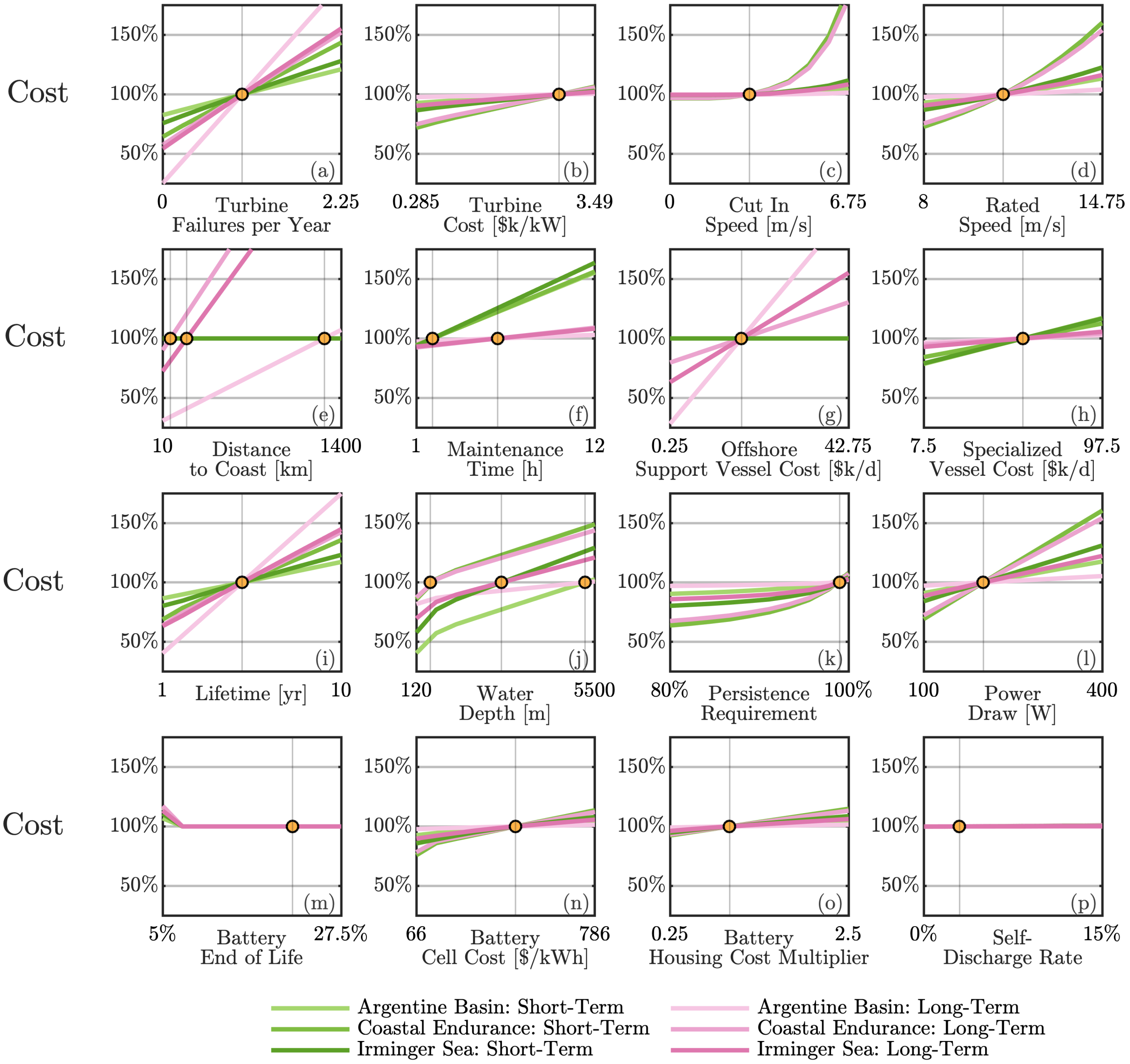

Figure 2.8: Cost sensitivities for powering all combinations of location and use case with wind under the conservative scenario. Sensitivities are shown by changes in select parameters (x-axes) versus percentage of baseline cost (y-axes). Baseline values are indicated by orange data points. Certain sensitivity parameters—depth, maintenance time, distance to coast—have a different baseline value for each location.

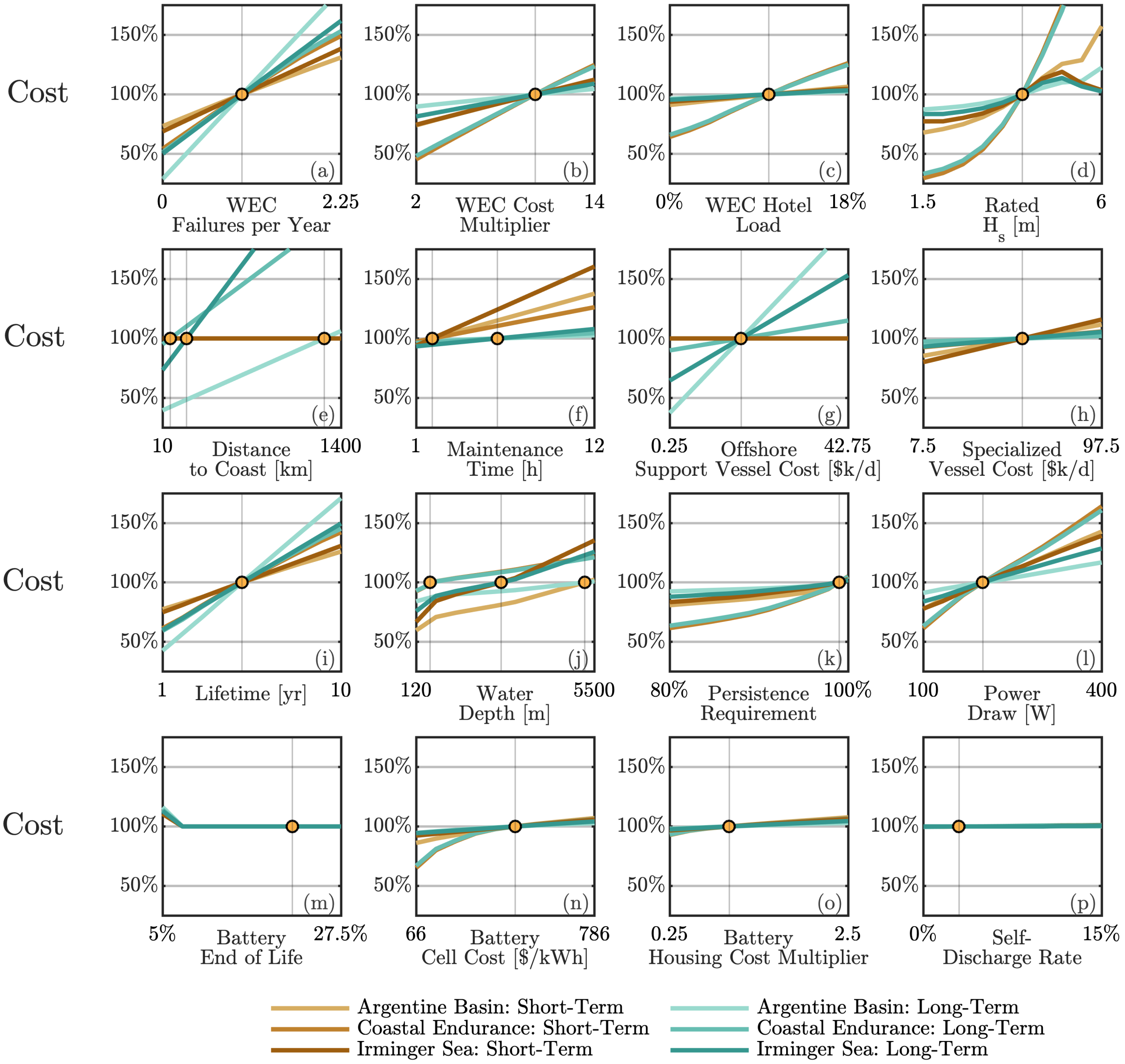

Figure 2.9: Cost sensitivities for powering all combinations of location and use case with wave under the conservative scenario. Sensitivities are shown by changes in select parameters (x-axes) versus percentage of baseline cost (y-axes). Baseline values are indicated by orange data points. Certain sensitivity parameters—depth, maintenance time, distance to coast—have a different baseline value for each location.

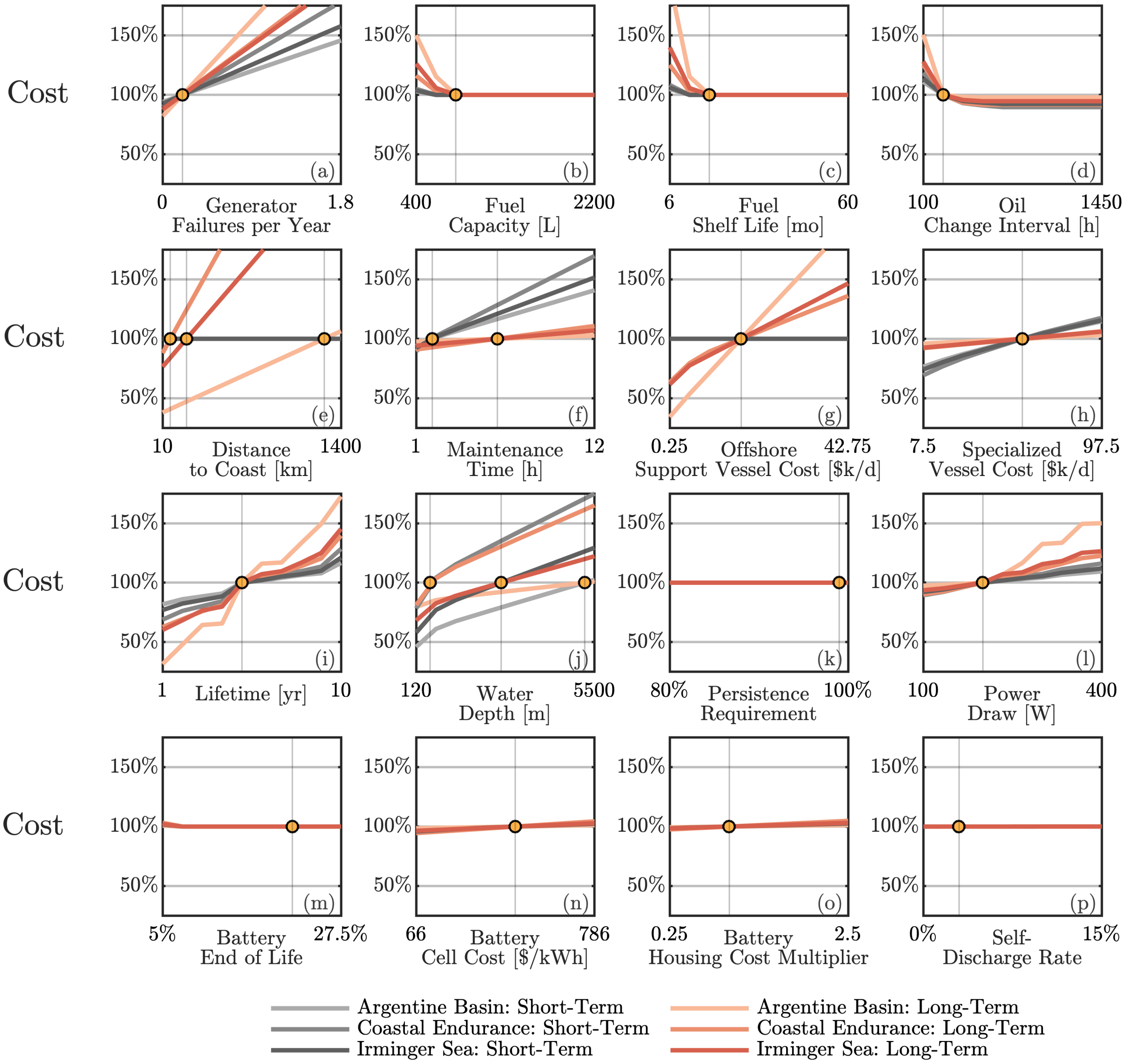

Figure 2.10: Cost sensitivities for powering all combinations of location and use case with diesel generation. Sensitivities are shown by changes in select parameters (x-axes) versus percentage of baseline cost (y-axes). Baseline values are indicated by orange data points. Certain sensitivity parameters—depth, maintenance time, distance to coast—have a different baseline value for each location.

2.5 Discussion

Here, we interpret our results by resource, presenting insights into the development of cost-effective in-situ powered ocean observation systems. We find that the economic feasibility of the resources evaluated in our study—solar, wind, wave and diesel—vary foremost by factors involving geographical location and resource availability, as well as factors that influence the cost of vessel intervention.

2.5.1 Solar

Reflecting the wide use of solar generation for in-situ powered observation systems, we find that the solar resource is cost-effective due to a negligible likelihood of failure and relatively low module costs. We find that the solar resource is particularly cost-effective for locations at lower latitude (Coastal Endurance: 44°35'N and Argentine Basin: 42°30'S, Figure 2.1). For Coastal Endurance, estimated solar costs are the lowest among all cases considered due to this location's shallow water depth (which limits the mooring cost, even for a relatively large platform) and consistent solar resource availability (Figure 2.6a). At Argentine Basin, the solar resource is even more consistent, resulting in lower required generation and storage capacities (Figures 2.6b and 2.6c), but higher total costs due to the increased cost of mooring in a deep (> 5000 m) water location. These considerations suggest that, in general, solar power suitability improves with shallower water depths and latitudes closer to the equator than are included in our analysis.

On the contrary, solar resource costs are approximately twice the cost of other resources at Irminger Sea, the location with the highest latitude (60°N), reflecting the challenge presented by seasonal irradiance asymmetry. Here, large storage (> 150 kWh, Figure 2.6c) and generation (> 7.5 kW, Figure 2.6b) capacities are required to meet the baseline persistence requirement. More so than for other resources, increasing solar generation capacity substantially increases the cost of the mooring system, as shown in Table 2.5 and equations 2.15 and 2.16. As a result, the solar resource is sensitive to water depth (Figure 2.7j) and panel efficiency (Figure 2.7c) since both influence mooring system cost. Similarly, the solar resource is more sensitive to battery costs at Irminger Sea than other locations (Figures 2.7n and 2.7o), highlighting the system's dependence on energy storage to meet the persistence requirement over winter months at high latitude. For the same reason, the solar resource at Irminger Sea is more sensitive to the self discharge rate of the battery (Figure 2.7p).

At a high level, this suggests that, in addition to powering observations at lower latitudes, the cost of solar generation is likely to benefit from innovations that reduce battery cost, as well as those that improve panel efficiency, allowing reduced mooring system cost. Similarly, designing solar generation platforms that can "blow down" may reduce mooring costs and improve economic feasibility. We also find that, among resources, the solar resource is most sensitive to the persistence requirement (Figure 2.7k) due to reductions in generation capacity with lesser persistence, suggesting that solar may be most cost-effective for powering observation applications with lower (< 80%) or deferrable persistence targets. Similar considerations apply to the sensitivity to power draw (Figure 2.7l), meaning that solar is likely to be more cost-effective for deployments with lower (< 100 W) power requirements and cost-prohibitive for powering observations with high (> 300 W) power needs. Finally, our results suggest that the solar resource has the strongest financial potential for longer-term observations among the resources evaluated, as—under the automated cleaning scenario—estimated costs do not increase with lifetime (Figure 2.7i) due to the longevity and durability of solar panels.

We find that, in the long-term use case, the automated cleaning scenario produces substantially lower total cost estimates than the human cleaning scenario (Figure 2.6a). This is most pronounced for Argentine Basin, where vessel intervention with an extended transit distance (Figure 2.1a) is necessary to clean panels. Additionally, the human cleaning scenario is disadvantageous for Irminger Sea, where the soiling that occurs between the two-year cleaning interval exacerbates this location's seasonal irradiance asymmetry (due to being at high latitude), necessitating an even larger battery bank (Figure 2.1c). On the contrary, our results suggest human cleaning may be a viable strategy at locations that are nearshore or for deployments that have regular site access for instrumentation needs (e.g., short-term instrumentation). This, however, depends on soiling rates (Figure 2.7a), which are uncertain in ocean settings and are a recommended area of future study.

2.5.2 Wind

We find that, for both the wind and wave resources, costs are primarily dependent on durability, electrical power demand, and location-related factors such as power density and distance to coast. Costs for these resources are foremost sensitive to durability assumptions, such as turbine failures per year (Figures 2.8a and 2.9a) and the optimistic versus conservative durability scenarios (Figure 2.6a). This suggests that generation system durability is key to enabling wind- and wave-powered observations.

Geographic sensitivities are primarily due to resource availability and distance to coast. We find that if the wave or wind resource is strong and the deployment is a short distance from shore, as for the Irminger Sea location (Figure 2.1a), total costs are relatively low and insensitive to use case and/or scenario. In contrast, at Coastal Endurance, which is nearshore and lower latitude, the relatively weak wave and wind resources at this location necessitate larger generation (Figure 2.6b) and storage (Figure 2.6c) capacities, which also increase turbine/WEC refurbishment costs. Consequently, only wind and wave systems with ideal durability are cost-comparable to solar and diesel at this location. Wave generation, in particular, does not achieve cost parity at this location due to the high cost of a larger WEC, even under the optimistic durability scenario. Alternatively, at Argentine Basin, which is far from shore but has strong wave and wind resources, vessel transit is the dominant operational cost, such that eliminating device failures (i.e., optimistic durability) or powering instrumentation that is routinely maintained (i.e., short-term instrumentation) results in substantially lower costs than other scenarios and use cases.

At a high level, this suggests that wave and wind may be cost-effective options in high latitude locations, where seasonal irradiance asymmetries can prohibit solar. When this is the case, the differentiating factors for wave and wind foremost involve durability or distance to coast (Figures 2.8e and 2.9e), and, secondarily, the relative power densities of the wind and wave resources available at the site. For example, smaller WECs are viable at Irminger Sea due to the strength of this location's wave resource, which lowers wave energy's total estimated cost beneath wind, whereas the opposite is true at Argentine Basin, where the strength of the wind resource enables smaller wind turbines. Another differentiating factor between these resources may be the design of their mooring systems. WECs have the operational benefit of most feasibly tolerating "blow down", which may increase survivability in extreme events, whereas wind turbines may have the benefit of using a spar surface float geometry that reduces diameter and, therefore, frontal area and drag forces.

Other cost sensitivities are similar across the wind and wave resources. For example, costs are linearly dependent on system lifetime (Figures 2.8i and 2.9i) due to the linear relationship between device failures and lifetime under the conservative scenarios. Additionally, relaxing the persistence requirement reduces costs (Figures 2.8k and 2.9k) and costs are sensitive to power draw (Figures 2.8l and 2.9l), meaning changes in sensing objectives affecting electricity requirement will have direct impact on power system costs. However, both of these sensitivities (persistence and power draw), for wind and wave, are not as significant as for the solar resource (Figures 2.7k and 2.7l) for a variety of nonlinear and inter-related factors, including location-specific differences in resource time profiles and varying cost gradients associated with generation capacity (e.g., mooring system cost).

Finally, we find that, for both wind and wave, costs are reduced by lowering the generator's rated condition (i.e., rated speed for wind, Figure 2.8d, and rated significant wave height for wave, Figure 2.9d). We caution that this is a consequence of our assumption that turbine and WEC costs are linear with G_r. In practice, economies of scale mean that unit generation costs increase for smaller capacities. However, this finding, that lowering maximum power output does not reduce costs, also highlights how meeting persistent sensing objectives with wind and wave resources is more contingent on low power continuity than peak power output. This is exemplified by the wave resource's sensitivity to WEC hotel load (Figure 2.9c), which is effectively a "cut in" condition, acting as the minimum required generation (as a percent of rated power output) for the WEC to produce a net positive power output. When the hotel load is reduced to zero, total costs at the location with the weakest wave resource reduce by $\sim$40%. This suggests that WEC advancements that lower or eliminate this cut in condition may greatly improve the breadth of locations in which wave-powered observation is economically feasible.

2.5.3 Diesel

We find that the diesel resource, like wind and wave, primarily depends on assumptions that influence vessel intervention, such as generator failures (Figure 2.10a), distance to coast for the long-term use case (Figure 2.10e), and maintenance time for the short-term use case (Figure 2.10f). In particular, the diesel resource is vulnerable to high costs when used to power the long-term use case at Argentine Basin (Figure 2.6a) due to a lack of site access and substantial transit distance for generator maintenance. In all other circumstances, the diesel resource is cost-comparable to other options.

Unlike the other resources, costs for the diesel resource are dependent on assumptions about which factor (fuel depletion, fuel spoilage, or oil change intervals) sets the vessel intervention interval. We find that vessel intervention is consistently set by the oil change interval (Figure 2.10d), which has a baseline value of 250 hours of generator runtime before requiring intervention. Increasing this, such that intervals for refueling or spoilage set the vessel intervention interval, causes total cost estimates to drop by only 2 - 10% across locations for the two use cases. Similarly, small ($\sim$25%) decreases in fuel capacity and fuel shelf life result in modest (< $\sim$15%) increases in total estimated cost (Figures 2.10b and 2.10c). This indicates that, under our formulation, that none of these three considerations for vessel intervention (refueling, fuel spoilage, and oil change) dominate by a margin considerable enough to negate the others.

Overall, this suggests that the diesel resource is cost-comparable to the other resources at nearshore locations (e.g., Coastal Endurance) or for powering instruments that have regular service intervals (i.e., short term instrumentation). If it is possible to reduce each of the aforementioned vessel intervention requirements, diesel may be cost-comparable in other circumstances as well.

In addition to total cost, we find that the oil change interval also influences cost-optimal diesel generation and battery storage capacities, such that large (> 5 kW) generators are cost-optimal (Figure 2.6b), as they charge the battery faster, reducing runtime and prolonging intervention for oil change. This has the additional influence of decreasing cost-optimal storage capacity to less than 11 kWh across all locations and use cases (Figure 2.6c).

Unlike solar, wind, and wave, the diesel resource is not the lowest total estimated cost in any of the six combinations of use case and scenario provided in our baseline results (Figure 2.6a). However, our results suggest that diesel generation has unique attributes that may benefit the future capabilities of in-situ powered observation in other ways.

The diesel resource is least sensitive, among resources, to power draw (Figure 2.10l), indicating that diesel may be most cost-effective for sensing applications with higher power requirements. Additionally, due to the relative compactness of diesel generation and our finding that generator volume is invariant with G_r (Appendix A.2), platform space requirements, which set mooring system costs, minimize for the diesel and wind resources (Figure 2.6b). Due to the uncertainty of spar design for this generation scale (Appendix A.1), diesel generators may involve simpler and lower-cost mooring systems than the other resources involved in this study. Our finding that battery storage requirements are lowest for the diesel resource (Figure 2.6c) may similarly aid mooring system design. Separately, reduced energy storage requirements for diesel generation adds robustness to capacity fading, observed through lower sensitivity to reducing the battery's end of life (Figure 2.10m). As discussed in 2.5.4, although we find that battery replacements are not required (Figure

2.6d), this is provisional and dependent on extrapolating the degradation model provided in [Xu et al., 2016] to colder temperatures, which should be a focus area of future research. Resources with smaller battery storage requirements may be more economically robust to unmodeled degradation dynamics inherent to this application in part because it may be easier to add a factor of safety to these storage capacities. Additionally, in the event that regular battery replacement is required, the cost and transport requirements of replacement cells would be lower, relative to resources with larger battery storage requirements.

These potential advantages, however, must be balanced against the environmental impacts caused by diesel extraction and transportation, including the risk of chemical impacts if fuel storage tanks are ruptured. While this risk is unique to the diesel resource, further work is needed to identify the life-cycle and ecological impacts of all resource options in contrast to their intended benefits for ocean observation.

2.5.4 Battery

Our results suggest that battery durability is of lesser concern than generation source durability in this application. Using Xu et al.'s semi-empirical model, we find that capacity fading following five years of cycling is between 8.7% and 9.6% of nominal storage capacity, well beneath σ_{EoL} (Figure 2.6e), which is typically quantified as 20%, and is expected to become > 30% in the next decade [Xu, 2020]. Furthermore, due to nonlinear dynamics—degradation rate slows with increasing capacity fade—we find that even as lifetime increases to ten years (Figures 2.7i to 2.10i), capacity fading remains beneath σ_{EoL}. These benefits of battery longevity, which are an unexpected outcome of our analysis, are due to the relatively high energy-to-power ratios (i.e., kWh of battery capacity divided by kW of power requirement) of the batteries used in this application, resulting from the need to bridge solar, wind, and wave energy intermittencies and meet the 99% persistence requirement. As energy-to-power ratio increases, discharge cycles become smaller in normalized amplitude and/or have larger periods, causing degradation to be driven by calendar aging mechanisms—such as average state of charge—rather than cycling mechanisms [Omar et al., 2014] [Xu et al., 2016]. This results in lower amounts of capacity fading and longer battery lifetimes relative to power systems with smaller energy-to-power ratios. The diesel resource, which is not constrained by renewable availability, has relatively smaller energy-to-power ratios and consequently slightly larger capacity fading 2.6e. However, these ratios are still not low enough to cause degradation to be driven by cycling mechanism.

Overall, we observe much lower amounts of capacity fading and longer battery lifetimes across all resources relative to power systems with much smaller energy-to-power ratios (e.g., battery electric vehicles), such that there is consistent (i.e., within 1%) capacity fading across our results (Figure 2.6e), with average state of charge being the primary driver of variation.

However, we caution that our conclusions regarding battery longevity are provisional, and depend on the extension of Xu et al.'s model to new applications. For example, Xu et al. apply their model to a case study evaluating batteries with energy-to-power ratios between 0.25 and 4, whereas the energy-to-power ratios in our analysis are significantly larger (> 85). Additionally, as described in Section 2.3.2, battery temperatures between 0 °C and 10 °C are likely across the locations evaluated in our study, and temperatures beneath 15 °C are known to accelerate aging in lithium-ion batteries. Although it would be most accurate to model degradation effects at such temperatures, lack of test data precludes extrapolating Xu et al.'s model to temperatures < 15 °C, and, to our knowledge, there is not a comparable model in the literature that quantifies capacity fading under irregular cycling at such temperatures. We note that (1) the influence of accelerated degradation due to warmer temperatures (up to 35 °C) in our model does not result in any economic impact, in large part due to the significant buffer between capacity fade and σ_{EoL} under baseline assumptions (Figure 2.6d), and (2) temperatures < 15 °C are known to slow calendar aging mechanisms [Molaeimanesh et al., 2020], which are the dominant driver of degradation in this application. However, cold temperatures cause other issues for lithium-ion cells, such as increases in internal impedance and poor performance in charging [Zhang et al., 2003] [Jaguemont et al., 2016]. Thus, future battery research should explore degradation mechanisms under irregular cycling in both high energy-to-power ratio and relatively low-temperature applications (i.e., -5 °C - 15 °C). If such temperatures compromise battery longevity, thermal management strategies that do not require supplementary power consumption, such as utilizing discarded electricity for residual heating, may be cost-effective, both due to the high cost of vessel intervention to replace batteries and the sensitivity of total system cost to power draw (Figures 2.7l to 2.10l).

2.5.5 Future Work

In addition to the recommendations presented above, we present ideas that may help to further enable effective and responsible in-situ powered ocean observation. A study that considers the cost and suitability of

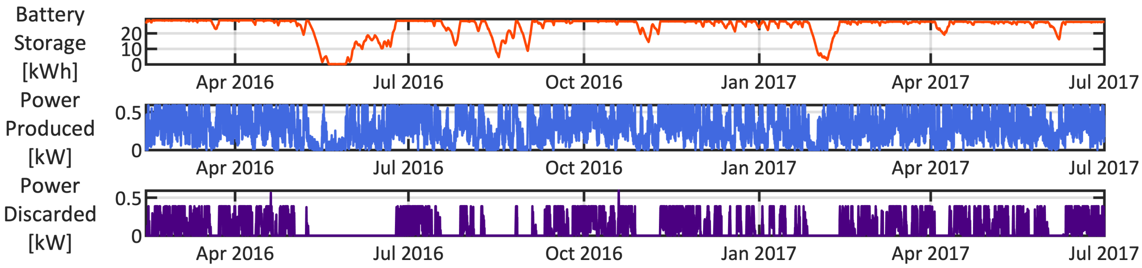

Figure 2.11: Simulated battery storage, power produced and power discarded to power short-term instrumentation under the conservative WEC scenario at the Southern Ocean location. To emphasize resource intermittency, only sixteen months of the five year time series are shown. It is often the case during this period that the power discarded is larger than the load being met (0.2 kW).

hybrid generation (i.e., multiple resources connected to a single battery bank) would be a natural extension of this analysis, as hybrid solutions have been shown to improve robustness by utilizing multiple intermittent resources in terrestrial micro-grids [Holdmann et al., 2019]. Importantly, this may help to reduce the total generation and storage capacities required, thereby reducing surface float dimensions and the cost and complexity of the float's mooring system.

Another practical strategy for reducing generation and storage capacities is to use real-time resource forecasts to adaptively manage energy consumption. This strategy would involve incorporating flexible loads (i.e., a controllable suite of instruments) and real-time energy forecasts to adaptively manage consumption. For the specific case of wave energy, as shown by the time series in Figure 2.11, the periods of low wave resources in June 2016, September 2016, and February 2017 in one of our cost-optimal wave simulations drive minimum required power system capacities. This means that significant generation must be discarded at other times because power generated exceeds both instrumentation needs and available battery storage. By forecasting these events in real time, that discarded power could be used for additional, flexible loads. This would also enable reductions in required battery capacity (and, therefore, volume and mass), reducing battery cell and housing costs, as well as the complexity of system deployment. This motivates the analysis presented in Chapter 3.

Ocean observations could, in theory, also be met by harnessing ocean currents, using dedicated cables, or relying on batteries. None of these cases are presented here because their costs are much higher. It is trivial to demonstrate that the cost of laying a dedicated cable or the cost of repeated vessel interventions to replace batteries for these use cases is orders of magnitude higher than for the in-situ generation approaches. At the locations considered, ocean currents are relatively weak and infeasibly large turbines would be required to meet the load cases. This approach might, however, be feasible for sensing in western boundary currents or other ocean currents with average speeds > 1 ms^{-1}. Evaluating turbine size at locations with energetic currents would be an effective starting point for a commensurate cost-based analysis of current-powered ocean observation.

Finally, future analysis should rigorously consider the environmental and intersectional impacts of in-situ powered observation. The examples we selected to motivate our study relate to the safety of vulnerable human populations [Kesavakumar et al., 2013], climate change [Kohler et al., 2015] [Sastri et al., 2019], ecosystem health [Klemas, 2013], and the extinction crisis [Goodwin et al., 2019] [Sheehan et al., 2020] [Vonnahme et al., 2020] [Van Dover et al., 2017] [Van Dover, 2014]. These widespread challenges depend on solutions that address root causes without amplifying intermediate stressors, (e.g., pollution, waste, natural resource extraction from both environments and marginalized communities, habitat destruction, exploitative labor practices, and impacts on subsistence fishing). While the work in this study focuses singularly on financial cost, further transdisciplinary research that considers the holistic benefits, consequences, externalities, and alternatives associated with improving the capabilities of ocean observations is needed to responsibly address these humanitarian and ecological challenges.

2.6 Conclusion

In this chapter, we present a comparative techno-economic analysis of resource options for powering in-situ ocean observations, including solar, wind, wave and diesel generation. We accomplish this through a techno-economic model that utilizes time domain simulation and optimization to identify cost-optimal generation and storage capacities and total estimated costs across resources.

We selected three locations (Argentine Basin, Coastal Endurance, and Irminger Sea) from the National Science Foundation's Ocean Observatories Initiative (OOI) with similarly continuous, temporally-resolved resource data, but contrasting distance to coast, water depth, and resource power density. Two oceanographic use cases that differentiate the influence of a service interval for instrumentation (short- and long-term instrumentation) are evaluated, both of which assess powering a 200 W load at 99% persistence for five years. For the solar resource, we consider two panel cleaning scenarios and, for the wind and wave resources, we consider hypothetical durability scenarios, which all differentiate the necessity of vessel intervention for power continuity. For the wave resource, we consider an additional hypothetical device cost scenario, as the cost of WECs are uncertain at this time and are, therefore, based on conservative multipliers on the cost of kW-scale wind turbines. To examine how our assumptions impact cost projections, we present a sensitivity study on various input parameters.

We find that cost-optimal energy system capacities depend on the resource being used, such that generation capacities are lower for the wave and wind resources (< 3.5 kW, and < 1 kW at locations with strong resources) and larger for the solar and diesel resources (> 3 kW, in certain cases exceeding 9 kW). With exception to using solar energy at high latitude, which requires a large (> 175 kWh) battery bank to bridge seasonal asymmetry, battery storage banks < 55 kWh are cost-optimal across resources and locations. The corresponding range of power system costs over the deployment duration is between \$107,000 and \$808,000. We find that solar is a cost-effective option in low-latitude and shallow water environments, where the seasonal continuity of irradiance and lower mooring system costs reduce total estimated costs. Outside of this, in deep water and high-latitude scenarios, the wind, wave and diesel resources are cost comparable, depending on assumptions impacting vessel intervention (e.g., durability, instrumentation maintenance cycles) and resource power density. Future efforts to enable high-latitude in-situ powered ocean observation would benefit from an emphasis on device durability and minimizing vessel intervention, whereas efforts to power equatorial observations may benefit from improving solar panel efficiency and reducing the mooring system cost of larger platforms.

Future analysis may also benefit from (1) considering hybrid generation and (2) applying resource forecasts to manage power, both of which may further optimize and reduce the power system capacities required for enhanced in-situ ocean observation. Additionally, future research will benefit from intersectional, transdisciplinary efforts that evaluate the holistic benefits, consequences, externalities and alternatives associated with improving the capabilities of ocean observation, in particular pertaining to the safety of vulnerable human populations, the climate crisis.

Chapter 3

Forecast-Based Stochastic Optimization for Wave Energy Conversion and Storage

3.1 Introduction

Stand-alone renewable energy systems can provide co-located electricity generation for various applications in open ocean [Kohler et al., 2015] [Copping et al., 2018] [Whitt et al., 2020], rural and remote settings [Hossain et al., 2015] [Chauhan and Saini, 2015] [Mandelli et al., 2016] [Muh and Tabet, 2019], desert environments [Shaahid and Elhadidy, 2007], the arctic [Boute, 2016] [Janzen et al., 2019], and other locations that are difficult to reach with centralized (e.g., utility grids) and conventional (e.g., fuel-based) power sources. Due to the intermittency of renewable resources, such systems require energy storage to meet persistent loads, making battery sizing [Yang et al., 2018] and real-time energy management [Robert et al., 2018] key considerations for system optimization. Incorporating resource forecasts into these optimization strategies can improve performance by providing advance knowledge of power availability [Ahmed and Khalid, 2019]. At the utility and micro-grid scales, this has been demonstrated for profit maximization [Exizidis et al., 2017] [Khalid et al., 2018], cost savings [Mazzola et al., 2017], dispatch scheduling [Kaur et al., 2016] [Gu et al., 2016], improved reliability [Wang et al., 2016], minimizing battery storage requirements [Khalid and Savkin, 2014], and sizing spinning reserves [Gil et al., 2010]. However, for comparatively smaller stand-alone renewable energy systems that lack a connection to a distribution grid, the benefits of forecasting have undergone less examination. Such systems may exhibit more flexible load characteristics and have a single source of power generation, as well as environment-specific functional requirements and deployment objectives.

Here, we consider the specific case of using ocean wave forecasts to optimize the energy management of a stand-alone wave-powered ocean observation system. Among stand-alone renewable energy systems, ocean-based applications are a relevant test case for such analysis because minimizing the energy system's size is essential to enabling its use in ocean environments. Unlike land-based applications, where the availability of space may enable "oversizing" the energy system (i.e., adding a factor of safety to the capacity of generation or storage components to ensure power is constantly available), oversizing the energy system on an ocean platform substantially increases deployment difficulty, the cost and complexity of its mooring system [Harris et al., 2004], and the magnitude of the structural loads in extreme waves. These considerations necessitate solutions that can address resource intermittency without oversizing generation and storage capacities. One possibility is to use real-time resource forecasts to reduce capacities required for persistent power availability. This can also be interpreted as using forecasts to increase the amount of energy consumption possible in comparison to an equivalently-sized energy system that does not utilize forecasting. Due to the uncertainty inherent in wave energy forecasting [Janssen, 2008] [Reikard and Rogers, 2011] [Widén et al., 2015], stochastic optimization methods are necessary.

In this paper, we describe and analyze a forecast-based stochastic optimization method suitable for an integrated oceanographic instrumentation package powered by a battery-backed wave energy converter. Our optimization hinges on the ability to change power consumption in real time (i.e., demand management) by adjusting which sensors are operating. To evaluate the benefits of forecast-driven decisions regarding power consumption, we simulate a variety of decision schemas, WEC sizes, and battery capacities using time-resolved wave resource datasets.

Section 3.2 provides background on wave-powered ocean observation and the example wave-powered ocean observation system, the data used to run our simulations, and our selected class of stochastic optimization methodology. Section 3.3 describes the objective function of our optimization, models for energy storage and conversion, and our simulation strategy. Section 3.4 presents the simulation results, including time series outputs, performance metrics and a sensitivity analysis. The implications of the results are

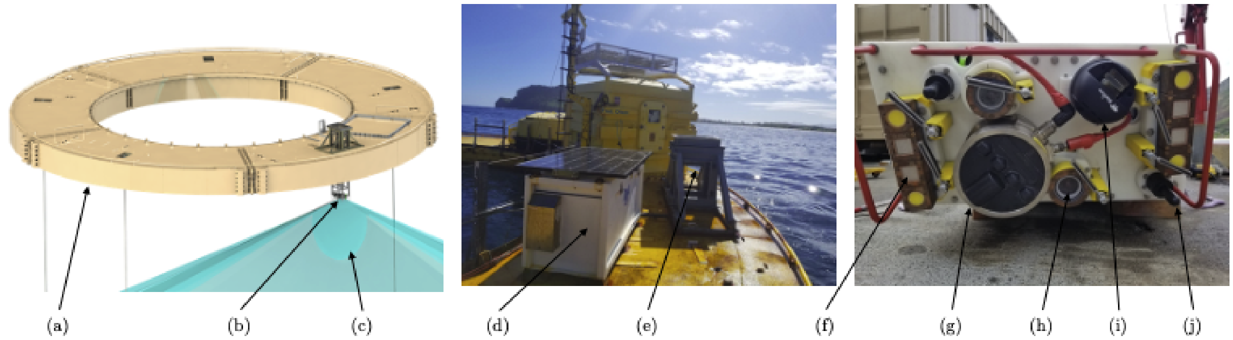

Figure 3.1: A schematic and images of the WAMP, with annotations showing the WEC hull (a), location of the instrument head (b), sensor field of view (c), battery bank and control computer (d), instrument support tower (e), and instrument head, which integrated strobe lights (f), a multibeam sonar (g), optical cameras (h), an acoustic camera (i), and hydrophones (j). The solar panel positioned atop the battery bank was used to maintain the WAMP's control system during extended periods of calm seas [Joslin et al., 2019].

discussed in Section 3.5.

3.2 Background

This section provides additional background, including wave-powered ocean observation and the system our analytical model is motivated by, the time-resolved datasets used, and the class of stochastic optimization drawn from in our methods.

3.2.1 Wave-Powered Ocean Observation

To date, electrical power availability has constrained the range, endurance and/or scope of ocean observations, such as those conducted by battery-powered buoys, cabled observatories, and vessel-based field campaigns, as summarized in Section 2.1. Incorporating stand-alone renewable generation technologies into ocean observation systems may change this paradigm, allowing distributed, flexible, and autonomous measurements with fewer power or payload constraints [Whitt et al., 2020]. Initial successes in this area have involved solar energy harvesting (e.g., measurement buoys [Kohler et al., 2015], electrical systems on Wavegliders [Manley and Willcox, 2010]), but the relatively low energy density of solar radiation still limits absolute energy harvesting capacity and payload capabilities. This motivates interest in energy sources with higher energy density, such as wave energy, to power ocean observations. In this context, wave energy

Table 3.1: Comparison of real-world and simulated WAMPs.

	WAMP	**Analytical Model**
Location	Kaneohe, HI, USA (WETS) 21°27.940 N, 157°45.040 W	Kaneohe, HI, USA (WETS) 21°28.642 N, 157°45.346 W
Dates (duration)	15 October 2018 – 28 January 2019 (105 days)	6 July 2017 – 19 September 2017 (75 days)
Power consumption	Mean power during uptime: 547 W Mean power over full duration: 445 W	Full-power mode: 600 W Medium-power mode: 450 W Low-power mode: 45 W Survival mode: 1 W
Power source	Battery-backed wave energy converter	Battery-backed wave energy converter
WEC size	16 m (30 kW rated power)	3 – 5 m (≈0.88 – 3.4 kW rated power)
Battery capacity	12.6 kWh	2.5 - 35 kWh

may be a competitive choice [Cavagnaro et al., 2020] because the resource is globally abundant [Gunn and Stock-Williams, 2012], has greater energy density than wind or solar energy, and is also most intense at high latitudes [Gunn and Stock-Williams, 2012], where solar energy has significant seasonal limitations. Further, the potential for a smaller surface expression may reduce the incidence rate of vandalism experienced by systems equipped with solar photovoltaics [Teng et al., 2010]. These considerations have motivated the development of "micro-scale" wave energy converters (WECs) [Mundon, 2019].

The technical feasibility of wave-powered ocean observation system was previously demonstrated at the Wave Energy Test Site (WETS) in Kaneohe, HI, as shown in (Figure 3.1). The Wave-Powered Adaptable Monitoring Package (WAMP) included a multibeam sonar, an acoustic camera, two optical cameras with strobe illumination, two hydrophones, real-time control and data processing computer, a wireless charging unit for autonomous underwater vehicles, and an anti-fouling system. Power was provided by a Fred.Olsen Lifesaver WEC, which allowed full operation of the WAMP systems for 84% of its 105 day deployment duration [Joslin et al., 2019] [Polagye et al., 2020]. During this deployment, wave forecasting was not used to optimize energy management, and the system's 84% sensor uptime was, in part, enabled by the availability of a WEC (30 kW rated power output, 16 meter characteristic width) that was "oversized" relative to WAMP power demand (on average, 547 W).

In contrast, our prior work on the economics of wave-powered ocean observation suggests that, at locations with wave power densities similar to WETS (approximately $16\ \mathrm{kWm}^{-1}$ over the WAMP deployment period [DeVisser et al., 2013]) WECs that are roughly an order of magnitude smaller (approximately 2.5 kW, 2.75 m) are cost-optimal to achieve 99% uptime for a constant, 200 W load over a five-year period [Dillon et al., 2022]. This motivates an investigation of whether it may be possible to achieve similar WAMP uptime rates with a much smaller WEC system that utilizes wave forecasts and automatic demand management. In practice, this could be achieved by incorporating a forecast-driven stochastic optimization strategy that can adaptively manage power demand based on predicted resource availability. In this paper, we simulate the performance of a WAMP-like system to evaluate the benefits of this approach.

We emphasize that the objective of our analysis is not to recreate the WAMP in simulation to compare performance under forecast-driven strategies to the system's real-world performance. This decision is due to several factors regarding the WAMP's design and deployment. First, the Lifesaver was not optimized or designed for the WETS wave resource or the WAMP's sensor loads, and was substantially over-sized for the WAMP. Second, the Lifesaver deployment had other priorities in conjunction with powering the WAMP, such as tuning the Lifesaver's control system, collecting performance data, and managing system loads. Not all of the power produced by the Lifesaver or available in the wave resource was allocated to the WAMP, and instantaneous power sent to the WAMP was capped at 960 W by the electrical system design. This cap, which is less than four percent of the Lifesaver's rated power output, mitigated the influence of resource intermittency on the WAMP in comparison to a system that would allocate all of its net generated power to the WAMP or a battery storage system.

Because of this, our approach is to construct an analytical version of an instrumentation package with power demand and flexibility similar to the WAMP, but coupled to smaller WECs that reflect co-design principles for this application. We compare the performance of the analytical model across various decision-making and load flexibility schemas. Aspects of the analytical model used in simulation are compared to the real-world WAMP in Table 3.1, which also contains information about the data used to run our simulations (e.g., location, dates, duration).

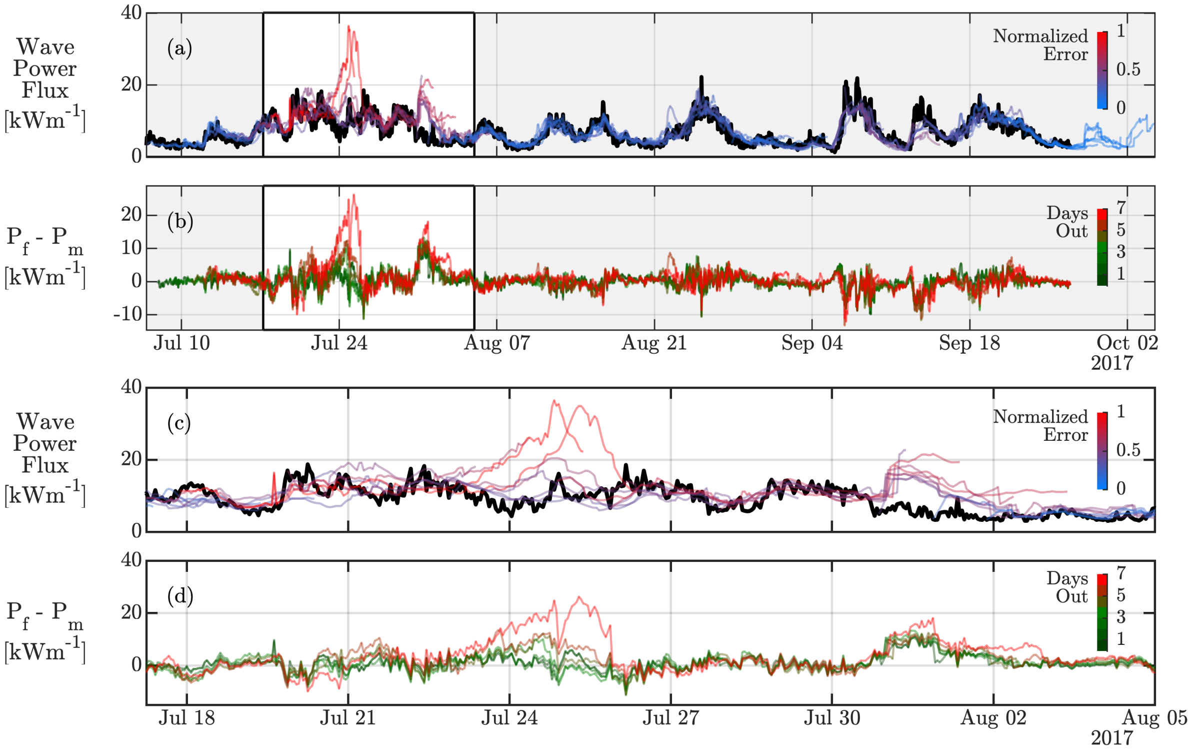

Figure 3.2: The time series data used in this study. (a) The wave power flux compares measured values (thick black line) with many forecasted trajectories (thin blue and red lines) that extend for 180 hours each and update on a daily basis. (b) The displacement between forecasted ($P_{w,f}$) and measured ($P_{w,m}$) wave energy flux over time is categorized by the number of days between the forecasted time and time of forecasting, up to 7 days, and encoded by the colorbar. (c,d) Details of the windowed regions in (a, b) that resolve hourly time scale variations.

3.2.2 Data from WETS

To evaluate the performance of forecast-based decisions, co-located measured and forecasted datasets are required. In this study, measured wave data is from the Coastal Data Information Program (CDIP [McWhorter et al., 2016]) Buoy 225 (Kaneohe Bay, WETS) and forecasted data is from the Pacific Islands Ocean Observing System (PacIOOS) Simulating WAves Nearshore (SWAN [Booij et al., 1997]) Regional Wave Model of O'ahu [Cheung, 2010], queried at the same longitude and latitude of the CDIP buoy. The 82 day duration used to drive the analytical model is the longest period of continuous data availability for both datasets in 2017. While our goal is not to evaluate the suitability of WETS for wave-powered ocean observation, we note that the summer dataset underestimates the annual average wave power density at this site. Each dataset includes statistical quantities describing the sea state (significant wave height, H_s, and peak period, T_p) at

1-hour intervals. When calculating WEC power output over time (Section 3.3.3), we assume that the sea state is constant between these discrete measurements. The forecasted data has a 7 day (180 hour) horizon and is refreshed every 24 hours. Due to a model spin-up artifact that causes initial forecast values to be significantly underestimated, we replace the beginning of the forecast with a linear interpolation between the present sea state and the forecasted sea state 3 hours in the future.

Figure 3.2 displays how forecasted and measured wave energy flux compare over time. Wave energy flux (P, Wm^{-1}) is calculated as

$$P_w = \frac{\rho g^2 {H_s}^2 T_p}{64\pi} \tag{3.1}$$

where ρ is the density of seawater (1025 kgm^{-3}) and g is the gravitational constant (9.81 ms^{-2}). This is the deep water formulation for wave power and is appropriate because water depth is more than twice the wavelength for the near entirety of our simulation window. We note that the deep water wave energy flux should strictly be calculated using the energy period (T_e), but our methodology for WEC generation efficiency (described in Section 3.3.3) also uses T_p to parameterize power production and, therefore, our use of T_p is appropriate.

Over the simulation window, absolute forecast error peaks at $\approx$24 kWm^{-1} above the measured value in late July. In general, wave forecasts over this period are more prone to overestimation than underestimation, particularly for longer-term (> 5 day) forecasts. Shorter term forecasts tend to capture week- and day-long trends, but do not fully resolve hourly fluctuations in the wave resource (Figure 3.2c,d).

3.2.3 Markov Decision Processes

Due to these imperfections between forecasted and actual wave energy resources, a robust method for making optimized decisions on energy management is required. Markov-Decision Processes (MDPs), the chosen class of stochastic optimization for this analysis, are a method for sequential decision-making under uncertainty [Puterman, 2014]. MDPs are interpretable, customizable, and modular, in that optimization penalties are explicitly defined and can be added, removed or modified for application-based purposes. Additionally, MDPs are computationally tractable in real time and under limited power availability. These characteristics, particularly that MDPs are a framework for *sequential* decision-making, make MDP methodology an effective starting point for optimizing the energy management of our system on a rolling basis. Additionally, due to the novelty of using forecasts to optimize stand-alone energy systems, the interpretable and customizable aspects of MDPs are useful in creating transparency around the effects of our methodology. This being said, as discussed in Section 3.5.2, future optimization efforts building upon our findings may benefit from utilizing more advanced, less interpretable data-driven methods, such as reinforcement learning [Sutton et al., 1992].

MDPs are broadly used, spanning applications in finance, healthcare, game theory and robotics [White, 1993] [Kolobov, 2012] [Bennett and Hauser, 2013]. Previous applications to marine energy include maintenance scheduling for ocean wave farms [Pradhan et al., 2018] and tidal energy infrastructure [de Nie et al., 2019], as well as determining certainty in the long-term generation capacities of wave energy farms [Arzaghi et al., 2020]. To our knowledge, this is the first application of MDPs to the real-time energy management of a marine energy system.

3.3 Methods

The following methodology was developed and implemented in MATLAB (Mathworks, R2020a). For greater detail and re-use, our code is open source, available at https://github.com/tmaxdillon/WAMP-MDP.

At a high level, in this application, battery state of charge over time depends on the balance between inflow of energy from WEC generation and outflow of energy from ocean sensing loads. Because we have operational control of these sensing loads, a decision needs to be made at the present time about how much power to consume. Here, we employ our MDP to estimate the optimal decision based on forecasted wave generation over a finite horizon, and evaluate the aggregate performance of these decisions through forward-stepping simulations. We begin by describing the form of the MDP objective function and its computation, and then describe the specifics of the energy system modeling. Last, we present our evaluation strategy, which compares the effectiveness of MDP to other approaches, such as inflexible loads and decision making without forecast data.

The following terms are used with specific meaning throughout the remainder of the paper:

- **Analytical Model**: Our analytical recreation of the WAMP (including its WEC, battery bank and instrumentation package), described in Table 3.1.

- **Backward Recursion**: How the MDP algorithm is solved, resulting in an estimated optimal power consumption decision for the analytical model.
- **Forward Simulation**: Evaluating the various decision approaches by simulating the analytical model forward in time for two months of sequential decisions.

3.3.1 MDP Objective Function

The objective function of an MDP is often referred to as Bellman's equation [Bellman and Kalaba, 1957]. Our Bellman's equation is a finite-horizon, discrete-time, backward recursion MDP. We selected a finite-horizon and discrete-time approach (as opposed to infinite-horizon or continuous-time) because this matches the temporal characteristics of wave forecasts, which are limited in their extent and discretized hourly. Specifically, this temporal discretization results in forecast "stages", t, at an interval of one hour up to the forecast's horizon, T, where $157 \leq T \leq 180$ hours, depending on how recently the current wave forecast was updated. To make decisions based on forecast time series, a backward recursion approach is common in MDP applications because it reduces the algorithm into a series of manageable subproblems.

Our Bellman's equation is defined by S, A, $\mu(a_t)$, and $\theta(a_t, t)$ where S is a set of states $s \in S$ that define the analytical model at each stage, A is a set of available actions $a \in A$ (or, "decisions") that transition the analytical model between states $s \in S$, and $\mu(a_t)$ and $\theta(a_t, t)$ are functional penalties imposed by making action a at stage t. The functional penalties are designed to incentivize application-specific outcomes.

For our wave-powered ocean observation application, we define state, action and these penalties as follows. States $s \in S$ represent the state of charge of the battery bank, discretized by d_s = 20 Wh (as discussed in Appendix B.1) and bounded between 0 kWh and the storage capacity of the battery bank, E_m ($2.5 \leq E_m \leq 35$ kWh). We handle rounding to state discretization values by tracking the true, non-discretized state time series. If the state of charge is less than the non-discretized value, our algorithm rounds up to the nearest discretization value, and rounds down if the state of charge is larger than the non-discretized value. Actions $a \in A$ are the set of operational sensing modes the analytical model can choose between, which enables load flexibility and therefore affects transitions between states over time (i.e., the battery bank's state of charge profile). We employ four operational modes with varying power consumption levels to demonstrate the suitability of our algorithm for a generic ocean observation system. Regarding the functional penalties, $\mu(a_t)$ incentivizes instantaneous power consumption and $\theta(a_t, t)$ incentivizes long-term consistency. Both are a function of a_t, which is the action or operational mode being evaluated at stage t.

The $\mu(a_t)$ penalty punishes the algorithm for entering operational modes with lower power consumption, thus incentivizing power consumption for ocean observation. Penalty values for each operational mode are provided in Table 3.2. These values are subjective, deliberately increasing with decreasing power consumption.

Table 3.2: Operational modes ($a \in A$)

Name	**Load** ($L(a_t)$)	**Penalty** ($\mu(a_t)$)
Survival Mode	1 W	1
Low Power	45 W	0.8
Medium Power	450 W	0.2
Full Power	600 W	0

The $\theta(a_t, t)$ penalty punishes the algorithm for failing to operate in either its medium- or full-power mode at a repeated interval throughout the simulation, specified as every θ_h hours. If the stage t coincides with θ_h and the instrumentation package is not in medium- or full-power mode, $\theta(a_t, t) = \theta_A$. Otherwise, if the instrumentation package is either in medium- or full-power mode or if the stage t does not coincide with θ_h, $\theta(a_t, t) = 0$. Mathematically this can be expressed as

$$\theta(a_t, t) = \begin{cases} \theta_A, & \text{if } a_t = \{1, 2\} \text{ and } h(t) \bmod \theta_h = 0 \\ 0, & \text{if } a_t = \{3, 4\} \text{ or } h(t) \bmod \theta_h \neq 0 \end{cases} \tag{3.2}$$

where $h(t)$ is the hour of the day at stage t. We delineate between a = 2 (low power) and a = 3 (medium power) as the threshold for the application of θ_A because this step is the largest change in power consumption in our operational modes. By default, θ_h = 4 hours and θ_A = 1000, meaning the $\theta(a_t, t)$ penalty magnitude is three orders of magnitude larger than the maximum value of $\mu(a_t)$ and that it is assessed on four hour intervals. Like the $\mu(a_t)$ penalty, these values are subjective and tuned to demonstrate the utility of an MDP algorithm in this application.

We emphasize that this subjectivity is an advantage of the MDP framework, as it allows an end-user to design the MDP for specific sensing objectives. Similarly, an end user can add subjective and/or application-specific penalties, such as penalizing the algorithm for operating at low battery levels or penalizing for fluctuating between operational modes. Here, to increase the interpretability of our outputs, we chose to only incorporate two functional penalties.

Our Bellman's equation is, therefore,

$$J_t(s_t) = \min_{a_t \in A} \left[\mu(a_t) + \theta(a_t, t) + J_{t+1}(s_{t+1}) \right] \tag{3.3}$$

where s_t is battery state of charge at stage t, J_t is the objective function value at the current stage t, and J_{t+1} is the objective function value of the future stage as a function of state transition to s_{t+1}.

3.3.2 Backward Recursion

Our Bellman's equation is computed through a backward recursion approach to reduce its computation to a series of manageable subproblems. Backward recursion initiates Bellman's equation at stage $t = T - 1$, assuming J_T = 0, and solves for the objective function value J_{T-1} for each possible state $s \in S$. This identifies the action for all states $s \in S$ that minimize the objective function at J_{T-1}. The objective function value for each state $J_{T-1}(s_{T-1} \in S)$ is stored, enabling the next recursion, which is a step backward in time, J_{T-2}, to compute Bellman's equation with known J_{T-1} values, based on how state s_{T-2} transitions to s_{T-1} under all actions $a \in A$ evaluated by the objective function. The recursion repeats this process, stepping backward in time one stage at a time. When the stage representing the present moment in time ($t = 0$) is reached, all future information is contained within J_1, such that action a_0 is the "optimal" decision recommended through backward recursion, based on the analytical model's present battery state of charge s_0. This procedure is illustrated in Figure 3.3.

Often, Bellman's equations will include "transition probabilities", which define the probability that the system will transition from s_t to other states $s \in S$ if action a_t is chosen. This enables state transitions and their optimization values to account for many potential outcomes with relative uncertainties. In our application, we chose to disregard transition probabilities (i.e., assume that state transitions are 100% certain) because these probabilities would depend on wave forecast errors, which are continuously distributed and

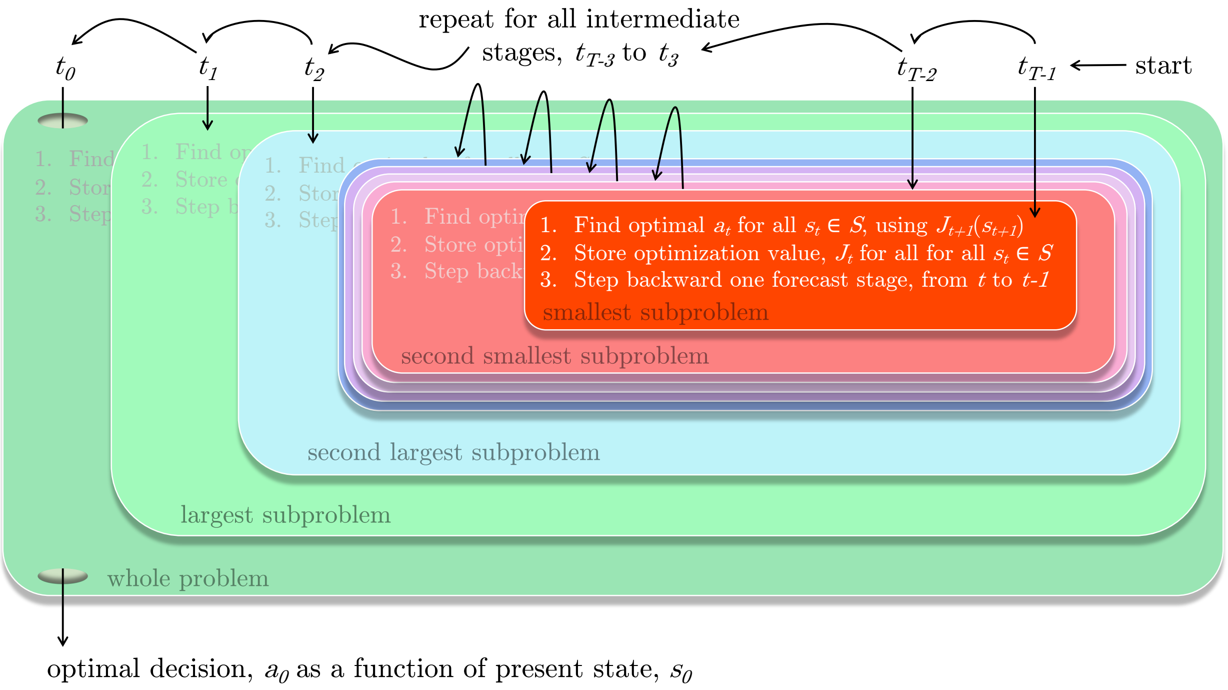

Figure 3.3: A schematic flowchart of a finite horizon, discrete time, backward recursion MDP. As shown, backward recursion reduces stochastic optimization into a series of manageable subproblems by finding the optimal action a for all stages $s \in S$, beginning at the transition from stage T_{t-1} to t_T. The primary output of backward recursion is the optimal decision at the present time, a_o.

vary in time. We find that our algorithm is effective without transition probabilities due to the stability inherent to the state space $s \in S$. This stability is due to (1) constraints on the state space (i.e., the battery's state of charge is physically bounded between zero and E_m) and (2) the fine temporal discretization of decisions relative to the large size of the state space (i.e., each decision only lasts for one hour, producing changes in state space that are most often an order of magnitude smaller than the size of the state space itself). If our state space was not physically-bounded, or if individual decisions could move the analytical model into a drastically different position within the state space much more frequently, transition probabilities might be needed for algorithm stability. Removing transition probabilities has the added benefit of reducing the number of algorithm evaluations needed to find an optimal decision, from $(T\text{-}1)|A||S|^2$ to $(T\text{-}1)|A||S|$, which is computationally significant for the required battery discretization and forecast horizon.

Rather than using statistical transition probabilities to estimate state transitions from s_t to s_{t+1}, we developed an energy model to estimate those transitions within our analytical model. This energy model is described in the following section.

3.3.3 Energy Modeling

To evaluate the analytical model's energy system response over time to actions taken in backward recursion (a_t) and forward simulation (a_0), we model the temporal variability in wave-generated energy and ocean observation loads. Energy transfer between the WEC, battery bank, and instrumentation platform are discretized in the time domain as

$$E_{t+1} = E_t + (P_t - L(a_t))\Delta t - D_t - \Gamma(E_t) \tag{3.4}$$

where the t and $t+1$ subscripts denote the current and next time step (both between stages of backward recursion and simulated time steps), Δt is time step interval (1 hour for both backward recursion stages and simulation time steps), E is battery state of charge (rounded to a discretization value $s \in S$), P_t is WEC power output, $L(a_t)$ is power consumed by the instrumentation platform as a function of action (i.e., operational mode), D_t is energy discarded, and $\Gamma(E_t)$ is self-discharge of the battery as a function of battery state of charge. We constrain E_{t+1} to the maximum battery storage capacity (E_m) and discard any generation in excess of the present load and storage capacity through a resistive load (represented by D_t). We allow E_{t+1}

to drop no lower than 0 kWh. The simulation is initialized with the battery at 50 % state of charge. If there is insufficient power available (P_t or E_t) for an action a_t chosen for a given time step (during backward recursion or forward simulation) a_t is adjusted to the operational mode with the largest amount of consumption possible that still maintains a non-negative battery state of charge, and E_{t+1} is set to the energy remaining following this decision. Regarding the nomenclature of "backward recursion" and "forward simulation", we clarify that the energy transfer described in Equation 3.4 is always evaluated in a forward-stepping manner.

As discussed in Section 2.3.1, we base our battery bank characteristics around lithium iron phosphate (LFP) batteries because, in this application, they are low-cost, exhibit low self-discharge (3% loss per month), have long service life, and are safer in thermal runaway [Feng et al., 2018] relative to other lithium-ion chemistries. In addition, LFP batteries can be fully discharged. In our prior work, we found that battery degradation (i.e., the loss of storage capacity over time or "capacity fading") [Birkl et al., 2017] is not likely to drive service intervals for this application and, therefore, factor into energy storage system sizing, due to relatively large storage-to-generation ratios (in other words, relatively slow battery cycling). Additionally, the amount of capacity fading that would occur during the two month simulation window is negligible. We, therefore, disregard the influence of degradation in Equation 3.4.

WEC System Modeling

To approximate the power generation of an ocean observation-scale WEC, we geometrically-scaled the U.S. Department of Energy Reference Model 3 (RM3) WEC [Neary et al., 2014] and evaluated its performance in WEC-Sim, an open source computational tool for WEC simulation [Lawson et al., 2014]. The RM3 WEC (Figure 3.4) is a full-scale floating point absorber with a 20 meter diameter float and 286 kW peak power output, which considerably exceeds the generation capacity required for our application.

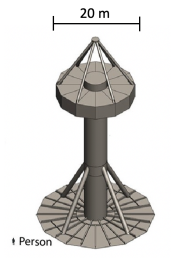

Figure 3.4: Reference Model 3 (RM3) floating point absorber WEC. Source: Sandia National Laboratories.

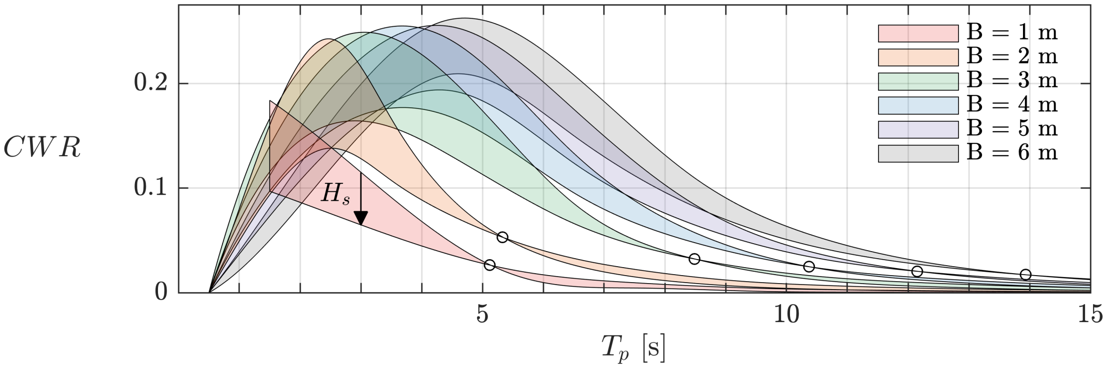

Figure 3.5: RM3 performance (CWR) as a function of T_p (x-axis), H_s (arrow, indicating upper and lower bounds) and B (color). At low T_p, CWR decreases with increasing H_s. At higher T_p (beyond inflection points denoted by ○) CWR increases with increasing H_s. CWR at discrete T_p are shown as smooth contours for ease of interpretation.

Therefore, we rescaled the RM3 WEC to characteristic diameters (B) of 1, 2, 3, 4, 5 and 6 meters, and analyzed these in WEC-Sim over the range of sea states in wave measurements and forecasts at WETS (i.e., significant wave heights, H_s, and peak wave periods, T_p). For each sea state, the damping coefficient for the power take-off (a WEC-Sim input) that resulted in the most power generated was chosen from a set of five values (Appendix B.2), approximating a passive optimal control strategy (i.e., no active tuning of the WEC dynamic response). While these scaled versions of the RM3 WEC are not necessarily optimized for hydrodynamic performance (e.g., a different aspect ratio might be optimal as absolute size decreases), this approach captures variations in hydrodynamic performance due to changes in WEC scale for a given sea state, which is needed to assess the influence of WEC size on MDP performance.

Figure 3.5 presents the WEC-Sim results and, therefore, performance of WECs considered in this study. These results are parameterized by the capture width ratio (CWR), a measure of hydrodynamic efficiency defined as the mechanical power generated by the WEC divided by the incident wave power (Equation 3.1). Peak CWR and resonant period increase with B, and CWR has a trivariate dependence on T_p, H_s and B. These results are linearly interpolated at unique combinations of T_p, H_s, and B to calculate CWR as a function of sea state and characteristic diameter.

P is calculated as the product of cumulative efficiencies, WEC diameter and the wave energy flux

$$P = \eta * CWR * B * P_w - \sigma G_r \tag{3.5}$$

where η is electrical conversion efficiency (assumed to be 0.6), P_w is wave energy flux, σ is the percentage of the WEC's rated generation used to power "house loads" (assumed to be 10$\%$), and G_r is the rated generation of the WEC in W for dimensional consistency. Regardless of the power available in a given sea state, WEC generation is capped at G_r. With exception to the parasitics of a house load, this formulation is identical to the International Electrotechnical Commission technical specification for wave energy calculation [Commission, 2012].

G_r is calculated from Eq. 3.5 by assuming the WEC must be large enough to produce its rated power ($P = G_r$) when H_s = 2.5 meters and T_p = 10 s. This rated condition was found by conducting a sensitivity analysis across rated H_s and T_p and selecting the rated sea state that produced the largest cumulative WEC power output throughout the simulation window. This yields capacity factors (defined as the mean electrical power output divided by G_r) between 45$\%$ and 51$\%$ across our simulations.

3.3.4 Forward Simulations

We evaluate the performance of our MDP by simulating the analytical model forward over a two month window (Figure 3.2). At each time step in this forward simulation, a decision on which operational mode to enter (a_0) is made and Equations 3.4 and 3.5 are used to advance the analytical model to the next time step using measured wave data. As mentioned in Section 3.2.2, SWAN data is used for backward recursion, forecast-based decisions, and measured CDIP data is used to advance the forward simulation. This process is represented schematically in Figure 3.6.

To investigate the influence of energy system size (i.e., WEC characteristic diameter B and maximum storage capacity E_m) on ocean sensing performance, we evaluate the MDP across combinations of B = 3, 4 and 5 meters and E_m = 2.5, 5, 10, 15, 20, 25, 30 and 35 kWh. For all combinations of energy system size, we conduct the forward simulation under eight decision-making and load management schemas to contextualize the performance of our MDP. This results in 192 forward simulations (3 x 8 x 8) with distinct outcomes.

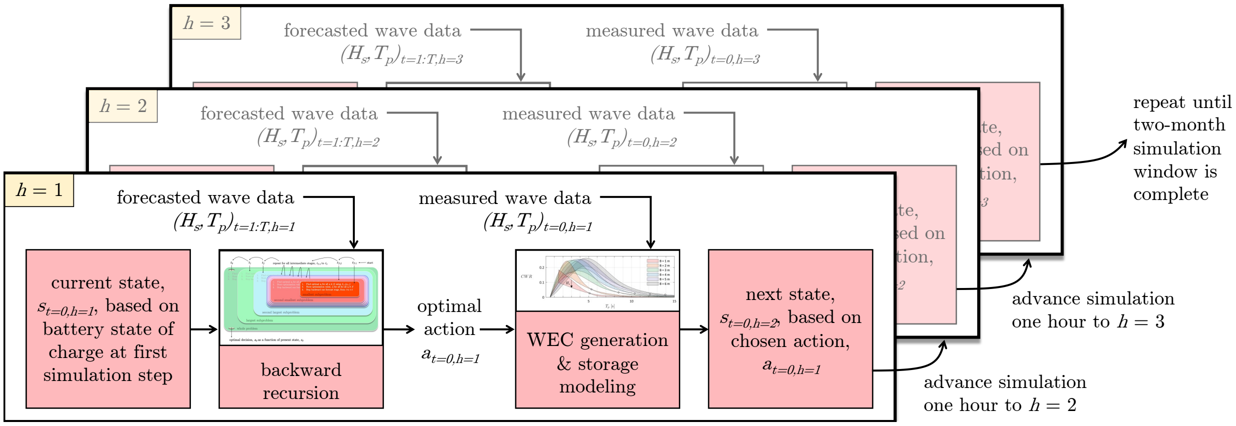

Figure 3.6: Our MDP forward simulation procedure, where t denotes the stages of backward recursion and h denotes each forward simulation step, amounting to a two-month simulation window.

Decision-Making Schemas

We compare the backward recursion MDP described in Section 3.3.1 to other decision-making schemas: “Posterior Bound”, “Greedy”, and “Duration-Based” decision-making.

The Posterior Bound decision-making schema is “omniscient”, representing the MDP’s solution when all forecasted variables (H_s and T_p) are known (i.e., zero forecast error). This is achieved by replacing the forecasted SWAN dataset with the measured CDIP dataset during backward recursion. We note that while this produces the optimal outcome of the MDP, this may not be considered the optimal performance of our analytical model because the MDP utilizes subjective penalties. We emphasize that the Posterior Bound decision-making schema cannot be achieved in an actual deployment and is only possible *a posteriori*. Nonetheless, it is a useful schema to understand the influence of forecast uncertainty in decision making.

The Greedy and Duration-Based decision-making schemas do not utilize forecasting and represent less sophisticated methods of demand management. The Greedy schema attempts to consume generated energy immediately, maximizing cumulative sensing, while the Duration-Based schema attempts to prioritize longer-term consistency. In the Greedy decision schema, at each time step, the instrumentation package enters the operational mode with the largest power consumption possible, based on the balance of energy flows in Equation 3.4. In the Duration-Based decision schema, the instrumentation package operates identically to the Greedy schema at every θ_h interval, consuming as much power as is possible. This reflects the persistence incentive produced through the $\theta_h(a_t, t)$ penalty in the MDP. When operating outside of every

θ_h interval, Duration-Based decisions are based on the amount of time the instrumentation package could continuously operate in its medium-power mode (450 W) under the present level of WEC generation before fully depleting its battery bank. If the WEC is producing more power than instrumentation is consuming, full-power mode is entered. If the instrumentation package is in a net consumptive state, but could operate for at least 12 hours before depletion, medium-power mode is entered. If the instrumentation package could only operate for three hours before depletion, low-power mode is entered. Finally, if the instrumentation package could operate for less than three hours before depletion, survival mode is entered. Like the MDP penalties ($\mu(a_t)$ and $\theta(a_t, t)$), the values governing decision-making in the Duration-Based schema are subjective and were determined through ad-hoc iteration.

These schemas represent load management strategies that may occur if wave forecasting is not available, serving as a useful comparison for the MDP. We extend this comparison by adding two cases with inflexible loads: “Maximum Power, No Flexibility” (MPNF) and “Average Power, Fixed Load” (APFL). In these cases, performance is determined solely by power system size. In MPNF, we compute the maximum 100% continuous load possible over the two-month simulation window given B and E_m. In APFL, we compute the mean load over the simulation window if a system of size B and E_m were to simply switch off when there is insufficient power. We analyze APFL using both the full (600 W) and medium (450 W) power operational modes as the "on" state, thus creating two outputs, denoted by APFL600 and APFL450.

Performance Metrics

We present five performance metrics—mean power consumption, “theta rate”, mean duration in low/survival mode, maximum duration in low/survival mode, and battery degradation—which compare characteristics of the decision-making schemas and inflexible cases.

Mean power serves as a proxy for how much sensing was accomplished over the simulation window and is computed as the mean value of the load time series, (L). Theta rate is the percentage of θ_h intervals in which the instrumentation package successfully operated in its full- or medium-power mode. We note that these θ_h intervals are explicitly accounted for in decision making by the MDP, Posterior Bound and Duration-Based schemas, but not the Greedy schema. The mean and maximum durations, respectively, define the mean and longest duration in the simulation window with operations at low and survival modes (or, equivalently, operations below full- or medium-power mode).

Last, battery degradation represents the amount of capacity fading that would occur if the state of charge profiles for this two-month horizon were extended to a 5-year period. In other words, while degradation does not affect the energy system model over the simulation time scale, it could become relevant over longer horizons. As described in Section 2.3.2, we compute battery degradation using an adapted version of Xu et al.'s [Xu et al., 2016] empirically-derived stress models for capacity fading of lithium ion batteries under irregular cycling, which take state of charge profile and temperature (assumed to be 25 °C) as inputs.

We note that battery degradation is not accounted for in the decision-making priorities of our proposed load management schemes and is, therefore, a diagnostic evaluation metric rather than a measure of algorithm performance. Other metrics, such as longest duration in low or survival mode and, in the case of the Greedy algorithm, theta rate, are similar in that they are not explicitly considered in the decision criteria.

3.3.5 Computation

We conduct our simulations using a single node of the National Renewable Energy Laboratory's High Performance Computing System, where each combination of B and E_m is allocated to a different core and run in parallel. In this arrangement, a single forward simulation involving backward recursion takes approximately 2 hours and 30 minutes of clock time to complete. We discuss the implications of this and the feasibility of using this algorithm for real-time decision-making in Section 3.5.2.

3.4 Results

We begin by presenting time series diagnostic outputs for a single forward simulation in Figure 3.7. This simulation involves a three meter WEC and 10 kWh battery bank and uses MDP to make decisions about which operational mode to enter at hourly time steps. We find that the instrumentation package is able to operate continuously in its full-power mode when significant wave height is large for extended periods of time and WEC power outputs are close to the rated power limit of 0.88 kW (c. July 20$^{\mathrm{th}}$). When significant wave height declines and peak wave period increases, wave flux and capture width ratio decline, decreasing WEC power output to near-zero and forcing the instrumentation package to depend on battery storage reserves. This results in operating mostly low- and medium-power modes (c. September 7$^{\mathrm{th}}$). While these

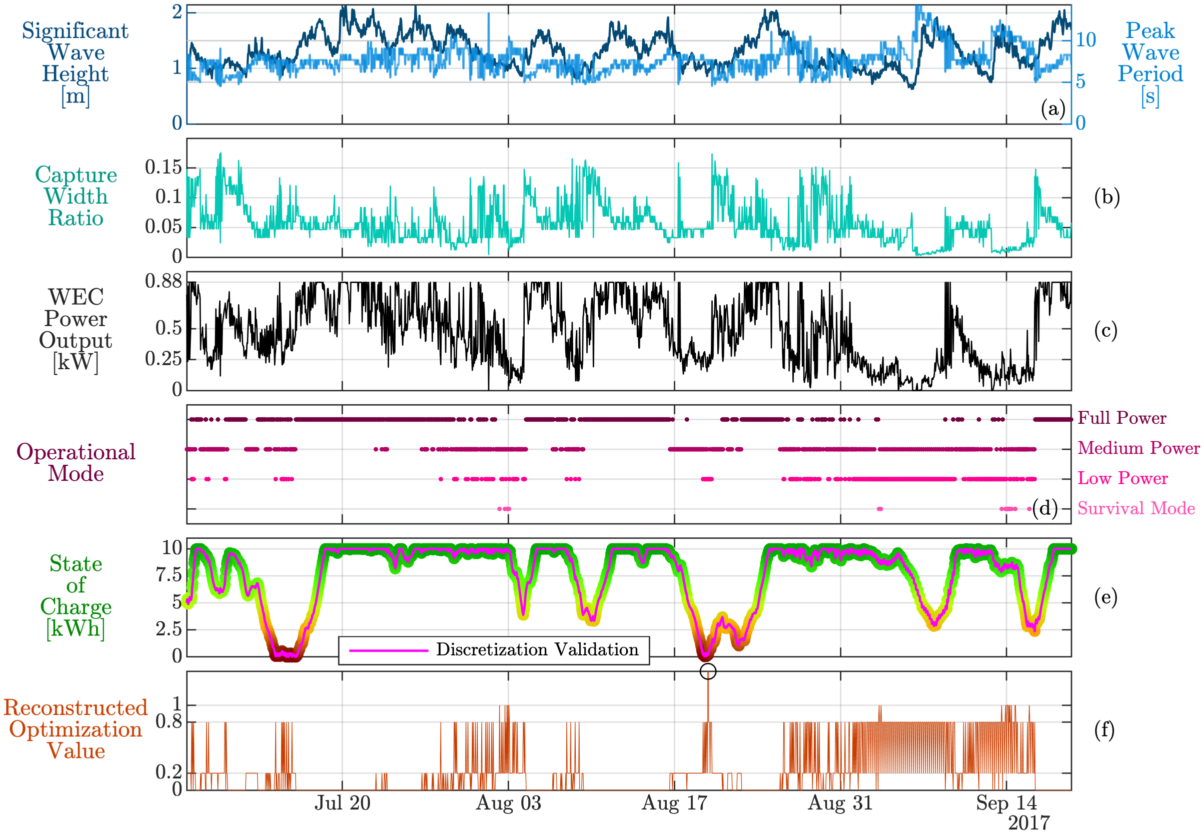

Figure 3.7: Time series diagnostics of a forward simulation (3 meter WEC, 10 kWh battery bank) under MDP decision-making, including (a) sea state, (b) capture width ratio, (c) WEC power output, (d) operational mode, (e) battery state of charge and discretization validation, and (f) reconstructed optimization value over the two month simulation window. The reconstructed optimization value is our objective function value without the backward recursion penalty (J_{t+1}) and is, therefore, equal to $\mu(a_t)+\theta(a_t,t)$. To show variations driven by the $\mu(a_t)$ penalty, the y-axis in (f) is truncated, as the $\theta(a_t,t)$ penalty's θ_A term has a value of 1000 that would otherwise mask variations in $\mu(a_t)$. The open circle marks where the reconstructed optimization value exceeds the truncated axis limit, indicating that at this time step the MDP failed to meet the $\theta(a_t,t)$ schedule.

diagnostics only show instantaneous (i.e., non-forecasted) variables, we note that the operational modes are being selected by interpreting wave forecast data through backward recursion, as described throughout Section 3.3. The reconstructed optimization value shows the instantaneous penalty value (i.e., Equation 3.3 without J_{t+1}) of these decisions over time.

In Figure 3.8, we present time series diagnostics that compare performance for additional decision schemas, including the Posterior Bound, Greedy decision-making and Duration-Based decision-making. These results are for the same WEC and battery size shown in Figure 3.7 (time series comparisons of additional WEC and battery sizes are provided in Appendix B.3), and therefore, the MDP results are identical between these figures. We find that, in general, the Greedy and Duration-Based decision-making schemas cause the instrumentation package to operate at lower battery state of charge levels, with the Greedy algorithm, as expected, depleting battery reserves most aggressively. In contrast, the decision-making schemas that utilize forecasting (MDP and Posterior Bound) tend to operate with higher battery levels, strategically saving energy to meet longer-term sensing objectives. All discrepancies between the MDP and Posterior Bound are due to errors in forecasted data. Two overall performance metrics, mean power consumption (P_{mean}) and theta rate (θ_{rate}) are provided as insets in Figure 3.8. While there are differences between the decision-making schemas, this only describes performance for one combination of WEC and battery size (four forward simulations).

Figure 3.9 provides a more comprehensive comparison, displaying the performance of all combinations of WEC and battery size under MDP, Posterior Bound, Greedy and Duration-Based decision-making (96 forward simulations). In general and as expected, most performance metrics (with exception to battery degradation, which, as described in Section 3.3.4, is not explicitly factored into decision criteria) improve with increasing WEC and battery size. We find that it is possible to keep the instrumentation package in its full-power mode for the entire simulation window with a five meter WEC and a battery bank with at least 25 kWh storage capacity. When this is the case, the Duration Based Logic is unable to remain in full power for the entire window because, by definition, this logic enters medium power whenever WEC power output drops beneath 450 W, independent of battery storage.

The Posterior Bound, which is the outcome of the MDP when there is no error in the wave forecast, performs most favorably among decision-making schemas, featuring high power consumption by ocean

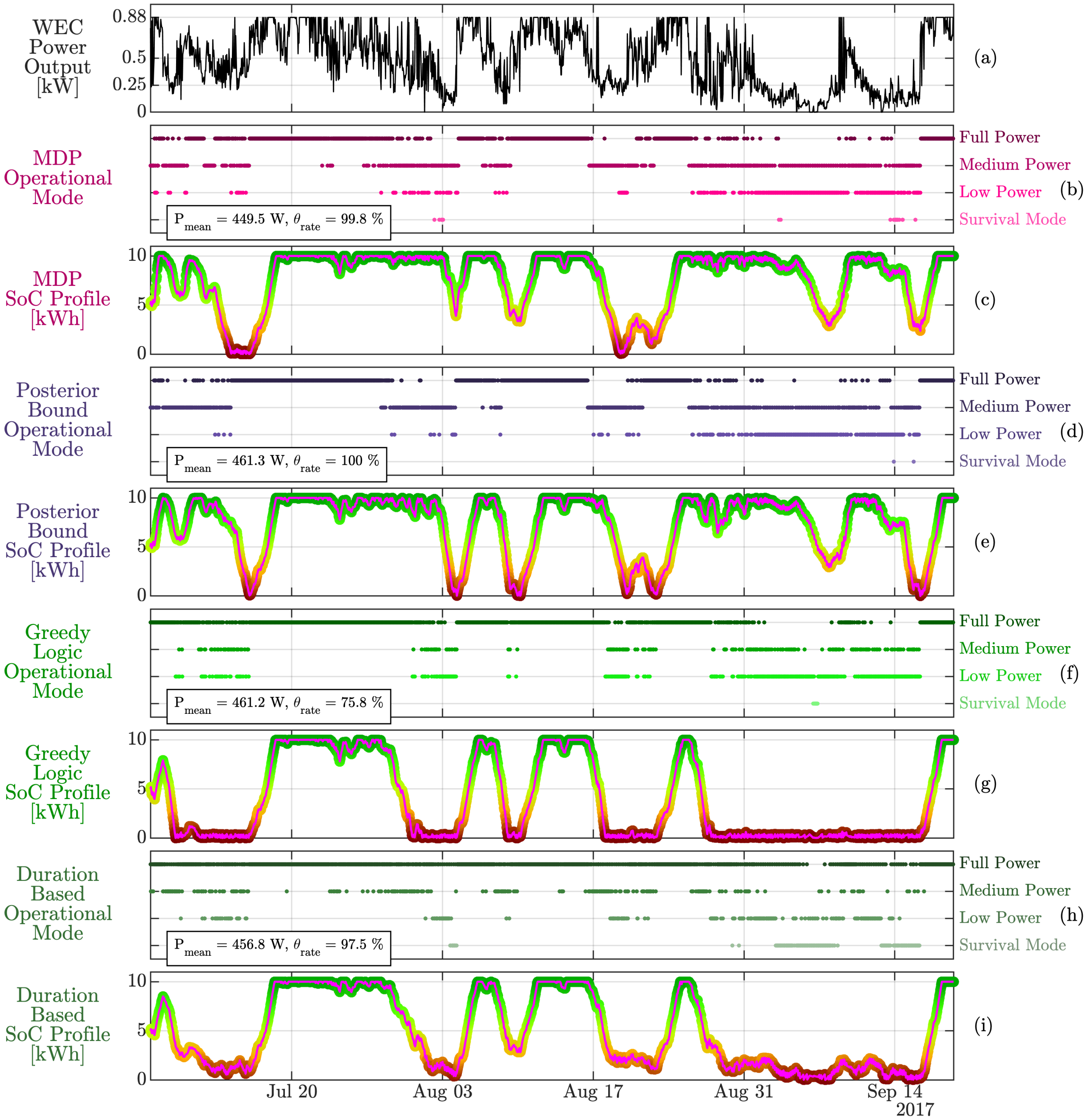

Figure 3.8: Time series, over the entire simulation window, of (a) WEC power output, operational mode, and battery state of charge of forward simulations under (b, c) MDP, (d, e) Posterior Bound, (f, g) Greedy, and (h, i) Duration-Based decision-making. Annotations show two performance metric values: mean power consumption (P_{mean}) and theta rate (θ_{rate}) for each decision schema. The pink lines (c, e, g, i) show the discretization validation discussed in Appendix B.1.

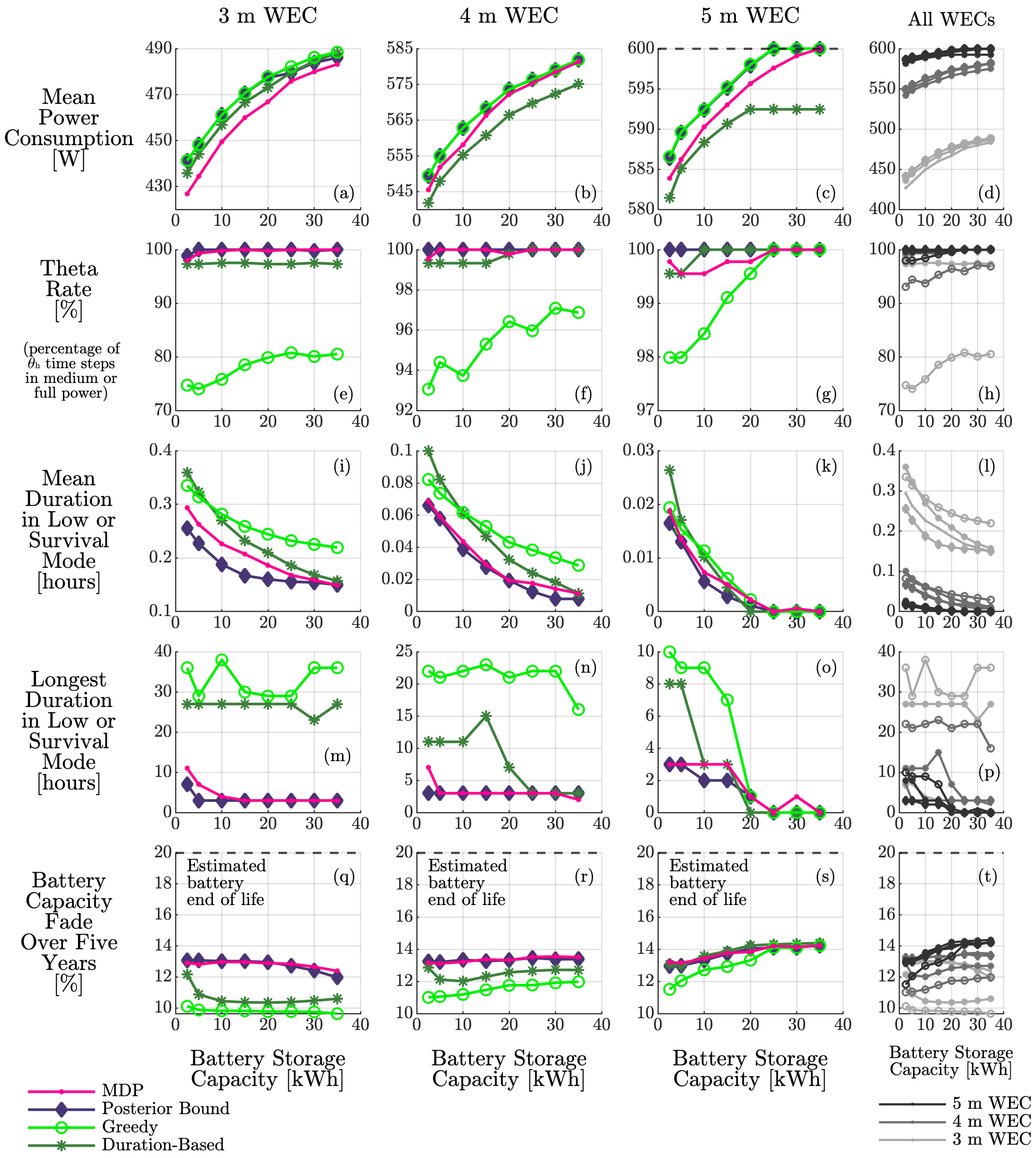

Figure 3.9: Performance metrics for forward simulations under MDP, Posterior Bound, Greedy, and Duration-Based decision-making across all combinations of WEC and battery size. Metrics include (a-d) mean power consumption, (e-h) theta rate, (i-l) mean and (m-p) longest duration in low or survival mode, and (q-t) battery capacity fade relative to the battery's end of life. To show detailed comparisons, we separate these results by WEC size, resulting in unique y-axis scales for each subplot. The far right column combines these results to contrast performance metrics across WEC sizes. In each plot, the x-axis is battery storage capacity.

sensing and, in general, the least amount of sensing intermittency. The Greedy decision-making schema parallels the Posterior Bound in terms of cumulative power consumption, but causes the instrumentation package to experience longer durations in low and survival mode, and a lower percentage of θ_h time steps in medium- or full-power mode, as these priorities are not factored in the Greedy algorithm. We find that battery capacity fade over a five year period is well below the predicted amount of capacity fading that may occur before the battery's end of life (20%) in all forward simulations.

Finally, Figure 3.10 compares the performance metrics for the MDP to the inflexible load cases: Maximum Power, No Flexibility (MPNF) and Average Power, Fixed Load, where the fixed setting is medium-power mode (APFL450) or full-power mode (APFL600), as described in Section 3.3.4. These results are for all combinations of WEC and battery size (96 forward simulations). The MDP performs most favorably, featuring the highest power consumption for ocean sensing and relatively low intermittency. We note that, because the MPNF load management case calculates the largest possible *continuous* power consumption for each WEC and battery size, by definition it has a theta rate of 100% (i.e., no time steps in a reduced or fully powered-off mode). However, this inflexibility causes the instrumentation package to consume far less power, on average, until the WEC size and storage capacity are sufficient to allow continuous, high-power operation. In general, these approaches have larger ranges of performance metric values than those shown in Figure 3.9, indicating that the performance of the inflexible load cases are more dependent on WEC and battery size than decision-making schemas that incorporate load flexibility.

3.5 Discussion

Here, we interpret our results, presenting insights into the development of forecast-based strategies for optimizing the power management of stand-alone renewable energy systems. Our results compare various approaches to managing the power consumption of an autonomous, WEC-powered ocean observation system. We find that the effectiveness of these approaches depends on the priorities for the sensing application. In discussing our results, we make use of two terms that describe application characteristics:

- **Load Flexibility**: Load flexibility refers to an application's ability to enter operational modes with different levels of power consumption. Complete flexibility indicates a platform that can consume any discrete power draw up to its maximum consumption, whereas complete inflexibility indicates a

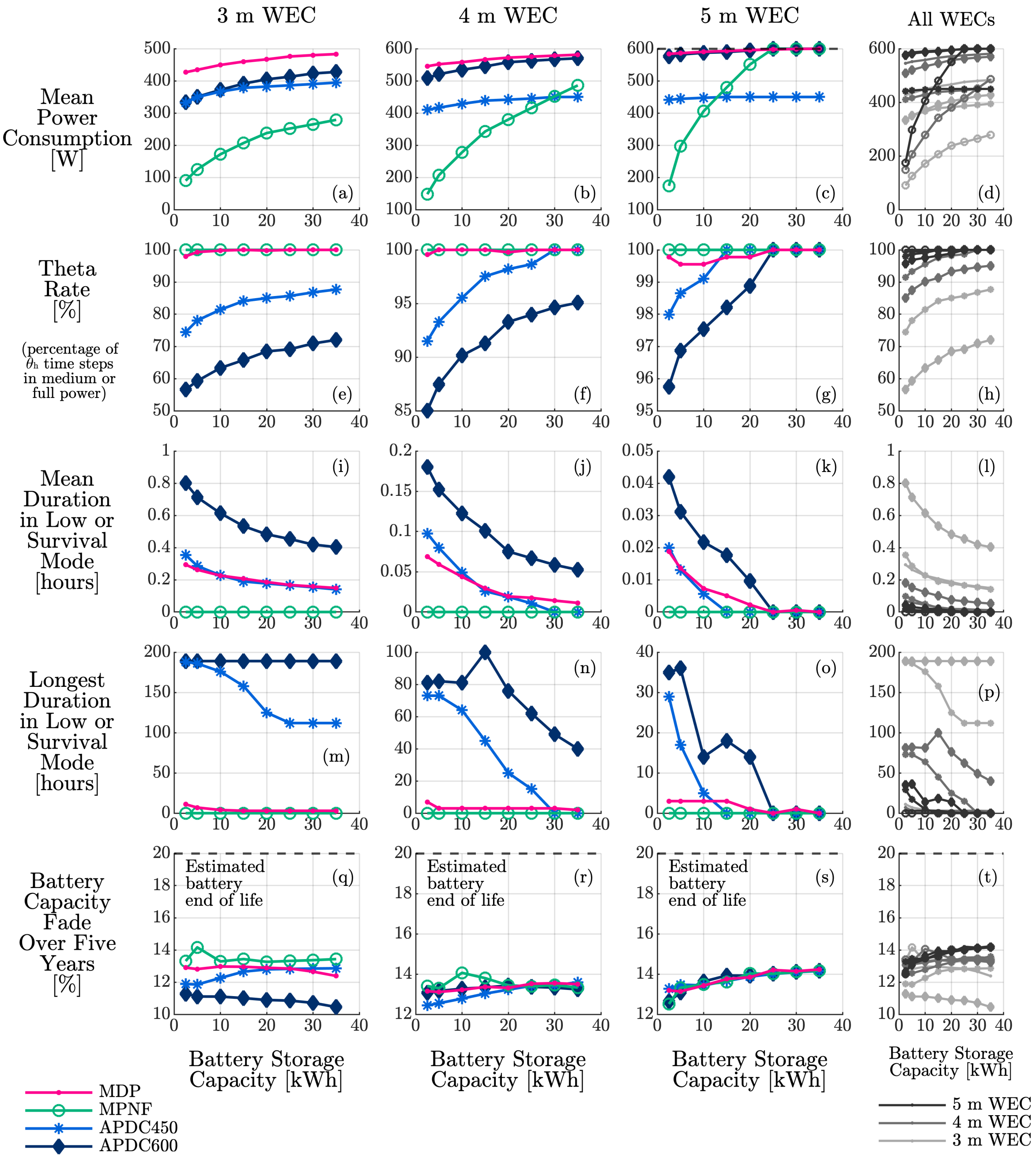

Figure 3.10: Performance metrics of forward simulations under MDP, MPNF, APFL450, and APFL600 load management schemes, across all combinations of WEC and battery size. Metrics include (a-d) mean power consumption, (e-h) theta rate, (i-l) mean and (m-p) longest duration in low or survival mode, and (q-t) battery capacity fade relative to the battery's end of life. To show detailed comparisons, we separate these results by WEC size, resulting in unique y-axis scales for each subplot. The far right column combines these results to contrast performance metrics across WEC sizes. In each plot, the x-axis is battery storage capacity.

platform that can only operate at one consumption level.

- **Load Deferrabilty**: Load deferrability refers to an application's ability to defer the timing of loads. For example, a load that is completely deferrable means that the timing of when that load is met is unimportant to the application. In contrast, other loads, may have to be met on or within a defined schedule (e.g., resident AUV recharge).

Our application is an ocean observation system with considerable load flexibility (i.e., four distinct power consumption levels, Figures 3.7 and 3.8). We find that, under our performance criteria, the use of forecasting to manage this flexibility is most beneficial when loads are prioritized on some defined schedule and, therefore, are not completely deferrable.

When this is the case, it is *possible* to manage power effectively without forecasting, demonstrated by the performance of the Duration-Based algorithm, but we find that the use of forecast information enhances performance in nearly all cases. Specifically, our MDP has shorter durations in low and survival mode (Figure 3.9i-p), and, in most cases, higher theta rates (Figure 3.9e-h) and mean power consumption (Figure 3.9a-d), indicating that it is more effective at meeting scheduled loads and providing cumulative sensing than the Duration-Based algorithm.

On the other hand, if the loads are completely deferrable, forecast information is less impactful. For completely deferrable loads, the theta rate (Figure 3.9e-h), as well as mean (Figure 3.9i-l) and longest (Figure 3.9m-p) duration in low or survival mode have no importance. Consequently, the only relevant metric is mean power consumption (Figure 3.9a-d), where we the Greedy algorithm outperforms the MDP. As mentioned previously, battery capacity fade (Figure 3.9q-t) is considered a diagnostic evaluation, rather than a performance metric, as it is not factored into any of the decision criteria and is not estimated to reach the 20% failure limit over a five year period.

By definition, the optimal strategy for completely deferrable loads is to consume power as immediately as it becomes available (i.e., Greedy consumption), thereby minimizing the possibility of discarding generated energy when the battery's state of charge reaches its upper limit. However, if perfect forecast information is available, as for the the Posterior Bound, then an MDP can theoretically perform as as well as the Greedy consumption algorithm, even while maintaining a higher average state of charge for future sensing (Figure 3.8). This suggests that forecasting may enable sensing platforms with completely deferrable loads to add additional un-deferrable loads without significant losses in cumulative power consumption, particularly if more advanced methods are employed to handle forecast uncertainty.

Further, we emphasize that the MDP's Bellman's equation (Equation 3.3) can be modified to disregard scheduled consumption and de-emphasize the benefits of being able to to perform future sensing. This can be achieved by removing the $\theta(a_t, t)$ penalty and modifying Bellman's equation as follows

$$J_t(s_t) = \min_{a_t \in A} \left[\mu(a_t) + J_{t+1}(s_{t+1})\alpha^t\right] \tag{3.6}$$

where α is a discount factor, lessening the influence of future optimization values (i.e., the $\mu(a_t)$ penalty) relative to immediate ones. Under this modified Bellman's equation, with α = 0.9, the time-resolved MDP performance is near identical to the Greedy consumption algorithm, consuming power as it becomes available.

For ocean sensing, we note (1) that deployment objectives often involve monitoring unknown or unpredictable natural phenomena that may occur at any given moment, and (2) that existing ocean observing platforms are often powered by "on demand" energy resources (e.g., cabled power, battery power) or are designed to operate on a duty cycle to reduce average power consumption, while sampling on a consistent basis. Instances of completely deferrable ocean sensing applications are rare, as most data analysis and interpretation relies on consistent, persistent sensing. Examples of largely deferrable loads include computationally-intensive processing and compression of data streams acquired through ocean observations, and power-intensive, high-bandwidth data transmission through low earth orbit satellite networks. As mentioned previously, an advantage of an MDP is that it can be designed to meet the subjective deferrability level (or lack thereof) for any given application.

This being said, loads, by definition, cannot be deferrable if they are completely inflexible. By comparing our MDP to inflexible load cases (Figure 3.10), we find that load inflexibility leads to substantially larger WEC sizes and battery capacities to achieve similar average performance to flexible load schemes, and, in general, have larger tradeoffs across performance metrics. For example, APDC600 comes closest (among inflexible load cases) to matching the MDP in terms of mean power consumption (Figure 3.10a-d), but causes the instrumentation package to experience extended intermittencies, as evidenced by having the lowest theta rates and the largest durations in low and survival modes (Figure 3.10e-p). Similarly, by definition, MPNF operates at 100% persistence, achieving a theta rate of 100% and no time spent in low or survival mode. Consequently, however, MPNF struggles to consume power for sensing, only approaching the MDP's mean power consumption when the energy system is substantially oversized (i.e., 5 meter WEC, >25 kWh battery bank), which has significant logistical implications. These results underscore the operational improvements that may be achieved by incorporating flexible loads into next-generation oceanographic sensing platforms, and, in general, stand-alone renewable power systems.

Finally, we note that we are drawing conclusions about generalized system performance from a relatively short period (two months). This period includes significant variability and intermittency in the wave resource (Figure 3.7), which our MDP, using forecast information, is able to handle more effectively than the Duration-based algorithm (Figure 3.9). For a period with less wave resource variability, all algorithms might be expected to perform similarly. Conversely, for a period with more sustained intermittency (i.e., a longer gap in substantial power generation from the WEC), battery capacity would, eventually, become the limiting factor, such that no amount of algorithm refinement or forecasting could continue to sustain scheduled loads.

3.5.1 Sensitivity Analysis

The penalties and overall design of our Bellman's equation (Equation 3.3) are subjective, intended to reflect operational priorities and capabilities for a generic ocean observation system. These subjective decisions, in practice, are customizable, enabling an MDP algorithm to meet the unique objectives and constraints of a real-world deployment. Here, to demonstrate some of this customizability, we present a sensitivity analysis evaluating algorithm performance across changes in two penalty parameters (θ_h and θ_A, Equation 3.2) and two wave forecast characteristics (the forecast horizon and the interval between discrete forecasts).

We find that modifying penalty parameters produces tradeoffs in MDP performance, changing the algorithm's effectiveness in meeting non-deferrable loads on schedule. For example, in Figure 3.11, we present our MDP's performance sensitivity to changes in θ_h, the time interval governing the $\theta(a_t, t)$ penalty. This interval defines how frequently the MDP is penalized for not operating in full- or medium-power mode and, therefore, defines the schedule of an unspecified, but non-deferrable load. We find that, as θ_h is reduced to 1 hour (meaning that the MDP is penalized for not operating in full- or medium-power mode at all time steps), mean durations in low or survival mode (Figure 3.11c,f) and theta rates decrease (Figure 3.11b,e). In other words, reducing this interval leads to reduced intermittency, but at the expense of a lower success rate in meeting non-deferrable loads on schedule, as the overall number of scheduled loads increases with the reduced interval. Increasing the interval for θ_h has limited effect on the ability to meet scheduled loads since this makes the loads easier to meet and the penalty for not meeting the loads is incurred less frequently. Mean power consumption is relatively insensitive to θ_h, with percentage changes limited to ± 0.5 %.

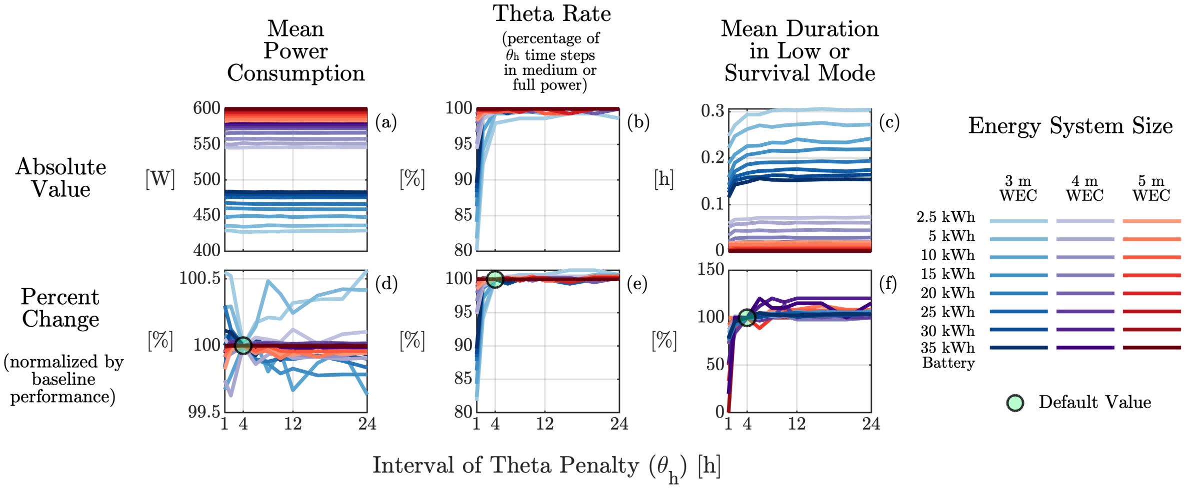

Figure 3.11: MDP performance sensitivity to θ_h (x-axes) in terms of (a,b) mean power consumption, (b,e) theta rate and (c,f) mean duration in low or survival mode. Performance is shown as (a-c) absolute and (d-e) percent changes, determined by normalizing the sensitivity output by baseline performance (i.e., when $\theta_h = 4$ h). Combinations of WEC size and battery capacity are indicated by coloration, with the primary distinction between WEC size and increasing storage capacities represented as darker shading within that color scheme. The default sensitivity value ($\theta_h = 4$ h) is indicated by the filled circle in the percentage change representations (d-e).

In Figure 3.12, we present our MDP's sensitivity to θ_A, the magnitude of the $\theta(a_t, t)$ penalty. This parameter controls how much the MDP prioritizes non-deferrable loads versus instantaneous consumption, such that increasing θ_A places higher priority on meeting non-deferrable loads. We find that the algorithm is largely insensitive to changes in θ_A until $\theta_A < 1$, such that, when $\theta_A = 0$, low and survival mode intermittencies increase and theta rates decrease, signaling a worsened ability to meet non-deferrable loads. This would be acceptable for load applications that are completely deferrable, which other approaches, such as the Greedy algorithm or applying a discount factor to the MDP (Equation 3.6) handle more effectively, producing more substantial increases in mean power consumption across all energy system sizes than shown here. However, as our foremost interest is to understand the utility of forecasting, which is most beneficial for meeting non-deferrable loads, for robustness, we selected a relatively large ($\theta_A = 1000$) magnitude for the $\theta(a_t, t)$ penalty.

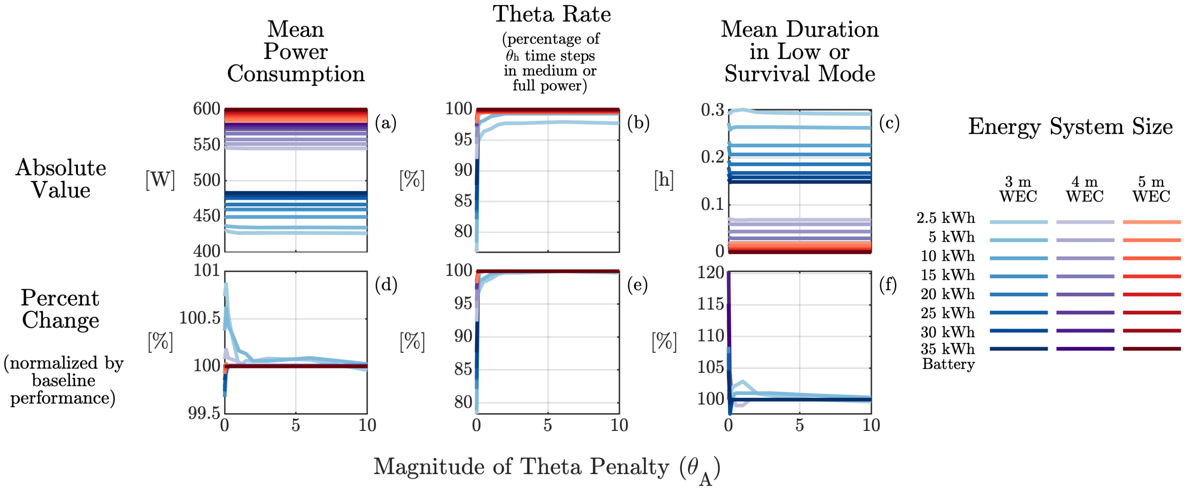

Figure 3.12: MDP performance sensitivity to θ_A (x-axes) in terms of (a,b) mean power consumption, (b,e) theta rate and (c,f) mean duration in low or survival mode. Performance is shown as (a-c) absolute and (d-e) percent changes, determined by normalizing the sensitivity output by baseline performance (i.e., when $\theta_A = 1000$). Combinations of WEC size and battery capacity are indicated by coloration, with the primary distinction between WEC size and increasing storage capacities represented as darker shading within that color scheme. The default sensitivity value ($\theta_A = 1000$) is not contained within the x-axes provided in order to enhance the θ_A values that produce the greatest of sensitivity.

We also consider our MDP's sensitivity to wave forecast characteristics, as access to resource forecasts may differ across applications. We find that the temporal extent and discretization of the forecasts used in our study can be marginally modified without significant degradation in algorithm performance. For example, as the forecast extent is reduced from its default (and maximum) value of 180 hours (Figure 3.13), the MDP's performance is relatively unaffected until the extent falls below 50 hours. Theta rate, in particular, is insensitive to forecast extents > 5 hours, suggesting that to meet non-deferrable loads our MDP, as expected, requires forecasts that are at least as long as the interval these non-deferrable loads are scheduled to be met on. Similarly, as the forecast's discretization increases from its default (and minimum) value of 1 hour, performance metrics are unaffected until the discretization exceeds 5 hours (Figure 3.14). We note that the forecast's discretization is also the duration of time spent in an operational mode, and that when this value exceeds θ_h (> 4 hours), the theta rate is no longer a valid indicator of algorithm performance.

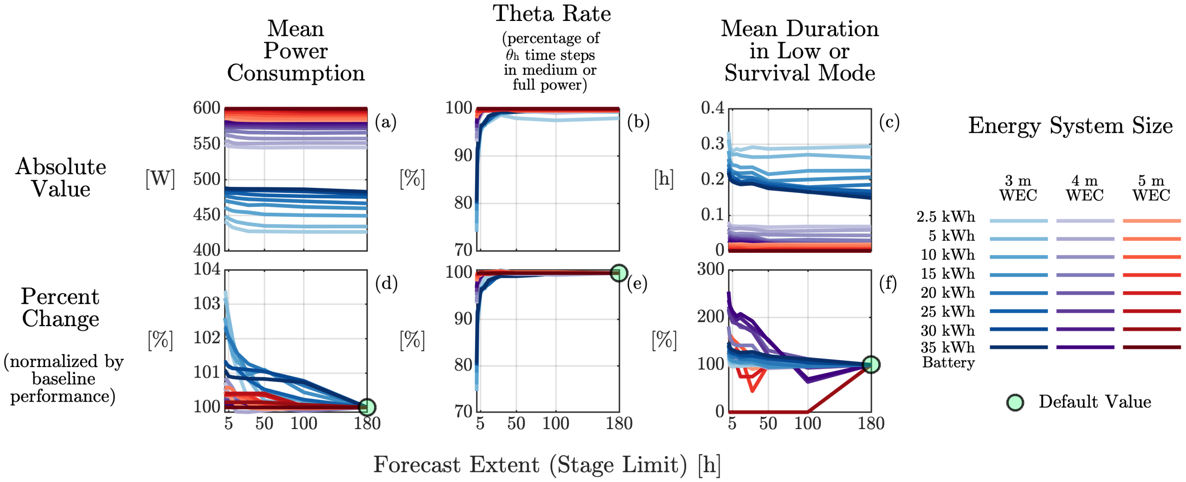

Figure 3.13: MDP performance sensitivity to forecast extent (x-axes) in terms of (a,b) mean power consumption, (b,e) theta rate and (c,f) mean duration in low or survival mode. Performance is shown as (a-c) absolute and (d-e) percent changes, determined by normalizing the sensitivity output by baseline performance (i.e., when forecast extent is 180 hours). Combinations of WEC size and battery capacity are indicated by coloration, with the primary distinction between WEC size and increasing storage capacities represented as darker shading within that color scheme. The default sensitivity value (forecast extent = 180 hours) is indicated by the filled circle in the percentage change representations (d-e).

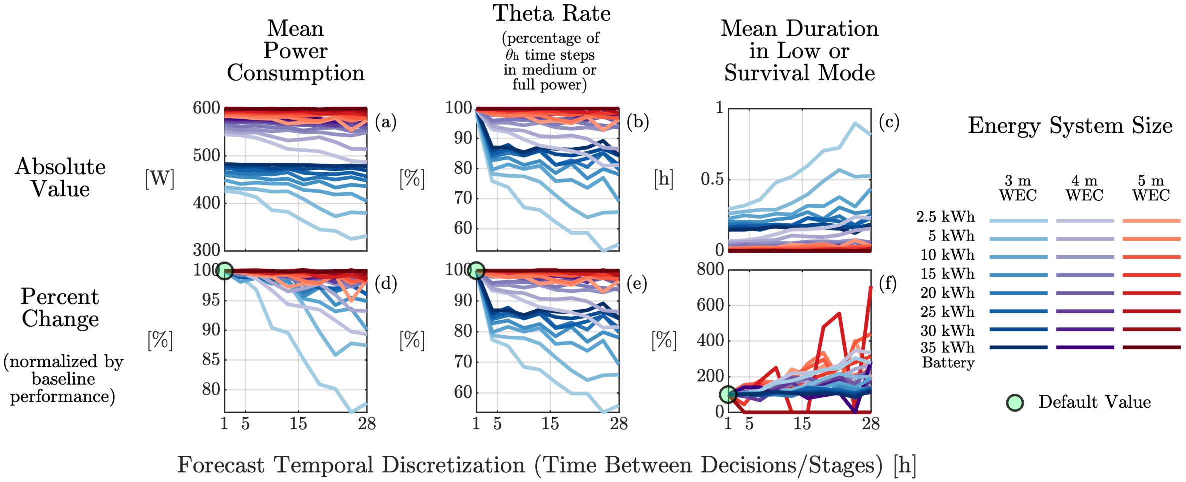

Figure 3.14: MDP performance sensitivity to forecast discretization (x-axes) in terms of (a,b) mean power consumption, (b,e) theta rate and (c,f) mean duration in low or survival mode. Performance is shown as (a-c) absolute and (d-e) percent changes, determined by normalizing the sensitivity output by baseline performance (i.e., when forecast discretization is 1 hour). Combinations of WEC size and battery capacity are indicated by coloration, with the primary distinction between WEC size and increasing storage capacities represented as darker shading within that color scheme. The default sensitivity value (forecast discretization = 1 hour) is indicated by the filled circle in the percentage change representations (d-e).

These results suggest that wave forecasts of lesser extent or coarser resolution can be used without significant losses in algorithm performance, but not beyond shortening forecast extent to 30 hours or coarsening resolution to 5 hours, at which point algorithm performance degrades. We caution that these results would not be expected to apply to simultaneously reducing forecast extent and coarsening temporal resolution.

Additional performance sensitivities are provided in Appendix B.4. We note that even this sensitivity analysis cannot fully express the capabilities of an MDP to meet a specific remote power application due to the vast customization potential of functional penalties and, in general, MDPs.

3.5.2 Computational Implications

We expect it would be feasible to solve the MDP's backward recursion algorithm using the computational capabilities onboard existing ocean observation platforms that are equipped with flexible suites of instruments. We find that, on a singe core of a high performance computer, our forward simulations (1790 consecutive recursions) take approximately 2 hours and 30 minutes to complete. A single recursion, which determines the analytical model's operational status for an hour, requires 1-2 seconds to solve on a standard CPU.

This, however, is based on our baseline MDP, which could be be adjusted for improved performance. As shown by the Posterior Bound (Figure 3.9), which is the outcome of the MDP with perfect forecast information, decision-making performance across all metrics would benefit from methods that can explicitly account for forecast uncertainty. For example, incorporating transition probabilities (Section 3.3.1), may mitigate the influence of forecast uncertainty and improve decision-making, but would increase the number of enumerations (and therefore, runtime) required by a factor of S, which is the number of discrete battery elements in our objective function ($125 \leq S \leq 2000$ in our MDP).

Another approach may be to incorporate data-driven strategies enabled by recent developments in machine learning. This may increase prediction accuracy, and, consequently, decision effectiveness, by inferring datasets and bypassing unknown dynamics, such as those involved in producing site-specific wave forecast error. This has been demonstrated successfully for forecasting wind [Zhang et al., 2014] [Haque et al., 2014] [Wang et al., 2017] [Ak et al., 2015], solar [McCandless et al., 2016] [Chen et al., 2011] [Wang et al., 2012] [Belaid et al., 2020], and wave resources [Cornejo-Bueno et al., 2016] [Fernández et al., 2015] [James et al., 2018], often involving hybrid approaches (i.e., two algorithms working in tandem), suggesting it may be possible to adapt our MDP to account for uncertainty, particularly considering the consistent streams of data entering and exiting the algorithm's objective function. One especially attractive method for this may be reinforcement learning (RL), due to the foundational similarities between MDPs and RL [Whitehead and Lin, 1995] [Otterlo and Wiering, 2012]. However, like transition probabilities, such enhancements would increase the computational cost of decisions and may complicate the practicality of real-time power management, particularly during the training stage.

3.5.3 Relevance to Other Renewable Resources

To our knowledge, this is the first assessment of the benefits of resource forecasting for a stand-alone renewable energy system. While our work considers the specific case of wave-powered ocean observation, other stand-alone deployments powered by a similarly unpredictable energy resource (e.g., wind, solar) may also benefit from forecast-based strategies for power management. Under present levels of forecasting development, none of these resources are decidedly more "forecastable" (i.e., have better forecast accuracy) than others across locations and durations [Widén et al., 2015]. Therefore, we expect that the benefits of forecasting may foremost depend on the characteristics of the load, operational considerations specific to the deployment, and the generation and storage capacities required to meet the deployment objective without forecasting.

We anticipate that, as with our wave-specific study, these benefits will be most impactful when power is used to meet non-deferrable loads on or within a defined schedule. This benefit may be especially meaningful in ocean settings, where the weight of near-surface infrastructure drives the size of the required buoy and, consequently, the complexity and durability of the mooring system. Because of this, oversizing energy equipment to meet scheduled loads is undesirable. Alternatively, the benefits of forecasting may be less meaningful in settings where oversizing is a feasible strategy. One such example is a terrestrial application powered by stand-alone solar panels, where (1) the cost of generation (PV panels) is relatively inexpensive, (2) the diurnal availability of irradiance may enable smaller battery capacities, and (3) the complexity, cost and spatial requirements for supporting infrastructure are relatively low in comparison to marine applications.

Similarly, we anticipate that the benefits of forecasting may be less impactful for hybrid power systems, which use multiple independent resources for electricity and are consequently less vulnerable to intermittencies in a single resource. Further work is needed to understand the benefits of forecasting for autonomous hybrid power systems and, more broadly, compare the effectiveness of using forecasting versus hybrid generation as a means for reducing energy system capacity requirements.

We find that our power management strategies are unlikely to cause sufficient battery degradation over a five-year period to require replacement (Figures 3.9 and 3.10). However, we caution that this observation is provisional and contingent on our application, which features relatively low generation-to-storage ratios, causing battery degradation to be driven by average state of charge, not cycling, as discussed in Section 2.5.4. For applications with smaller battery banks and larger generation-to-storage ratios, such as hybrid or solar-powered systems, degradation may be a more important consideration for forecast-based power management decisions. Furthermore, we note that degradation effects may be challenging to explicitly model within Bellman's Equation due to the requirement that MDP's adhere to the Markov Property (i.e., that state transitions are "history independent").

3.6 Conclusion

In this paper, we assess the benefits of forecasting for a stand-alone renewable energy system. We study the specific case of using forecast information to manage the power consumption of a wave-powered, battery-storage-backed ocean observation system. We develop an analytical model of an ocean observation system that can adaptively switch between four power modes on hourly intervals. We simulate the performance of the observation system using this analytical model for eight power management (or "decision") strategies. In particular, we develop a decision strategy that utilizes a finite-horizon, discrete-time, backward recursion MDP to make decisions that are informed by a 180-hour wave forecast. We compare decision strategies by simulating the analytical model over a two-month period under each decision strategy and across 24 combinations of WEC and battery size. We assess performance in terms of power consumption, intermittency and meeting scheduled consumption targets.

We find that, under this type of forecast-based decision-making, the benefits of forecasting (exemplified by the MDP) are most impactful when loads must be met on or within a defined schedule, and are therefore not completely deferrable. The MDP generally achieves higher levels of power consumption, lower durations of intermittency, and a higher success rate in meeting scheduled load targets than a decision-making algorithm that attempts to meet the load schedule without forecasting. We find that, if loads are completely deferrable, a Greedy algorithm, which does not utilize forecasting and consumes as much power as it can as immediately as becomes available is, by definition, optimal. For such loads, the Greedy algorithm outperforms the MDP. However, the MDP can be adapted to disregard scheduled consumption and achieve performance nearly identical to the Greedy algorithm, underscoring the customizability of the MDP framework and its ability to meet the functional needs of a given application with appropriate design of its objective function.

We find that the influence of forecast uncertainty is notable, as the Posterior Bound (the outcome of the MDP when forecasts with zero error are used to make decisions) outperforms all decision strategies. The Posterior Bound represents the upper limit of the MDP's theoretical performance, suggesting that, with more advanced forms of forecast uncertainty handling, such as reinforcement learning, the MDP's performance could be improved.

Our primary finding, that forecasting improves the power management of non-deferrable ocean observation loads, may facilitate real-world wave-powered ocean observation deployments by reducing the generation and storage capacities (and, consequently, the size of the surface platform) required to accomplish sensing goals. While our analysis focuses on wave-powered ocean observation specifically, this finding may be beneficial for other stand-alone applications powered by similarly unpredictable resources (e.g., solar, wind), particularly those that must avoid oversizing generation and storage capacities for reasons related to cost, space or complexity.

Chapter 4

Conclusion

4.1 Major Conclusions

As outlined in Chapter 1, this thesis describes optimization frameworks I developed to improve our understanding of off-grid wave energy conversion from various perspectives, including its economic requirements, system features, and possible end uses. This focuses on using wave energy for kilowatt-scale applications, such as ocean observation, which are smaller in comparison to using wave energy to power utility grids.

Chapter 2 presents a comparative techno-economic analysis of resource options for powering "in-situ" ocean observations, including solar, wind, wave, and diesel generation. I accomplish this through a techno-economic model that utilizes time domain simulation and optimization to identify cost-optimal generation and storage capacities and total estimated costs across resources. We find that cost-optimal energy system capacities depend on the resource being used, such that generation capacities are lower for the wave and wind resources (< 3.5 kW, and < 1 kW at locations with strong resources) and larger for the solar and diesel resources (> 3 kW, in certain cases exceeding 9 kW). With exception to using solar energy at high latitude, which requires a large (> 175 kWh) battery bank to bridge seasonal asymmetry, battery storage banks < 55 kWh are cost-optimal across resources and locations. We find that solar is a cost-effective option in low-latitude and shallow water environments, where the seasonal continuity of irradiance and lower mooring system costs reduce total estimated costs. Outside of this, in deep water and high-latitude scenarios, the wind, wave and diesel resources are cost comparable, depending on assumptions impacting vessel intervention (e.g., durability, instrumentation maintenance cycles) and resource power density. Future efforts to enable high-latitude in-situ powered ocean observation would benefit from an emphasis on device durability and minimizing vessel intervention, whereas efforts to power equatorial observations may benefit from improving solar panel efficiency and reducing the mooring system cost of larger platforms.

Chapter 3 assesses the benefits of using forecast information to manage the power consumption of a wave-powered, battery-storage backed ocean observation system. To achieve this, I simulate an observation system that can switch between four power states according to eight power management (or "decision") strategies. In particular, we develop a decision strategy that utilizes a finite-horizon, discrete-time, backward recursion Markov Decision Process (MDP) to make decisions that are informed by a 180-hour wave forecast. I find that, under this type of forecast-based decision-making, the benefits of forecasting (exemplified by the MDP) are most impactful when loads must be met on or within a defined schedule. A highlight of the MDP its ability to meet the functional needs of a given application with appropriate design of its objective function. The influence of forecast uncertainty is notable, suggesting that, with more advanced forms of forecast uncertainty handling, such as reinforcement learning, the MDP's performance could be improved. This research may facilitate real-world wave-powered ocean observation deployments by reducing the generation and storage capacities (and, consequently, the size of the surface platform) required to accomplish sensing goals. While our analysis focuses on wave-powered ocean observation specifically, these findings may be beneficial for other stand-alone applications powered by similarly unpredictable resources (e.g., solar, wind), as well as other uses for wave energy in off-grid settings.

4.2 Future Work

A study that considers the cost and suitability of hybrid generation (i.e., multiple resources connected to a single battery bank) would be a natural extension of this analysis, as hybrid solutions have been shown to improve robustness by utilizing multiple intermittent resources in terrestrial micro-grids [Holdmann et al., 2019]. A main challenge in this effort will be navigating complexity of optimizing at higher dimensions (i.e., adding additional generation capacity axes to the objective space to reflect the multiple resource options). This will substantially increase the runtime required for a brute-force search, as was executed in my work. Additionally, optimizing at higher dimensions may also introduce new discontinuities in the objective space due to step changes in how distinct generation sources interface (both economically and in terms of energy) on a combined platform.

Another challenge associated with hybrid analysis is accurately defining the design and cost of the hybrid platform's mooring system. As described in Appendix A.1, I made several assumptions to simplify our mooring evaluations and use them within our broader techno-economic study. There is, at present, a gap in knowledge and accessible software regarding the optimal design of mooring systems for kilowatt-scale power systems in deep-water settings. An independent analysis of these moorings would provide more detailed information on the relationship between platform size and geometry, and mooring system complexity, durability and cost. This would allow future efforts on hybrid power for ocean observation to focus primarily on detailed energy models for each resource, including their inter-dependencies and various uncertainties (e.g., "scenarios" that define durability or operational characteristics).

Last, as the motivational context of both chapters involves the prospective benefits of expanding electricity access to new locations, particularly in the ocean and for ocean observation, further research is needed to certify these benefits and understand consequences. The success of future research will depend on intersectional, transdisciplinary analysis that evaluates the holistic benefits, consequences, externalities, and alternatives associated with improving the capabilities of ocean observation, in particular pertaining to the safety of vulnerable human populations, the climate crisis, and ecosystem health.

4.3 Community-Based Applications for Off-Grid Wave Energy

The methods, knowledge developments, and future work outlined above have relevance beyond the realm of powering ocean observations and similar autonomous micro-grids. For example, these concepts and strategies may also benefit efforts to provide critical renewable-generated resources, such as electricity and desalinated water, for remote and coastal communities across the globe—many of whom are facing urgent impacts and priorities caused by the climate crisis and other inequities, both historical and ongoing.

In the final year of my doctoral studies, I was awarded a one-year Oak Ridge Institute for Science Education Marine Hydrokinetic graduate student fellowship to work in collaboration with the Makah Tribe, a federally-recognized tribe located remotely in Neah Bay, in the northwest corner of the Olympic Peninsula. The objective of our study was to clarify how the Makah Tribe may consider exercising its sovereign interests and authority over its marine space by using locally-available wave energy resources and, in doing so, address Tribal priorities related to emergency preparedness, environmental change and freshwater shortages. I approached this by using and enhancing the computational models I developed throughout my thesis with continuous feedback from Makah Tribal Council, the Makah Ocean Policy Work Group and other relevant decision-makers across Tribal Staff, including Makah Public Works, Makah Operations, the Office of the General Manager, Makah Community Planning and Economic Development, Makah Fisheries Management, Neah Bay Public Safety, the Makah Cultural and Research Center and the Port of Neah Bay. As a condition of the fellowship, I lived near Neah Bay for six months, which aided our communication and improved my understanding of the region's geography, ecology, and infrastructure. Our analysis is ongoing and we plan to continue our collaboration following my graduation.

The Makah Ocean Policy Work Group has protocols to ensure ethical and responsible publication of research projects with graduate students, which includes a sufficient review period for deliverables such as doctoral dissertations. Due to the short amount of time between the conclusion of my fellowship and defense, it was not feasible to meet these review requirements and include the analysis, results, and discussion associated with our project in this dissertation. However, I hope our collaboration, at a high-level, is instructive for the next steps needed to produce *responsible* future outcomes for off-grid wave energy.

4.4 Producing Responsible Outcomes

This thesis evaluates off-grid wave energy under the hope that its influences——if more widely developed——may be beneficial for people and the environment. This aspiration demands that we understand the historical context of industrialized energy development. For centuries, human exploitation of natural resources for energy have denigrated both racialized populations and ecosystems [Lennon, 2017]. This includes how and where energy resources are collected (e.g., mines, drilling, hydraulic fracturing), the placement and impacts of its conversion and distribution infrastructure (e.g., plants, pipelines, oil spills), and the direct, indirect, intentional and unintentional results of energy usage (e.g., pollution, waste, habitat destruction, development of armed forces and policing, wealth accumulation and inequality). Looking to expand alternative energies for relief is akin to prescribing a child ridden with cavities an allegedly enamel-restoring candy. It's plausible that it can be restorative, but given the remedy's similarity to an origin of decimation, a radical investigation is justified and necessary. We must investigate wave energy's fundamental relationship to the root causes of fossil-fuel-driven injustices to determine whether and how wave energy should be implemented [Levenda et al., 2021].

Although the progress of renewable energy is often discussed in terms of cost-competitiveness (e.g., levelized cost of electricity) and system optimization (e.g., conversion efficiency), these metrics do not capture the fundamental issues of our incumbent, fossil-fuel-driven energy system. The industrialization of fossil fuels for electricity, heating and transport was not exacerbatory and threatening due to a lack of prioritization regarding cost or efficiency. Fossil fuels endangered the living world because we did not have an adequate understanding of and appreciation for their externalities and impacts on vulnerable human and non-human populations, particularly under the scale and acceleration at which they were expanded and the longevity of their operational influences (e.g., carbon cycles, abandoned mines). My thesis repeats this lack of understanding and appreciation. It evaluates off-grid wave energy in great detail, yet primarily from the perspective of cost-competitiveness and system-level effectiveness. A more radical investigation is absent from the work included in this dissertation. Consequently, relative to my suggestions toward *cost-effective* and *system-optimized* wave energy, I feel less confident suggesting how *responsible* wave energy outcomes can be achieved. Nevertheless, in my research——particularly during my collaboration with the Makah Tribe, which is not formally part of my thesis——I have felt certain approaches break through; taking a single step toward what could, after hundreds of steps, result in an analysis that truly grasps the human and ecological implications of off-grid wave energy. I conclude my dissertation with the two approaches that I feel most strongly about.

First, I recommend that future developments focus on specific (e.g., application-specific, location-specific, population-specific) uses of wave energy. For the outcomes of wave energy to be responsible, we must locate specific uses that empower the communities and ecosystems that have been most denigrated by industrialization and colonization. We must *also* evaluate and reject uses of wave energy that perpetuate this denigration. For example, on one hand, we may assess how wave-powered ocean observation can protect a hydrothermal vent crawling with biodiversity in the deep sea, or how wave energy can benefit a high-latitude, climate-vulnerable Indigenous community lacking consistent access to electricity or freshwater. On the other hand, we must *also* assess how wave-powered ocean observation can enable destructive seafloor mining operations, or how the material requirements of commercial-scale wave energy may influence geopolitical dynamics, labor practices and mining operations in the Global South. Increased investment in specific assessments like these can help direct wave energy toward responsible outcomes because specifying an application, location, or population situates impacts and end uses within (as opposed to beyond) the scope of research. I am not suggesting that generalized and fundamental research is unimportant. Rather, I am suggesting that specific and applied research should be understood as a way to take control of the historically unevaluated and unappreciated, yet ethically imperative, aspects of energy development, such as environmental externalities and impacts on racialized communities. As an example, in my research, my collaboration with the Makah Tribe was specific to the Makah——enabling more time and opportunity to understand the Tribe's unique history, ecology, priorities, organizational structure and culture than if this were a generalized assessment.

Second, I recommend that future developments prioritize transdisciplinary research that integrates backgrounds, expertise and knowledge systems. In many cases, this is necessary for specific research to be possible. For example, an effective application- or location-specific technology evaluation requires not just technology experts, but also experts in the application being considered and location under evaluation. Increased investment in transdisciplinary research can, therefore, lead us to more effective and accurate outcomes from specific research, as well as *sustained* progress. Conceptually, transdisciplinary research is distinct from inter- or multi-disciplinary research in that it drives the formation of new understandings and approaches from disparate fields [Med, 2006]. By producing a novel approach, discipline, community or understanding, we can set a foundation to continue studying and improving the impact of a research outcome beyond its initial synthesis. When forming transdisciplinary research groups for wave energy, we should place particular emphasis on representing and empowering populations that have been most denigrated and ecosystems most threatened by industrialized energy development (e.g., Indigenous communities, Black communities, the Global South, island communities, low-income communities, water protectors, the arctic, rainforests, oceans) [Finley-Brook and Holloman, 2016]. We can achieve this through both project methods (e.g., co-creation, knowledge sharing, salaried participation) and outcomes (e.g., installed assets that provide critical resources, capacity-building). Transdisciplinary research groups should also include experts beyond engineers and technology developers——such as individuals with experience or training in ecology, ethnic studies, anthropology, history, philosophy, and education—as engineers and technology developers are often not adequately trained to analyze human- and environmental-centered implications. In practice, transdisciplinary research groups for wave energy should consist of (1) wave energy experts, (2) population- or community-specific members, and (3) social scientists, ecologists and non-STEM experts, organized in a non-hierarchical structure and empowered equally to work together and shape the project's outcomes. This recommendation is drawn from my experience, as my opinion on the importance of transdisciplinary research again originates from my collaboration with the Makah Tribe. This collaboration included experts and community members from the broadest variety of any project I participated in throughout my doctoral studies. While I believe our work would have benefited immensely from more thorough involvement (i.e., funding to support) community-member and non-wave-expert participation, we simply would not have identified essential considerations for wave energy if it were not for the limited yet invaluable discussions with those outside my field and background.

These ideas—specific and transdisciplinary research—contradict conventional approaches for technology-centric and engineering research, which can be siloed, implemented hierarchically, and ignorant toward the ethical imperatives we face as humans. Often, scientific research is generalized under the guise of universality or agnosticism, envisioned as an objective, naturally-self-expanding and improving web of human knowledge. This is untrue and obfuscates the impacts (positive and negative) of scientific effort. In reality, our research is selected based on the subjective priorities and intentions of powerful decision-makers that gained control amidst histories of injustice and environmental degradation. By embracing specific research, we can make the downstream impacts of technology development more transparent, empowering more people to understand and shape technological influences. By prioritizing transdisciplinary research, we can improve the accuracy of specific research, reduce the subjectivity of our research directions, and deliberately include populations that have been both restricted from and subjected to the harms of the levers that shape our society. Effectively, these strategies boil down to redistributing agency. By adopting more holistic approaches to research that redistribute agency, we can refine and hopefully "optimize" the humanitarian and ecological impacts that the growing variety of energy systems, such as wave energy, are capable of. Absent this, like an objective function with missing terms, our search for how to engage with natural phenomena and resources is prone to misalignment that is likely to exacerbate, rather than dismantle, ongoing patterns of denigration.

Bibliography

Ahmed, A. and Khalid, M. (2019). A review on the selected applications of forecasting models in renewable power systems. *Renewable and Sustainable Energy Reviews*, 100:9–21.

Ak, R., Fink, O., and Zio, E. (2015). Two machine learning approaches for short-term wind speed time-series prediction. *IEEE transactions on neural networks and learning systems*, 27(8):1734–1747.

Akhter, F., Siddiquei, H. R., Alahi, M. E. E., and Mukhopadhyay, S. C. (2021). Recent advancement of the sensors for monitoring the water quality parameters in smart fisheries farming. *Computers*, 10(3):26

Arzaghi, E., Abaei, M. M., Abbassi, R., O'Reilly, M., Garaniya, V., and Penesis, I. (2020). A markovian approach to power generation capacity assessment of floating wave energy converters. *Renewable Energy*, 146:2736–2743.

Astariz, S. and Iglesias, G. (2015). The economics of wave energy: A review. *Renewable and Sustainable Energy Reviews*, 45:397 – 408.

Baharudin, N., Mansur, T., Ali, R., Wahab, A., Rahman, N., Ariff, E., and Ali, A. (2012). *Mini-grid power system optimization design and economic analysis of solar powered sea water desalination plant for rural communities and emergency relief conditions*. IEEE.

Barnes, C. R. and Tunnicliffe, V. (2008). Building the world's first multi-node cabled ocean observatories (neptune canada and venus, canada): Science, realities, challenges and opportunities. In *OCEANS 2008-MTS/IEEE Kobe Techno-Ocean*, pages 1–8. IEEE.

Belaid, S., Mellit, A., Boualit, H., and Zaiani, M. (2020). Hourly global solar forecasting models based on a supervised machine learning algorithm and time series principle. *International Journal of Ambient Energy*, pages 1–12.

Bellman, R. and Kalaba, R. (1957). Dynamic programming and statistical communication theory. *Proceedings of the National Academy of Sciences of the United States of America*, 43(8):749.

Bennett, C. C. and Hauser, K. (2013). Artificial intelligence framework for simulating clinical decision-making: A markov decision process approach. *Artificial intelligence in medicine*, 57(1):9–19.

Bernard, E. N. and Meinig, C. (2011). History and future of deep-ocean tsunami measurements. In *OCEANS'11 MTS/IEEE KONA*, pages 1–7. IEEE.

Birkl, C. R., Roberts, M. R., McTurk, E., Bruce, P. G., and Howey, D. A. (2017). Degradation diagnostics for lithium ion cells. *Journal of Power Sources*, 341:373–386.

Boget, E. (2020). Personal Communication.

Booij, N., Holthuijsen, L., and Ris, R. (1997). The" swan" wave model for shallow water. In *25th International Conference on Coastal Engineering*, pages 668–676.

Bottenheim, J., Netcheva, S., Morin, S., and Nghiem, S. (2009). Ozone in the boundary layer air over the arctic ocean: measurements during the tara transpolar drift 2006–2008. *Atmospheric Chemistry and Physics*, 9(14):4545–4557 1680–7316.

Boute, A. (2016). Off-grid renewable energy in remote arctic areas: An analysis of the russian far east. *Renewable and Sustainable Energy Reviews*, 59:1029–1037.

Cahill, B., Lewis, T., et al. (2014). Wave periods and the calculation of wave power. In *Marine Energy Technology Symposium*.

Cavagnaro, R. J., Copping, A., Green, R., Greene, D., Jenne, S., Rose, D., and Overhus, D. (2020). Powering the blue economy: Progress exploring marine renewable energy integration with ocean observations. *Marine Technology Society*.

Chang, G., Jones, C. A., Roberts, J. D., and Neary, V. S. (2018). A comprehensive evaluation of factors affecting the levelized cost of wave energy conversion projects. *Renewable Energy*, 127:344–354.

Chauhan, A. and Saini, R. (2015). Renewable energy based off-grid rural electrification in uttarakhand state of india: Technology options, modelling method, barriers and recommendations. *Renewable and Sustainable Energy Reviews*, 51:662–681.

Chen, C., Duan, S., Cai, T., and Liu, B. (2011). Online 24-h solar power forecasting based on weather type classification using artificial neural network. *Solar energy*, 85(11):2856–2870.

Cheung, K. F. (2010). Simulating waves nearshore (swan) regional wave model: Oahu. Distributed by the Pacific Islands Ocean Observing System (PacIOOS).

Chew, G., Pelaccio, D. G., and Johnson, D. (2002). *Study of power system upgrades for NDBC buoys*, volume 1. IEEE.

Clark, A. M. and Sekino, H. (2001). *A multidisciplinary deep sea long-term observatory in Japan*, volume 2. IEEE.

Commission, I. E. (2012). Technical specification 62600-100: Marine energy - wave, tidal and other water current converters - part 100: Electricity producing wave energy converters - power performance assessment.

Copping, A., LiVecchi, A., Spence, H., Gorton, A., Jenne, S., Preus, R., Gill, G., Robichaud, R., and Gore, S. (2018). Maritime renewable energy markets: power from the sea. *Marine Technology Society Journal*, 52(5):99–109.

Copping, A. E., Green, R., Cavagnaro, R. J., Jenne, D. S., Greene, D., Martinez, J. J., and Yang, Y. (2020). Powering the blue economy-ocean observing use cases report. Technical report, Pacific Northwest National Lab.(PNNL), Richland, WA (United States).

Corbus, D., Link, H., Butterfield, S., Stork, C., and Newcomb, C. (1999). Certification testing for small wind turbines. Technical report, National Renewable Energy Lab.(NREL), Golden, CO (United States).

Cornejo-Bueno, L., Nieto-Borge, J., García-Díaz, P., Rodríguez, G., and Salcedo-Sanz, S. (2016). Significant wave height and energy flux prediction for marine energy applications: A grouping genetic algorithm–extreme learning machine approach. *Renewable Energy*, 97:380–389.

Daniel, T., Manley, J., and Trenaman, N. (2011). The wave glider: enabling a new approach to persistent ocean observation and research. *Ocean Dynamics*, 61(10):1509–1520

Datawell, B. (2006). Datawell waverider reference manual. *Datawell BV, Zumerlustraat*, 4:2012.

de Nie, R., Leontaris, G., Hoogendoorn, D., and Wolfert, A. R. M. R. (2019). Offshore infrastructure planning using a vine copula approach for environmental conditions: an application for replacement maintenance of tidal energy infrastructure. *Structure and Infrastructure Engineering*, 15(5):600–617.

DeVisser, A., Cable, B., and Vega, L. (2013). Wave energy test site (wets) marine corps base hawaii. *Energy Ocean International, June*.

Dewey, R. K. (1999). Mooring design & dynamics—a matlab® package for designing and analyzing oceanographic moorings. *Marine Models*, 1(1-4):103–157.

Dillon, T., Maurer, B., Lawson, M., Jenne, D. S., Manalang, D., Baca, E., and Polagye, B. (2022). Cost-optimal wave-powered persistent oceanographic observation. *Renewable Energy*, 181:504–521.

Dillon, T., Maurer, B., Lawson, M., and Polagye, B. (2023a). Forecast-based stochastic optimization for wave energy conversion and storage. Under Internal Review.

Dillon, T., Palmer, S. M., Maurer, B., Gunawan, M., and Polagye, B. (2023b). Techno-economic comparison of resources for powering oceanographic observation. Under Internal Review.

Dizon, C., Cavagnaro, R. J., Robertson, B., and Brekken, T. K. (2021). Modular horizontal pendulum wave energy converter: Exploring feasibility to power ocean observation applications in the us pacific northwest. *IET Renewable Power Generation*, 15(14):3354–3367 1752–1416.

Downing, S. D. and Socie, D. (1982). Simple rainflow counting algorithms. *International journal of fatigue*, 4(1):31–40.

Exizidis, L., Kazempour, J., Pinson, P., De Grève, Z., and Vallée, F. (2017). Impact of public aggregate wind forecasts on electricity market outcomes. *IEEE Transactions on Sustainable Energy*, 8(4):1394–1405.

Feng, X., Ouyang, M., Liu, X., Lu, L., Xia, Y., and He, X. (2018). Thermal runaway mechanism of lithium ion battery for electric vehicles: A review. *Energy Storage Materials*, 10:246 – 267.

Fernández, J. C., Salcedo-Sanz, S., Gutiérrez, P. A., Alexandre, E., and Hervás-Martínez, C. (2015). Significant wave height and energy flux range forecast with machine learning classifiers. *Engineering Applications of Artificial Intelligence*, 43:44–53.

Finley-Brook, M. and Holloman, E. L. (2016). Empowering energy justice. *International journal of environmental research and public health*, 13(9):926.

Fischer, P., Brix, H., Baschek, B., Kraberg, A., Brand, M., Cisewski, B., Riethmüller, R., Breitbach, G., Möller, K. O., Gattuso, J.-P., et al. (2020). Operating cabled underwater observatories in rough shelf-sea environments: a technological challenge. *Frontiers in Marine Science*, 7.

Gentemann, C., Scott, J. P., Mazzini, P. L., Pianca, C., Akella, S., Minnett, P. J., Cornillon, P., Fox-Kemper, B., Cetinić, I., Chin, T. M., et al. (2020). Saildrone: Adaptively sampling the marine environment. *Bulletin of the American Meteorological Society*, 101(6):E744–E762.

Gil, A., De La Torre, M., Dominguez, T., and Rivas, R. (2010). Influence of wind energy forecast in deterministic and probabilistic sizing of reserves. In *international workshop on large-scale integration of wind power into power systems as well as on transmission networks for offshore wind power plants*.

Goodwin, K. D., Muller-Karger, F. E., Djurhuus, A., Allen, L. Z., Allen, A. E., McCrow, J. P., and Hyde, G. C. (2019). Molecular approaches for an operational marine biodiversity observation network. In *World Seas: an Environmental Evaluation*, pages 613–631. Elsevier.

Green, R., Copping, A., Cavagnaro, R., Rose, D., Overhus, D., and Jenne, D. S. (2019). Enabling power at sea: Opportunities for expanded ocean observations through marine renewable energy integration preprint. Technical report, National Renewable Energy Lab.(NREL), Golden, CO (United States).

Greer, J. and Niederman, C. (1975). *Power for data buoys and other remote stations*. IEEE.

Griffin, R. A., Robinson, G. J., West, A., Gloyne-Phillips, I. T., and Unsworth, R. K. (2016). Assessing fish and motile fauna around offshore windfarms using stereo baited video. *PLoS One*, 11(3):e0149701.

Gu, W., Wang, Z., Wu, Z., Luo, Z., Tang, Y., and Wang, J. (2016). An online optimal dispatch schedule for cchp microgrids based on model predictive control. *IEEE transactions on smart grid*, 8(5):2332–2342.

Gunn, K. and Stock-Williams, C. (2012). Quantifying the global wave power resource. *Renewable Energy*, 44:296–304.

Haque, A. U., Nehrir, M. H., and Mandal, P. (2014). A hybrid intelligent model for deterministic and quantile regression approach for probabilistic wind power forecasting. *IEEE Transactions on power systems*, 29(4):1663–1672.

Harris, R. E., Johanning, L., and Wolfram, J. (2004). Mooring systems for wave energy converters: A review of design issues and choices. *Marec2004*.

Hegseth, J. M., Bachynski, E. E., and Martins, J. R. (2020). Integrated design optimization of spar floating wind turbines. *Marine Structures*, 72:102771.

Holdmann, G. P., Wies, R. W., and Vandermeer, J. B. (2019). Renewable energy integration in alaska's remote islanded microgrids: economic drivers, technical strategies, technological niche development, and policy implications. *Proceedings of the IEEE*, 107(9):1820–1837.

Hossain, F. M., Hasanuzzaman, M., Rahim, N., and Ping, H. (2015). Impact of renewable energy on rural electrification in malaysia: a review. *Clean Technologies and Environmental Policy*, 17(4):859–871.

IRENA (2020). Electricity storage valuation framework: Assessing system value and ensuring project viability. Technical report, International Renewable Energy Agency, Abu Dhabi.

Jaguemont, J., Boulon, L., and Dubé, Y. (2016). A comprehensive review of lithium-ion batteries used in hybrid and electric vehicles at cold temperatures. *Applied Energy*, 164:99–114.

James, S. C., Zhang, Y., and O'Donncha, F. (2018). A machine learning framework to forecast wave conditions. *Coastal Engineering*, 137:1–10.

Janssen, P. A. (2008). Progress in ocean wave forecasting. *Journal of Computational Physics*, 227(7):3572–3594.

Janzen, C., McCammon, M., Weingartner, T., Statscewich, H., Winsor, P., Danielson, S., and Heim, R. (2019). Innovative real-time observing capabilities for remote coastal regions. *Frontiers in Marine Science*, 6:176.

Jordan, D. C. and Kurtz, S. R. (2013). Photovoltaic degradation rates—an analytical review. *Progress in photovoltaics: Research and Applications*, 21(1):12–29

Jordan, D. C., Silverman, T. J., Wohlgemuth, J. H., Kurtz, S. R., and VanSant, K. T. (2017). Photovoltaic failure and degradation modes. *Progress in Photovoltaics: Research and Applications*, 25(4):318–326

Joslin, J., Cotter, E., Murphy, P., Gibbs, P., Cavagnaro, R., Crisp, C., Stewart, A. R., Polagye, B., Cross, P. S., Hjetland, E., et al. (2019). The wave-powered adaptable monitoring package: hardware design, installation, and deployment. In *Proceedings of the 13th European Wave and Tidal Energy Conference, Naples, Italy*, pages 1–6.

Kaur, A., Nonnenmacher, L., Pedro, H. T., and Coimbra, C. F. (2016). Benefits of solar forecasting for energy imbalance markets. *Renewable energy*, 86:819–830.

Kelley, D. S., Delaney, J. R., and Team, C. A. (2016). Nsf's cabled array: A wired tectonic plate and overlying ocean. In *OCEANS 2016 MTS/IEEE Monterey*, pages 1–10. IEEE.

Kesavakumar, B., ArulMuthiah, M., Elango, S., Gowthaman, D., Kaliyaperumal, P., Senthilkumar, P., Sridharan, R., and Venkatesan, R. (2013). *Design of optimal power source for NIOT offshore moored buoy system*. IEEE.

Khalid, M., Aguilera, R. P., Savkin, A. V., and Agelidis, V. G. (2018). On maximizing profit of wind-battery supported power station based on wind power and energy price forecasting. *Applied Energy*, 211:764–773.

Khalid, M. and Savkin, A. (2014). Minimization and control of battery energy storage for wind power smoothing: Aggregated, distributed and semi-distributed storage. *Renewable Energy*, 64:105–112.

Klemas, V. (2013). Fisheries applications of remote sensing: an overview. *Fisheries Research*, 148:124–136.

Koenig, J. W. (1999). Biovulnerability of fuels. In *International Colloquium on Fuels*.

Kohler, P. C., LeBlanc, L., and Elliott, J. (2015). Scoop-ndbc's new ocean observing system. In *OCEANS 2015-MTS/IEEE Washington*, pages 1–5. IEEE.

Kolobov, A. (2012). Planning with markov decision processes: An ai perspective. *Synthesis Lectures on Artificial Intelligence and Machine Learning*, 6(1):1–210.

Lagarias, J. C., Reeds, J. A., Wright, M. H., and Wright, P. E. (1998). Convergence properties of the nelder–mead simplex method in low dimensions. *SIAM Journal on optimization*, 9(1):112–147.

Lam, L., Bauer, P., and Kelder, E. (2011). A practical circuit-based model for li-ion battery cells in electric vehicle applications. In *2011 IEEE 33rd International Telecommunications Energy Conference (INTELEC)*, pages 1–9. IEEE.

Laresgoiti, I., Käbitz, S., Ecker, M., and Sauer, D. U. (2015). Modeling mechanical degradation in lithium ion batteries during cycling: Solid electrolyte interphase fracture. *Journal of Power Sources*, 300:112–122.

Lawson, M., Yu, Y.-H., Ruehl, K., Michelen, C., et al. (2014). Development and demonstration of the wec-sim wave energy converter simulation tool. In *2nd Marine Energy Technology Symposium*.

Leimeister, M. and Kolios, A. (2021). Reliability-based design optimization of a spar-type floating offshore wind turbine support structure. *Reliability Engineering & System Safety*, 213:107666.

Lennon, M. (2017). Decolonizing energy: Black lives matter and technoscientific expertise amid solar transitions. *Energy Research & Social Science*, 30:18–27.

Levenda, A. M., Behrsin, I., and Disano, F. (2021). Renewable energy for whom? a global systematic review of the environmental justice implications of renewable energy technologies. *Energy Research & Social Science*, 71:101837.

Li, J., Liu, P., and Li, Z. (2020). Optimal design and techno-economic analysis of a solar-wind-biomass off-grid hybrid power system for remote rural electrification: A case study of west china. *Energy*, 208:118387

Lisell, L., Tetreault, T., and Watson, A. (2009). Solar ready buildings planning guide. Technical report, National Renewable Energy Lab.(NREL), Golden, CO (United States).

Mandelli, S., Barbieri, J., Mereu, R., and Colombo, E. (2016). Off-grid systems for rural electrification in developing countries: Definitions, classification and a comprehensive literature review. *Renewable and Sustainable Energy Reviews*, 58:1621–1646.

Manley, J. and Willcox, S. (2010). The wave glider: A persistent platform for ocean science. In *OCEANS'10 IEEE SYDNEY*, pages 1–5. IEEE.

Marcon, Y., Kopiske, E., Leymann, T., Spiesecke, U., Vittori, V., von Wahl, T., Wintersteller, P., Waldmann, C., and Bohrmann, G. (2019). A rotary sonar for long-term acoustic monitoring of deep-sea gas emissions. In *OCEANS 2019-Marseille*, pages 1–8. IEEE.

Marqusee, J. and Don II, D. J. (2020). Reliability of emergency and standby diesel generators: Impact on energy resiliency solutions. *Applied energy*, 268:114918

Mazzola, S., Vergara, C., Astolfi, M., Li, V., Perez-Arriaga, I., and Macchi, E. (2017). Assessing the value of forecast-based dispatch in the operation of off-grid rural microgrids. *Renewable Energy*, 108:116–125.

McCandless, T., Haupt, S., and Young, G. S. (2016). A regime-dependent artificial neural network technique for short-range solar irradiance forecasting. *Renewable Energy*, 89:351–359.

McLeod, I. and Ringwood, J. V. (2022). Powering data buoys using wave energy: a review of possibilities. *Journal of Ocean Engineering and Marine Energy*, pages 1–16 2198–6452.

McWhorter, J., Wright, D., and Thomas, J. (2016). Coastal data information program (cdip). *Research Ideas and Outcomes*, 2:e8827.

Med, C. I. (2006). Multidisciplinarity, interdisciplinarity and transdis-ciplinarity in health research, services, education and policy: 1. definitions, objectives, and evidence of effectiveness. *Clin Invest Med*, 29(6):351–364.

Meinig, C., Burger, E. F., Cohen, N., Cokelet, E. D., Cronin, M. F., Cross, J. N., De Halleux, S., Jenkins, R., Jessup, A. T., and Mordy, C. W. (2019). Public–private partnerships to advance regional ocean-observing capabilities: a saildrone and noaa-pmel case study and future considerations to expand to global scale observing. *Frontiers in Marine Science*, 6:448

Millner, A. (2010). Modeling lithium ion battery degradation in electric vehicles. In *2010 IEEE Conference on Innovative Technologies for an Efficient and Reliable Electricity Supply*, pages 349–356. IEEE.

Molaeimanesh, G., Mousavi-Khoshdel, S., and Nemati, A. (2020). Experimental analysis of commercial lifepo 4 battery life span used in electric vehicle under extremely cold and hot thermal conditions. *Journal of Thermal Analysis and Calorimetry*, pages 1–10.

Muh, E. and Tabet, F. (2019). Comparative analysis of hybrid renewable energy systems for off-grid applications in southern cameroons. *Renewable Energy*, 135:41–54.

Mundon, T. (2019). Performance evaluation and analysis of a micro-scale wave energy system. In *European Wave and Tidal Energy Conference*.

Neary, V. S., Lawson, M., Previsic, M., Copping, A., Hallett, K. C., LaBonte, A., Rieks, J., and Murray, D. (2014). Methodology for design and economic analysis of marine energy conversion (mec) technologies. Technical report, Sandia National Lab.(SNL-NM), Albuquerque, NM (United States).

Nematbakhsh, A., Olinger, D. J., and Tryggvason, G. (2014). Nonlinear simulation of a spar buoy floating wind turbine under extreme ocean conditions. *Journal of Renewable and Sustainable Energy*, 6(3):033121.

Omar, N., Monem, M. A., Firouz, Y., Salminen, J., Smekens, J., Hegazy, O., Gaulous, H., Mulder, G., Van den Bossche, P., Coosemans, T., et al. (2014). Lithium iron phosphate based battery–assessment of the aging parameters and development of cycle life model. *Applied Energy*, 113:1575–1585.

Orrell, A. C., Sheridan, L. M., and Kazimierczuk, K. (2022). Distributed wind market report: 2022 edition. Technical report, Pacific Northwest National Lab.(PNNL), Richland, WA (United States).

Osse, T. J., Meinig, C., Stalin, S., and Milburn, H. (2015). The prawler, a vertical profiler powered by wave energy. In *OCEANS 2015-MTS/IEEE Washington*, pages 1–8. IEEE.

Otterlo, M. v. and Wiering, M. (2012). Reinforcement learning and markov decision processes. In *Reinforcement learning*, pages 3–42. Springer.

Pattanaik, B., Rao, Y., Vishwanath, A., and Jalihal, P. (2021). *Instrumentation and Data acquisition system of wave powered navigational buoy*. IEEE.

Pettigrew, N. R., Roesler, C. S., Neville, F., and Deese, H. E. (2006). *An operational real-time ocean sensor network in the Gulf of Maine*. Springer.

Pinkel, R., Goldin, M., Smith, J., Sun, O., Aja, A., Bui, M., and Hughen, T. (2011). The wirewalker: A vertically profiling instrument carrier powered by ocean waves. *Journal of Atmospheric and Oceanic Technology*, 28(3):426–435

Polagye, B., Joslin, J., Murphy, P., Cotter, E., Scott, M., Gibbs, P., Bassett, C., and Stewart, A. (2020). Adaptable monitoring package development and deployment: Lessons learned for integrated instrumentation at marine energy sites. *Journal of Marine Science and Engineering*, 8(8):553.

Pradhan, P., Kishore, S., and Defourny, B. (2018). Optimal predictive maintenance policy for an ocean wave farm. *IEEE Transactions on Sustainable Energy*, 10(4):1993–2004.

Puterman, M. L. (2014). *Markov decision processes: discrete stochastic dynamic programming*. John Wiley & Sons.

Ramasamy, V., Zuboy, J., O'Shaughnessy, E., Feldman, D., Desai, J., Woodhouse, M., Basore, P., and Margolis, R. (2022). Us solar photovoltaic system and energy storage cost benchmarks, with minimum sustainable price analysis: Q1 2022. Technical report, National Renewable Energy Lab.(NREL), Golden, CO (United States).

Reikard, G. and Rogers, W. E. (2011). Forecasting ocean waves: Comparing a physics-based model with statistical models. *Coastal Engineering*, 58(5):409–416.

Robert, F. C., Sisodia, G. S., and Gopalan, S. (2018). A critical review on the utilization of storage and demand response for the implementation of renewable energy microgrids. *Sustainable cities and society*, 40:735–745.

Robertson, B., Bekker, J., and Buckham, B. (2020). Renewable integration for remote communities: Comparative allowable cost analyses for hydro, solar and wave energy. *Applied Energy*, 264:114677

Roemmich, D., Johnson, G. C., Riser, S., Davis, R., Gilson, J., Owens, W. B., Garzoli, S. L., Schmid, C., and Ignaszewski, M. (2009). The argo program: Observing the global ocean with profiling floats. *Oceanography*, 22(2):34–43.

Rynne, P. and von Ellenrieder, K. D. (2008). *A wind and solar-powered autonomous surface vehicle for sea surface measurements*. IEEE.

Rysgaard, S., Bjerge, K., Boone, W., Frandsen, E., Graversen, M., Høye, T. T., Jensen, B., Johnen, G., Jackowicz-Korczynski, M. A., and Kerby, J. T. (2022). A mobile observatory powered by sun and wind for near real time measurements of atmospheric, glacial, terrestrial, limnic and coastal oceanic conditions in remote off-grid areas. *HardwareX*, 12:e00331

Sastri, A., Christian, J. R., Achterberg, E. P., Atamanchuk, D., Buck, J. J. H., Bresnahan, P. J., Duke, P. J., Evans, W., Gonski, S. F., Johnson, B., et al. (2019). Perspectives on in situ sensors for ocean acidification research. *Frontiers in Marine Science*, 6:653.

Setiawan, A. A., Zhao, Y., and Nayar, C. V. (2009). Design, economic analysis and environmental considerations of mini-grid hybrid power system with reverse osmosis desalination plant for remote areas. *Renewable energy*, 34(2):374–383

Shaahid, S. and Elhadidy, M. (2007). Technical and economic assessment of grid-independent hybrid photovoltaic–diesel–battery power systems for commercial loads in desert environments. *Renewable and Sustainable Energy Reviews*, 11(8):1794–1810.

Sheehan, E. V., Bridger, D., Nancollas, S. J., and Pittman, S. J. (2020). Pelagicam: A novel underwater imaging system with computer vision for semi-automated monitoring of mobile marine fauna at offshore structures. *Environmental Monitoring and Assessment*, 192(1):11.

Skop, R. (1988). Mooring systems: a state-of-the-art review. *J. Offshore Mech. Arct. Eng.*

Smith, L. M., Barth, J. A., Kelley, D. S., Plueddemann, A., Rodero, I., Ulses, G. A., Vardaro, M. F., and Weller, R. (2018). The ocean observatories initiative. *Oceanography*, 31(1):16–35.

Standard, A. (2009). Awea small wind turbine performance and safety standard. Technical report, American Wind Energy Association.

Sutton, R. S., Barto, A. G., and Williams, R. J. (1992). Reinforcement learning is direct adaptive optimal control. *IEEE Control Systems Magazine*, 12(2):19–22.

Talbert, J. (2021). Personal Communication.

Teillant, B., Costello, R., Weber, J., and Ringwood, J. (2012). Productivity and economic assessment of wave energy projects through operational simulations. *Renewable Energy*, 48:220–230.

Teng, C.-C., Cucullu, S., McArthur, S., Kohler, C., Burnett, B., and Bernard, L. (2010). Vandalism of data buoys. *Mar. Weather Log*, 54(1).

Tennekes, H. (1973). The logarithmic wind profile. *Journal of Atmospheric sciences*, 30(2):234–238

Thirunavukkarasu, M. and Sawle, Y. (2021). A comparative study of the optimal sizing and management of off-grid solar/wind/diesel and battery energy systems for remote areas. *Frontiers in Energy Research*, 9:752043

Thomson, J., Talbert, J., de Klerk, A., Brown, A., Schwendeman, M., Goldsmith, J., Thomas, J., Olfe, C., Cameron, G., and Meinig, C. (2015). Biofouling effects on the response of a wave measurement buoy in deep water. *Journal of Atmospheric and Oceanic Technology*, 32(6):1281–1286.

Van Dover, C. L. (2014). Impacts of anthropogenic disturbances at deep-sea hydrothermal vent ecosystems: a review. *Marine environmental research*, 102:59–72.

Van Dover, C. L., Ardron, J., Escobar, E., Gianni, M., Gjerde, K., Jaeckel, A., Jones, D., Levin, L., Niner, H., Pendleton, L., et al. (2017). Biodiversity loss from deep-sea mining. *Nature Geoscience*, 10(7):464–465.

Vonnahme, T. R., Molari, M., Janssen, F., Wenzhöfer, F., Haeckel, M., Titschack, J., and Boetius, A. (2020). Effects of a deep-sea mining experiment on seafloor microbial communities and functions after 26 years. *Science Advances*, 6(18):eaaz5922.

Walker, H. (2018). Best practices for operation and maintenance of photovoltaic and energy storage systems. Technical report, National Renewable Energy Lab.(NREL).

Wang, F., Mi, Z., Su, S., and Zhao, H. (2012). Short-term solar irradiance forecasting model based on artificial neural network using statistical feature parameters. *Energies*, 5(5):1355–1370.

Wang, H.-z., Li, G.-q., Wang, G.-b., Peng, J.-c., Jiang, H., and Liu, Y.-t. (2017). Deep learning based ensemble approach for probabilistic wind power forecasting. *Applied energy*, 188:56–70.

Wang, L., Li, H., and Jiang, J. (2022). A high-efficiency wave-powered marine observation buoy: Design, analysis, and experimental tests. *Energy Conversion and Management*, 270:116154

Wang, Q., Martinez-Anido, C. B., Wu, H., Florita, A. R., and Hodge, B.-M. (2016). Quantifying the economic and grid reliability impacts of improved wind power forecasting. *IEEE Transactions on Sustainable Energy*, 7(4):1525–1537.

Whaley, C. (2016). Best practices in photovoltaic system operations and maintenance. Technical report, National Renewable Energy Lab.(NREL), Golden, CO (United States).

White, D. J. (1993). A survey of applications of markov decision processes. *Journal of the operational research society*, 44(11):1073–1096.

Whitehead, S. D. and Lin, L.-J. (1995). Reinforcement learning of non-markov decision processes. *Artificial intelligence*, 73(1-2):271–306.

Whitt, C., Pearlman, J., Polagye, B., Caimi, F., Muller-Karger, F., Copping, A., Spence, H., Madhusudhana, S., Kirkwood, W., Grosjean, L., et al. (2020). Future vision for autonomous ocean observations. *Frontiers in Marine Science*, 7:697.

Widén, J., Carpman, N., Castellucci, V., Lingfors, D., Olauson, J., Remouit, F., Bergkvist, M., Grabbe, M., and Waters, R. (2015). Variability assessment and forecasting of renewables: A review for solar, wind, wave and tidal resources. *Renewable and Sustainable Energy Reviews*, 44:356–375.

Xu, B. (2020). Personal Communication.

Xu, B., Oudalov, A., Ulbig, A., Andersson, G., and Kirschen, D. S. (2016). Modeling of lithium-ion battery degradation for cell life assessment. *IEEE Transactions on Smart Grid*, 9(2):1131–1140.

Yang, Y., Bremner, S., Menictas, C., and Kay, M. (2018). Battery energy storage system size determination in renewable energy systems: A review. *Renewable and Sustainable Energy Reviews*, 91:109–125.

Ye, Y., Shi, Y., and Tay, A. A. (2012). Electro-thermal cycle life model for lithium iron phosphate battery. *Journal of Power Sources*, 217:509–518.

Zhang, S., Xu, K., and Jow, T. (2003). The low temperature performance of li-ion batteries. *Journal of Power Sources*, 115(1):137–140.

Zhang, Y., Wang, J., and Wang, X. (2014). Review on probabilistic forecasting of wind power generation. *Renewable and Sustainable Energy Reviews*, 32:255–270.

Chapter A

Chapter 2 Appendix

A.1 Mooring Design and Dynamics

Tables A.1 and A.2 provide sub-component costs for the 40 moorings (combinations of float diameter and water depth) shown in Tables 2.4, 2.5 and 2.6.

All mooring analysis was performed in the MDD software package. This assumes a single-point mooring with user-defined sequence of in-line elements selected from a comprehensive catalogue (e.g., line, anchor, intermediate buoyancy, chain, shackles, acoustic release). Elements can be added to the catalogue by specifying geometry, drag coefficient, material and buoyancy, and we used this feature to design surface float geometries representing the generation platforms studied in this work (e.g., wind spar). For each resource, we assessed surface float sizes and mooring system designs/lengths that span the range of generation capacities (Table 2.9) and water depths (Figure 2.1b) evaluated in our study.

To capture variations driven by water depth, two mooring configurations were evaluated. Deep water (> 500 meters) moorings are based on the Ocean Station Papa 166 Waverider mooring, which incorporates subsurface flotation to add a “false bottom” to the mooring system, reducing the watch circle, adding compliance, and simplifying deployment. Shallow water ($\leq$ 500 meters) moorings, which use less subsurface flotation and introduce compliance through longer nylon line segments (scope $\approx$ 2), were based on the recommended layout for Waverider buoys deployed in water depths exceeding 200 meters, provided in the Datawell Waverider reference manual [Datawell, 2006].

Table A.1: Estimated mooring sub-component costs for wave resource

	1 m WEC Diameter				
	120 m	**500 m**	**1000 m**	**3000 m**	**5000 m**
Acoustic Release	$4,284	$19,656	$19,656	$19,656	$19,656
Anchor	$1,820	$2,730	$3,640	$2,730	$2,730
Chain, Shackles, Links and Swivels	$979	$979	$3,522	$3,522	$3,522
Line	$2,636	$11,138	$12,435	$33,688	$91,320
Subsurface Buoyancy	$931	$4,003	$8,576	$8,576	$12,079
Total	$10,651	$38,506	$47,828	$68,172	$129,307

	3 m WEC Diameter				
	120 m	**500 m**	**1000 m**	**3000 m**	**5000 m**
Acoustic Release	$4,284	$19,656	$19,656	$19,656	$19,656
Anchor	$2,730	$3,640	$4,549	$3,640	$3,640
Chain, Shackles, Links and Swivels	$979	$979	$3,522	$3,522	$3,522
Line	$2,636	$16,639	$18,576	$50,326	$91,320
Subsurface Buoyancy	$931	$3,072	$8,576	$8,576	$12,079
Total	$11,561	$43,985	$54,880	$85,720	$130,217

	6 m WEC Diameter				
	120 m	**500 m**	**1000 m**	**3000 m**	**5000 m**
Acoustic Release	$4,284	$19,656	$19,656	$19,656	$19,656
Anchor	$5,459	$9,099	$9,099	$9,099	$9,099
Chain, Shackles, Links and Swivels	$979	$1,198	$3,934	$4,043	$4,043
Line	$8,480	$16,639	$18,576	$50,326	$91,322
Subsurface Buoyancy	$931	$3,072	$8,576	$8,576	$12,079
Total	$20,134	$49,663	$59,841	$91,700	$136,199

Table A.2: Estimated mooring sub-component costs for solar and diesel resources

	2 m Platform Diameter				
	120 m	**500 m**	**1000 m**	**3000 m**	**5000 m**
Acoustic Release	$4,284	$19,656	$19,656	$19,656	$19,656
Anchor	$2,730	$3,185	$3,640	$3,640	$4,095
Chain, Shackles, Links and Swivels	$948	$979	$3,491	$3,491	$3,491
Line	$2,636	$11,138	$18,576	$52,159	$92,703
Subsurface Buoyancy	$931	$4,003	$8,576	$8,576	$8,576
Total	$11,529	$38,961	$53,939	$87,522	$128,521

	4 m Platform Diameter				
	120 m	**500 m**	**1000 m**	**3000 m**	**5000 m**
Acoustic Release	$4,284	$19,656	$19,656	$19,656	$19,656
Anchor	$5,914	$5,914	$11,374	$5,914	$5,914
Chain, Shackles, Links and Swivels	$1,150	$1,198	$3,947	$4,026	$3,995
Line	$3,939	$16,639	$18,576	$52,159	$92,703
Subsurface Buoyancy	$931	$3,072	$8,576	$8,576	$8,576
Total	$16,218	$46,479	$62,129	$90,331	$130,844

	8 m Platform Diameter				
	120 m	**500 m**	**1000 m**	**3000 m**	**5000 m**
Acoustic Release	$4,284	$19,656	$19,656	$19,656	$19,656
Anchor	$11,829	$11,829	$11,374	$11,374	$11,374
Chain, Shackles, Links and Swivels	$1,150	$1,198	$3,490	$3,995	$3,995
Line	$8,480	$35,824	$39,995	$112,301	$199,595
Subsurface Buoyancy	$931	$3,072	$8,576	$8,576	$8,576
Total	$26,674	$71,578	$83,091	$155,902	$243,196

	12 m Platform Diameter				
	120 m	**500 m**	**1000 m**	**3000 m**	**5000 m**
Total	$80,021	$214,735	$249,274	$467,706	$729,587

Table A.3: Estimated mooring sub-component costs for wind resource

	0.8 m Spar Diameter				
	120 m	**500 m**	**1000 m**	**3000 m**	**5000 m**
Acoustic Release	$4,284	$19,656	$19,656	$19,656	$19,656
Anchor	$2,730	$3,185	$3,185	$4,095	$4,095
Chain, Shackles, Links and Swivels	$948	$979	$3,491	$3,491	$3,491
Line	$2,636	$11,138	$19,782	$51,934	$92,703
Subsurface Buoyancy	$931	$4,003	$8,576	$8,576	$8,576
Total	$11,529	$38,961	$54,689	$87,751	$128,521

Moorings are tested for survivability (i.e., failure of any in-line component) using the MDD software environment. Two test conditions are considered. The first is working condition in which the system experiences net buoyancy and drag force from ocean currents. For all locations considered these are based on a current profile from Station Papa and we note that this would, in reality, vary by location, adding a third dimension to the mooring cost matrices. The second is an extreme condition corresponding to the maximum horizontal orbital velocity throughout the water column for an 18 meter wave height and 15 s wave period. These velocities are estimated using linear (Airy) wave theory. As for the current profile, this extreme condition would, in reality, vary by location. For a given mooring configuration and test condition (working or extreme), MDD solves for the equilibrium position of each in-line element. We then compare the forces acting on each element to the failure loads, adjusting subsurface flotation, line diameter, and anchor weight as needed to achieve a safety factor > 2.5 in working conditions and > 4.5 in extreme conditions. The larger factor safety factor for extreme conditions is to account for a higher probability of "snap loading" during extreme events, which would be more likely to cause system failure than constant tension.

We then use the test condition with the highest cost as the cost of the specific mooring configuration. As discussed below, the WEC mooring is allowed to "blow down" in extreme conditions, while the solar, wind, and diesel platforms are required to remain on the surface to prevent damage to equipment. For the latter resources, this places an additional design constraint on the mooring configuration.

The unit costs of in line elements were sourced from a variety of vendors, including Obert Marine Supply (WA, USA), Yale Coordage (ME, USA), McLane Flotation (MA, USA), Bloch Steel (WA, USA), and EdgeTech (MA, USA). Polyethylene line was chosen due to its high strengths. In waters shallower than 200 meters, less expensive acoustic releases rated to smaller depths become viable, resulting in a significant cost reduction for moorings in the shallowest water. We corrected items sourced prior to 2022 for inflation.

Due to a lack of published information on moorings for solar, wind, and diesel generation at this scale, we made several assumptions to estimate the cost of in line mooring elements (C_{lineel}). For solar and diesel platforms, we modeled the surface element as a buoyant cylinder with a height of 1 meter, drag coefficient of 2, and calculated the buoyancy required for a draft of 0.1 meter in an unmoored condition (i.e., with zero tension force from the mooring line acting on the surface element). Because solar conversion is less spatially dense than the other resources, large (> 10 meter diameter) solar platforms are required for some locations and sensitivity cases. We found that simulations of this platform size caused numerical instabilities in MDD. For larger platforms, multi-point mooring systems are common [Skop, 1988]. Therefore, we estimated the cost of in-line mooring elements (C_{lineel}) for a 12 meter platform (the upper limit required for solar evaluation) for a three point mooring by applying a 3x multiplier to the in-line element cost of the 8 meter mooring, and applied the same multiplier on the installation duration. For platform sizes between 8 meters and 12 meters, we linearly interpolate. We note that, for our baseline results, the maximum required solar platform size is 8.1 meter diameter and the multi-point mooring assumption has negligible effect. In the case of diesel generation, systems are much more compact and can be incorporated into a 2 meter diameter platform with the same form factor as the solar platform.

For wind platforms, we assume a buoyant spar design, which, for megawatt-scale turbines, is an ongoing area of research [Leimeister and Kolios, 2021] [Hegseth et al., 2020]. Rather than attempt a first-principles spar optimization for our scale for generation, we base our spar design and mooring cost on simplified assumptions found through iterative use of MDD. For this scale of wind turbine, we found that platform size is set by the buoyancy required to prevent blowdown from forces acting on the mooring during energetic ocean conditions (as opposed to being set by buoyancy to support turbine weight or righting moment to resist turbine thrust). We found that a spar with a diameter of 0.8 meters, slender height-to-diameter aspect ratio of five [Nematbakhsh et al., 2014], drag coefficient of two, and a buoyancy requirement of 50% draft in an unmoored condition is sufficient to prevent blow down across turbine sizes evaluated. This allows the wind model for C_{lineel} to be reduced to a function of water depth.

WECs were modeled as a buoyant cylindrical surface element with drag coefficient of two and height-to-diameter aspect ratio of five. In practice, WEC buoyancy could be designed or actively controlled to locate the WEC on the surface in working conditions and “blow down” in extreme events as a survival strategy. We manually tuned the buoyancy of the cylindrical surface element in MDD to approximate this performance.

To capture variations driven by water depth, two mooring types were evaluated. Deep water (> 500 meters) moorings are based on the Ocean Station Papa 166 Waverider mooring, which incorporates subsurface flotation to add a “false bottom” to the mooring system, reducing the watch circle, adding compliance, and simplifying deployment. Shallow water ($\leq$ 500 meters) moorings, which use less subsurface flotation and introduce compliance through longer nylon line segments (scope $\approx$ 2), were based on the recommended layout for Waverider buoys deployed in water depths exceeding 200 meters, provided in the Datawell Waverider reference manual [Datawell, 2006].

Across all resources, moorings were tested for survivability using the MDD software environment. MDD solves for the positions of each in-line element iteratively until a static force-balance is found. We assume this static force balance sufficiently captures working and maximum loads on the system, and adjust subsurface flotation, line diameter and anchor weight to achieve factors of safety greater than 2.5 in working conditions and 4.5 in extreme conditions. Working conditions are based on a typical current profile from Station Papa, which we note would vary depending on the ocean currents at specific deployment locations. Extreme conditions are approximated by the maximum horizontal water particle velocities throughout the water column using linear (Airy) wave theory for an 18 meter wave height and 15 second period wave. The larger factor of safety threshold for extreme conditions is based on the larger probability of snap loading during extreme events, which is more likely to cause system failure than constant tension.

When evaluating the solar, diesel and wind moorings in MDD, we did not accept solutions that caused the surface element to submerge or “blow down” in the extreme condition, assuming this could damage equipment.

The unit costs of in line elements were sourced from a variety of vendors, including Obert Marine Supply (WA, USA), Yale Coordage (ME, USA), McLane Flotation (MA, USA), Bloch Steel (WA, USA), and EdgeTech (MA, USA). Polyethylene line was chosen due to its high strengths. In waters shallower than 200 meters, less expensive acoustic releases rated to smaller depths become viable, resulting in a significant cost reduction for moorings in the shallowest water. We corrected items sourced prior to 2022 for inflation.

Finally, we note that since [Dillon et al., 2022] was published, MDD was adapted to rectify an error in drag force calculation for partially submerged surface floats, which (in addition to inflation) is why cost of in-line elements for the wave resource (Table 2.4) increased here from the estimates presented in [Dillon et al., 2022].

A.2 Small-Scale ($\leq$ 20 kW) Diesel Generator Trends

In Section 2.3.1, we define a relationship for small-scale ($\leq$ 20 kW) diesel generator mass as a function of G_r. This was found through a non-negative linear regression, shown in Figure A.1.

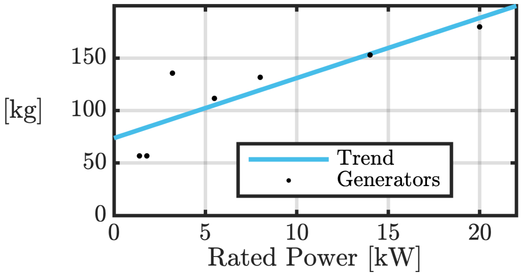

Figure A.1: Non-negative linear regression of mass versus rated power of 9 commercially-available sub-20 kW diesel generators. Data points were found from online vendors.

In Section 2.3.1, we define a relationship for the cost of small-scale ($\leq$ 20 kW) diesel generators as a function of G_r, $C_{\text{dgen}}(G_r)$. This was found through a non-negative linear regression, shown in Figure A.2.

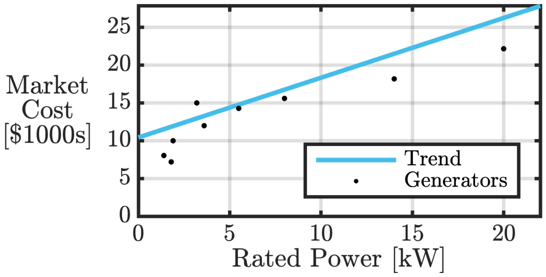

Figure A.2: Non-negative linear regression of market cost versus rated power of 9 commercially-available sub-20 kW diesel generators. Data points were found from online vendors.

In Section 2.3.1, we define the unit volume of small-scale ($\leq$ 20 kW) diesel generators as constant (0.22 m^3) across power ratings. This was found through a non-negative linear regression, shown in Figure A.3.

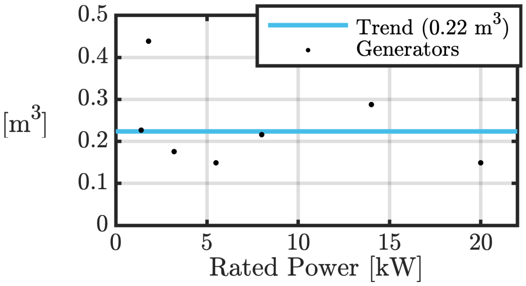

Figure A.3: Non-negative linear regression of length versus rated power of 9 commercially-available sub-20 kW diesel generators. Data points were found from online vendors.

In Section 2.3.2, we define a relationship for fuel consumption in liters per hour as a function of G_r. This was found through a non-negative linear regression, shown in Figure A.4.

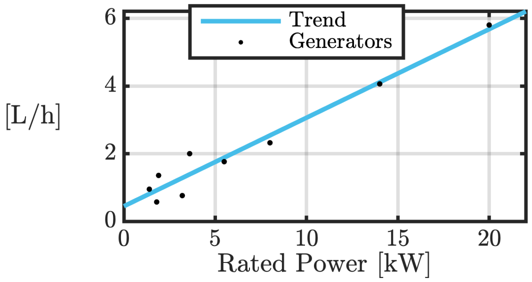

Figure A.4: Non-negative linear regression of fuel consumption versus rated power of 9 commercially-available sub-20 kW diesel generators. Data points were found from online vendors.

A.3 Cost of Small-Scale ($\leq$ 10 kW) Distributed Wind Turbines

In Section 2.3.1, we define the unit cost of small-scale ($\leq$ 10 kW) distributed wind turbines as α_{turb} = \$2848/kW. α_{wind} is found through a non-negative linear regression, shown in Figure A.5.

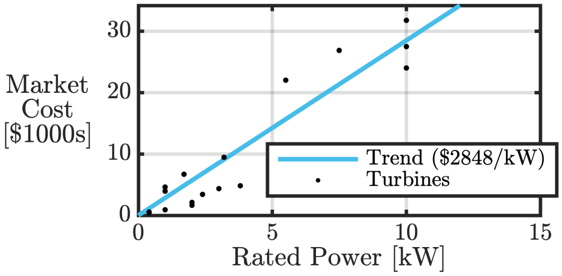

Figure A.5: Non-negative linear regression of market cost versus rated power of 18 commercially-available sub-10 kW wind turbines. Data points were found from online vendors.

A.4 Adjusting Wind Speed to Rotor Height

As mentioned in Section 2.3.2, when calculating wind power output, we adjust wind speed from the measurement height to the rotor height using a logarithmic profile assumption [Tennekes, 1973]. Rotor height (h_r) is found by assuming the bottom of the rotor is 4 meters above the water surface, such that

$$h_r = 4 + \sqrt{\frac{2G_r}{\eta_{\text{turb}}\rho_{\text{air}}\pi u_{ra}^3}} \tag{A.1}$$

where turbine rated power (G_r) is in watts for dimensional consistency, η_{turb} is turbine efficiency (assumed to be 35%), and ρ_{air} is the density of air (1.225 kgm^{-3}). Adjusted wind speed (u_t) is then found from the measured wind speed (u_m) as

$$u_t = u_m \frac{\ln \frac{h_r}{z_o}}{\ln \frac{h_m}{z_o}} \tag{A.2}$$

where h_m is the measurement height (reported at 10 meters) and z_o is surface roughness (0.02 mm) converted to meters. In simulation, we find that the required turbine diameter ranges from 1.8 to 3.8 meters, such that the turbine hub height ranges from 4.9 to 5.9 meters. As shown in Figure A.7, the assumed surface roughness value has little effect on system cost.

A.5 WEC-Sim Damping Coefficients

As discussed in Section 2.3.2, the following five damping coefficients (a WEC-Sim input), provided in table A.4 were used to produce our WEC generation model.

Table A.4: WEC-Sim damping coefficients

31,250 $\mathrm{N(ms^{-1})^{-1}}$
62,500 $\mathrm{N(ms^{-1})^{-1}}$
93,750 $\mathrm{N(ms^{-1})^{-1}}$
125,000 $\mathrm{N(ms^{-1})^{-1}}$
156,200 $\mathrm{N(ms^{-1})^{-1}}$

A.6 Cost Tables

Tables A.5 to A.20 provide the numerical and sub-component cost estimates of our model, shown graphically in Figure 2.6.

A.7 Additional Sensitivity Parameters

In Section 2.4.1, we present a sensitivity analysis evaluating cost across changes in parameters that define our assumptions. Here, in Figures A.6, A.7, and A.8, we provide cost sensitivity to additional parameters. We note that the sensitivities shown here are, in general, smaller, indicating that our model estimates are not as dependent on these assumptions relative to those provided in the body of the paper. To make these

Table A.5: Sub-costs for solar, automated cleaning, short-term instrumentation

	Argentine Basin	**Coastal Endurance**	**Irminger Sea**
Mooring Elements	\$150.2k	\$62k	\$146k
Mooring Installation	\$29.4k	\$14.5k	\$21.6k
Platform	\$5.7k	\$9.3k	\$15.2k
Battery Cells	\$3.7k	\$4.7k	\$82.9k
Battery Housing	\$3.7k	\$4.7k	\$82.9k
Panels	\$3.9k	\$6.4k	\$10.5k
Electrical Infrastructure	\$2.5k	\$4.2k	\$6.8k
Structural Infrastructure	\$0.7k	\$1.2k	\$2k
Assembly	\$0.5k	\$0.9k	\$1.5k
Battery Replacements	\$0k	\$0k	\$0k
Vessel Operations	\$0k	\$0k	\$0k
Total	\$200.4k	\$107.8k	\$369.3k

Table A.6: Sub-costs for solar, automated cleaning, long-term instrumentation

	Argentine Basin	**Coastal Endurance**	**Irminger Sea**
Mooring Elements	\$150.2k	\$62k	\$146k
Mooring Installation	\$29.4k	\$14.5k	\$21.6k
Platform	\$5.7k	\$9.3k	\$15.2k
Battery Cells	\$3.7k	\$4.7k	\$82.9k
Battery Housing	\$3.7k	\$4.7k	\$82.9k
Panels	\$3.9k	\$6.4k	\$10.5k
Electrical Infrastructure	\$2.5k	\$4.2k	\$6.8k
Structural Infrastructure	\$0.7k	\$1.2k	\$2k
Assembly	\$0.5k	\$0.9k	\$1.5k
Battery Replacements	\$0k	\$0k	\$0k
Vessel Operations	\$0k	\$0k	\$0k
Total	\$200.4k	\$107.8k	\$369.3k

Table A.7: Sub-costs for solar, human cleaning, short-term instrumentation

	Argentine Basin	**Coastal Endurance**	**Irminger Sea**
Mooring Elements	\$156.9k	\$64.4k	\$146k
Mooring Installation	\$29.4k	\$14.5k	\$21.6k
Platform	\$6.3k	\$10.5k	\$15.2k
Battery Cells	\$3.7k	\$4.7k	\$95.1k
Battery Housing	\$3.7k	\$4.7k	\$95.1k
Panels	\$2.2k	\$3.6k	\$5.2k
Electrical Infrastructure	\$1.4k	\$2.3k	\$3.4k
Structural Infrastructure	\$0.4k	\$0.7k	\$1k
Assembly	\$0.6k	\$1k	\$1.5k
Battery Replacements	\$0k	\$0k	\$0k
Vessel Operations	\$0k	\$0k	\$0k
Total	\$204.6k	\$106.4k	\$383.9k

Table A.8: Sub-costs for solar, human cleaning, long-term instrumentation

	Argentine Basin	Coastal Endurance	Irminger Sea
Mooring Elements	$186.4k	$73.9k	$148.5k
Mooring Installation	$29.4k	$14.8k	$22k
Platform	$9.3k	$15.2k	$15.3k
Battery Cells	$4.2k	$5.1k	$138.5k
Battery Housing	$4.2k	$5.1k	$138.5k
Panels	$3.2k	$5.3k	$5.3k
Electrical Infrastructure	$2.1k	$3.4k	$3.4k
Structural Infrastructure	$0.6k	$1k	$1k
Assembly	$0.9k	$1.5k	$1.5k
Battery Replacements	$0k	$0k	$0k
Vessel Operations	$205.7k	$19.6k	$39.1k
Total	$445.9k	$144.9k	$513.1k

Table A.9: Sub-costs for wind, optimistic durability, short-term instrumentation

	Argentine Basin	Coastal Endurance	Irminger Sea
Mooring Elements	$123.6k	$40.3k	$82.5k
Mooring Installation	$29.4k	$14.5k	$21.4k
Platform	$0.1k	$0.5k	$0.2k
Battery Cells	$7k	$15.8k	$9.3k
Battery Housing	$7k	$15.8k	$9.3k
Turbine	$7.8k	$34.3k	$13.5k
Assembly	$3.5k	$15.2k	$6k
Battery Replacements	$0k	$0k	$0k
Turbine Repair	$0k	$0k	$0k
Vessel Operations	$0k	$0k	$0k
Total	$178.4k	$136.5k	$142.3k

Table A.10: Sub-costs for wind, optimistic durability, long-term instrumentation

	Argentine Basin	Coastal Endurance	Irminger Sea
Mooring Elements	$123.6k	$40.3k	$82.5k
Mooring Installation	$29.4k	$14.5k	$21.4k
Platform	$0.1k	$0.5k	$0.2k
Battery Cells	$7k	$15.8k	$9.3k
Battery Housing	$7k	$15.8k	$9.3k
Turbine	$7.8k	$34.3k	$13.5k
Assembly	$3.5k	$15.2k	$6k
Battery Replacements	$0k	$0k	$0k
Turbine Repair	$0k	$0k	$0k
Vessel Operations	$0k	$0k	$0k
Total	$178.4k	$136.5k	$142.3k

Table A.11: Sub-costs for wind, conservative durability, short-term instrumentation

	Argentine Basin	**Coastal Endurance**	**Irminger Sea**
Mooring Elements	$123.6k	$40.3k	$82.5k
Mooring Installation	$29.4k	$14.5k	$21.4k
Platform	$0.1k	$0.4k	$0.2k
Battery Cells	$7.5k	$21.4k	$11.7k
Battery Housing	$7.5k	$21.4k	$11.7k
Turbine	$7.4k	$27.8k	$11.2k
Assembly	$3.3k	$12.3k	$5k
Battery Replacements	$0k	$0k	$0k
Turbine Repair	$13.3k	$50.2k	$20.3k
Vessel Operations	$24k	$24k	$20.3k
Total	$215.8k	$212.3k	$187.9k

Table A.12: Sub-costs for wind, conservative durability, long-term instrumentation

	Argentine Basin	**Coastal Endurance**	**Irminger Sea**
Mooring Elements	$123.6k	$40.3k	$82.5k
Mooring Installation	$29.4k	$14.5k	$21.4k
Platform	$0.1k	$0.4k	$0.2k
Battery Cells	$7.5k	$21.4k	$11.7k
Battery Housing	$7.5k	$21.4k	$11.7k
Turbine	$7.4k	$27.8k	$11.2k
Assembly	$3.3k	$12.3k	$5k
Battery Replacements	$0k	$0k	$0k
Turbine Repair	$13.3k	$50.2k	$20.3k
Vessel Operations	$514.1k	$48.9k	$97.8k
Total	$706k	$237.2k	$261.7k

Table A.13: Sub-costs for wave, optimistic WEC durability scenario, short-term instrumentation

	Argentine Basin	**Coastal Endurance**	**Irminger Sea**
Mooring Elements	$123.2k	$44.1k	$68.6k
Mooring Installation	$29.4k	$14.5k	$21.4k
Battery Cells	$15.4k	$20k	$7.9k
Battery Housing	$15.4k	$20k	$7.9k
WEC Device	$46k	$137.5k	$28.2k
WEC Installation	$3.7k	$11k	$2.3k
Battery Replacements	$0k	$0k	$0k
WEC Refurbishments	$0k	$0k	$0k
Vessel Operations	$0k	$0k	$0k
Total	$233k	$247.2k	$136.3k

Table A.14: Sub-costs for wave, optimistic WEC durability scenario, long-term instrumentation

	Argentine Basin	**Coastal Endurance**	**Irminger Sea**
Mooring Elements	$123.2k	$44.1k	$68.6k
Mooring Installation	$29.4k	$14.5k	$21.4k
Battery Cells	$15.4k	$20k	$7.9k
Battery Housing	$15.4k	$20k	$7.9k
WEC Device	$46k	$137.5k	$28.2k
WEC Installation	$3.7k	$11k	$2.3k
Battery Replacements	$0k	$0k	$0k
WEC Refurbishments	$0k	$0k	$0k
Vessel Operations	$0k	$0k	$0k
Total	$233k	$247.2k	$136.3k

Table A.15: Sub-costs for wave, optimistic WEC cost scenario, short-term instrumentation

	Argentine Basin	**Coastal Endurance**	**Irminger Sea**
Mooring Elements	$123.2k	$44.1k	$68.6k
Mooring Installation	$29.4k	$14.5k	$21.4k
Battery Cells	$15.4k	$20k	$7.9k
Battery Housing	$15.4k	$20k	$7.9k
WEC Device	$18.4k	$55k	$11.3k
WEC Installation	$3.7k	$11k	$2.3k
Battery Replacements	$0k	$0k	$0k
WEC Refurbishments	$27.6k	$82.5k	$16.9k
Vessel Operations	$24k	$24k	$24k
Total	$257k	$271.1k	$160.2k

Table A.16: Sub-costs for wave, optimistic WEC cost scenario, long-term instrumentation

	Argentine Basin	**Coastal Endurance**	**Irminger Sea**
Mooring Elements	$123.2k	$44.1k	$68.6k
Mooring Installation	$29.4k	$14.5k	$21.4k
Battery Cells	$15.4k	$20k	$7.9k
Battery Housing	$15.4k	$20k	$7.9k
WEC Device	$18.4k	$55k	$11.3k
WEC Installation	$3.7k	$11k	$2.3k
Battery Replacements	$0k	$0k	$0k
WEC Refurbishments	$27.6k	$82.5k	$16.9k
Vessel Operations	$514.1k	$48.9k	$97.8k
Total	$747.2k	$296k	$234k

Table A.17: Sub-costs for wave, conservative scenario, short-term instrumentation

	Argentine Basin	**Coastal Endurance**	**Irminger Sea**
Mooring Elements	$123.1k	$44k	$68.4k
Mooring Installation	$29.4k	$14.5k	$21.4k
Battery Cells	$19.1k	$23.8k	$8.9k
Battery Housing	$19.1k	$23.8k	$8.9k
WEC Device	$42.5k	$134k	$27.3k
WEC Installation	$3.4k	$10.7k	$2.2k
Battery Replacements	$0k	$0k	$0k
WEC Refurbishments	$57.3k	$180.8k	$36.9k
Vessel Operations	$24k	$24k	$24k
Total	$317.8k	$455.5k	$197.9k

Table A.18: Sub-costs for wave, conservative scenario, long-term instrumentation

	Argentine Basin	**Coastal Endurance**	**Irminger Sea**
Mooring Elements	$123.1k	$44k	$68.4k
Mooring Installation	$29.4k	$14.5k	$21.4k
Battery Cells	$19.1k	$23.8k	$8.9k
Battery Housing	$19.1k	$23.8k	$8.9k
WEC Device	$42.5k	$134k	$27.3k
WEC Installation	$3.4k	$10.7k	$2.2k
Battery Replacements	$0k	$0k	$0k
WEC Refurbishments	$57.3k	$180.8k	$36.9k
Vessel Operations	$514.1k	$48.9k	$97.8k
Total	$808k	$480.4k	$271.7k

Table A.19: Sub-costs for diesel short-term instrumentation

	Argentine Basin	**Coastal Endurance**	**Irminger Sea**
Mooring Elements	$123.6k	$40.2k	$82.2k
Mooring Installation	$29.4k	$14.5k	$21.4k
Platform	$1.1k	$1.1k	$1.1k
Battery Cells	$3.3k	$3.3k	$3.3k
Battery Housing	$3.3k	$3.3k	$3.3k
Diesel Generator	$34.4k	$34.4k	$34.4k
Generator Enclosure	$0.9k	$0.9k	$0.9k
Fuel	$4.4k	$4.4k	$4.4k
Battery Replacements	$0k	$0k	$0k
Generator Repair	$8.8k	$8.8k	$8.8k
Vessel Operations	$28.7k	$28.7k	$28.7k
Total	$237.9k	$139.7k	$188.6k

Table A.20: Sub-costs for diesel, long-term instrumentation

	Argentine Basin	**Coastal Endurance**	**Irminger Sea**
Mooring Elements	\$123.6k	\$40.2k	\$82.2k
Mooring Installation	\$29.4k	\$14.5k	\$21.4k
Platform	\$1.3k	\$1.3k	\$1.3k
Battery Cells	\$5.1k	\$5.1k	\$5.1k
Battery Housing	\$5.1k	\$5.1k	\$5.1k
Diesel Generator	\$40.2k	\$40.2k	\$40.2k
Generator Enclosure	\$0.9k	\$0.9k	\$0.9k
Fuel	\$4.1k	\$4.1k	\$4.1k
Battery Replacements	\$0k	\$0k	\$0k
Generator Repair	\$10.3k	\$10.3k	\$10.3k
Vessel Operations	\$411.3k	\$39.1k	\$78.2k
Total	\$631.3k	\$160.9k	\$248.9k

sensitivities visible, the axes limits are significantly reduced in comparison to Figures 2.7 to 2.10. In Section 2.3.1, we describe our approach to estimating platform cost (C_{plat}) for solar, wind and diesel generation, which includes an assumption that platform mass is five times the generation system mass. This assumption is included here as "platform mass multiplier" and we note that the solar resource is more sensitive to this assumption than wind and diesel due to the larger spatial requirement of solar panels.

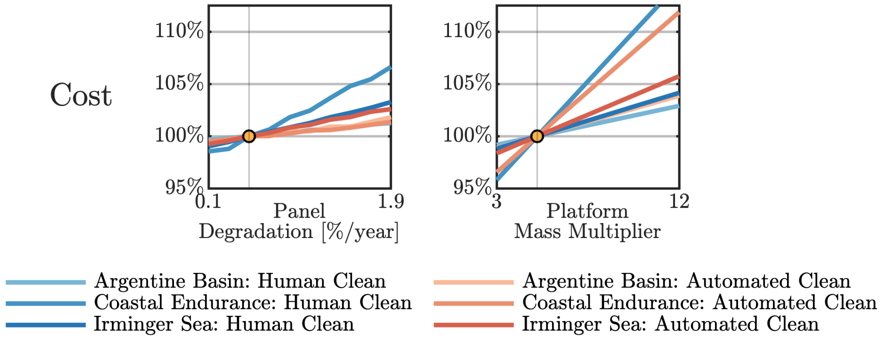

Figure A.6: Cost sensitivities for powering the long-term instrumentation use case at all locations with solar under the automated and human cleaning scenarios. Sensitivities are shown by changes in select parameters (x-axes) versus percentage of baseline cost (y-axes). Baseline values are indicated by orange data points. Note that, as cost is less sensitive to these parameters, the axes have been narrowed relative to the sensitivities provided in Figure 2.7.

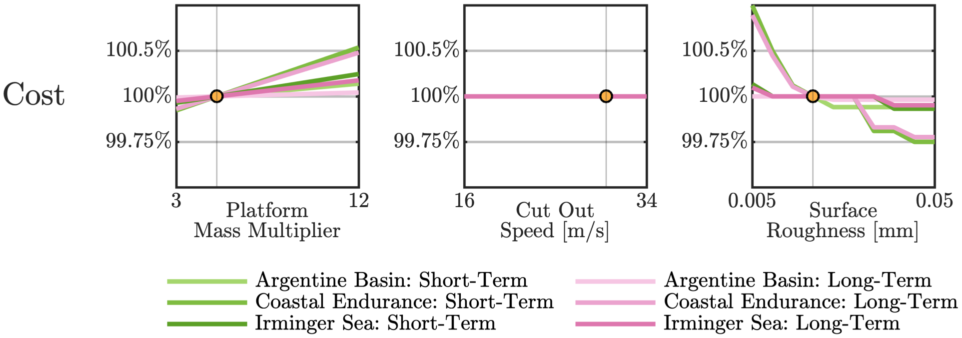

Figure A.7: Cost sensitivities for powering all combinations of location and use case with wind under the conservative scenario. Sensitivities are shown by changes in select parameters (x-axes) versus percentage of baseline cost (y-axes). Baseline values are indicated by orange data points. Note that, as cost is less sensitive to these parameters, the axes have been narrowed relative to the sensitivities provided in Figure 2.8.

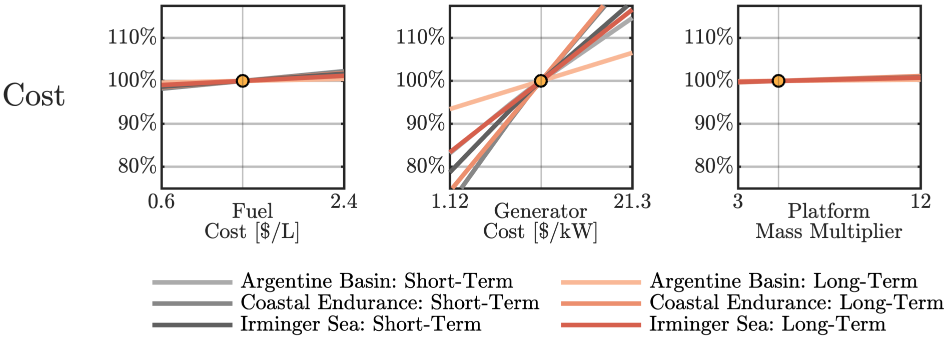

Figure A.8: Cost sensitivities for powering all combinations of location and use case with diesel generation. Sensitivities are shown by changes in select parameters (x-axes) versus percentage of baseline cost (y-axes). Baseline values are indicated by orange data points. Note that, as cost is less sensitive to these parameters, the axes have been narrowed relative to the sensitivities provided in Figure 2.10.

Chapter B

Chapter 3 Appendix

B.1 State Space Discretization

The state space discretization value (d_s = 20 Wh) was found by conducting our simulation suite with a set discretization value, reconstructing each state space time series without discretization post-simulation, and comparing these two outputs graphically. This is shown in Section 3.4. We also analyzed changes in algorithm performance with changing discretization value and found that performance destabilizes when d_s exceeds 40 Wh. This is shown in Appendix B.4. We selected d_s = 20 Wh because this was robust to the destabilization that occurs at larger discretization and resulted in good agreement between the discretized and reconstructed timeseries. The finer the discretization, the higher the computational cost of the simulation.

B.2 WEC-sim damping coefficients

As discussed in Section 3.3.3, the following five damping coefficients (a WEC-Sim input), provided in table B.1 were used to produce our WEC generation model.

Table B.1: WEC-Sim Damping Coefficients

31,250 $\mathrm{N(ms^{-1})^{-1}}$
62,500 $\mathrm{N(ms^{-1})^{-1}}$
93,750 $\mathrm{N(ms^{-1})^{-1}}$
125,000 $\mathrm{N(ms^{-1})^{-1}}$
156,200 $\mathrm{N(ms^{-1})^{-1}}$

B.3 Time Series Comparison of Additional WEC and Battery Sizes

In Figure 3.8, we present time series diagnostics comparing decisions schemes for our analytical model with a three meter WEC and 10 kWh battery bank. Here, in Figures B.1, B.2, B.3, B.4 and B.5, we provide the same time series diagnostics for additional WEC (three, four and five meter) and battery (10 and 30 kWh) sizes. As mentioned in Section 3.4, energy system size is a preeminent factor in improving sensing performance.

B.4 Additional Sensitivity Parameters

In Section 3.5.1, we present a sensitivity analysis evaluating our MDP's performance across changes in four parameters controlling objective function penalties and forecast characteristics. Here, in Figures B.6, B.7, B.8, B.9, B.10, B.11, and B.12, we provide our MDP's sensitivity to additional parameters. With exception to electrical conversion efficiency and WEC hotel load (Figures B.6 and B.7), which influence power availability, we find that MDP performance is less sensitive to the parameters provided here, indicating that our algorithm is robust toward the assumptions that involve these parameters.

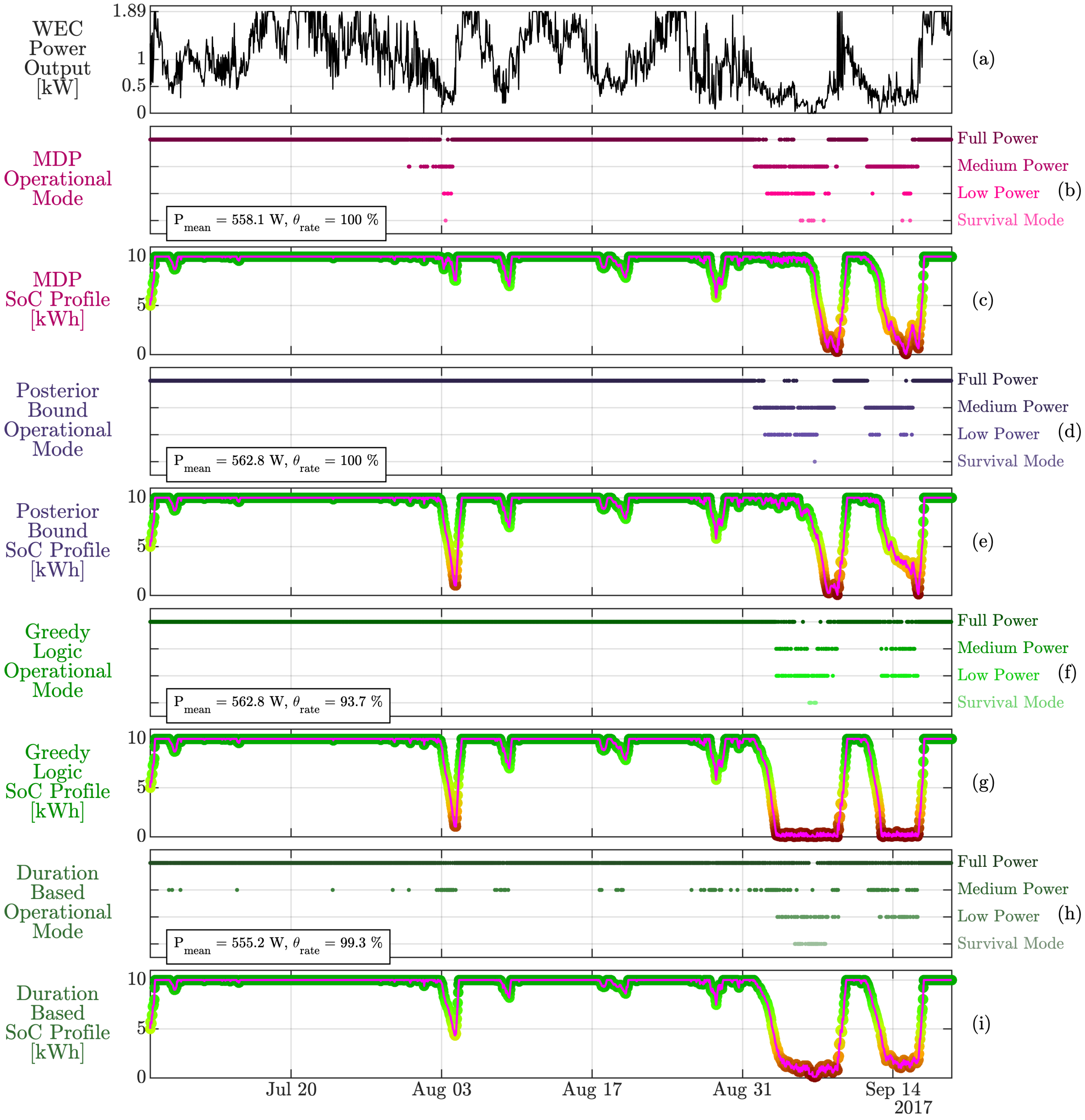

Figure B.1: Time series, over the entire simulation window, of (a) WEC power output, operational mode, and battery state of charge of forward simulations under (b, c) MDP, (d, e) Posterior Bound, (f, g) Greedy, and (h, i) Duration-Based decision-making. Annotations show two performance metric values: mean power consumption (P_{mean}) and theta rate (θ_{rate}) for each decision schema. The pink lines (c, e, g, i) show the discretization validation discussed in Appendix B.1.

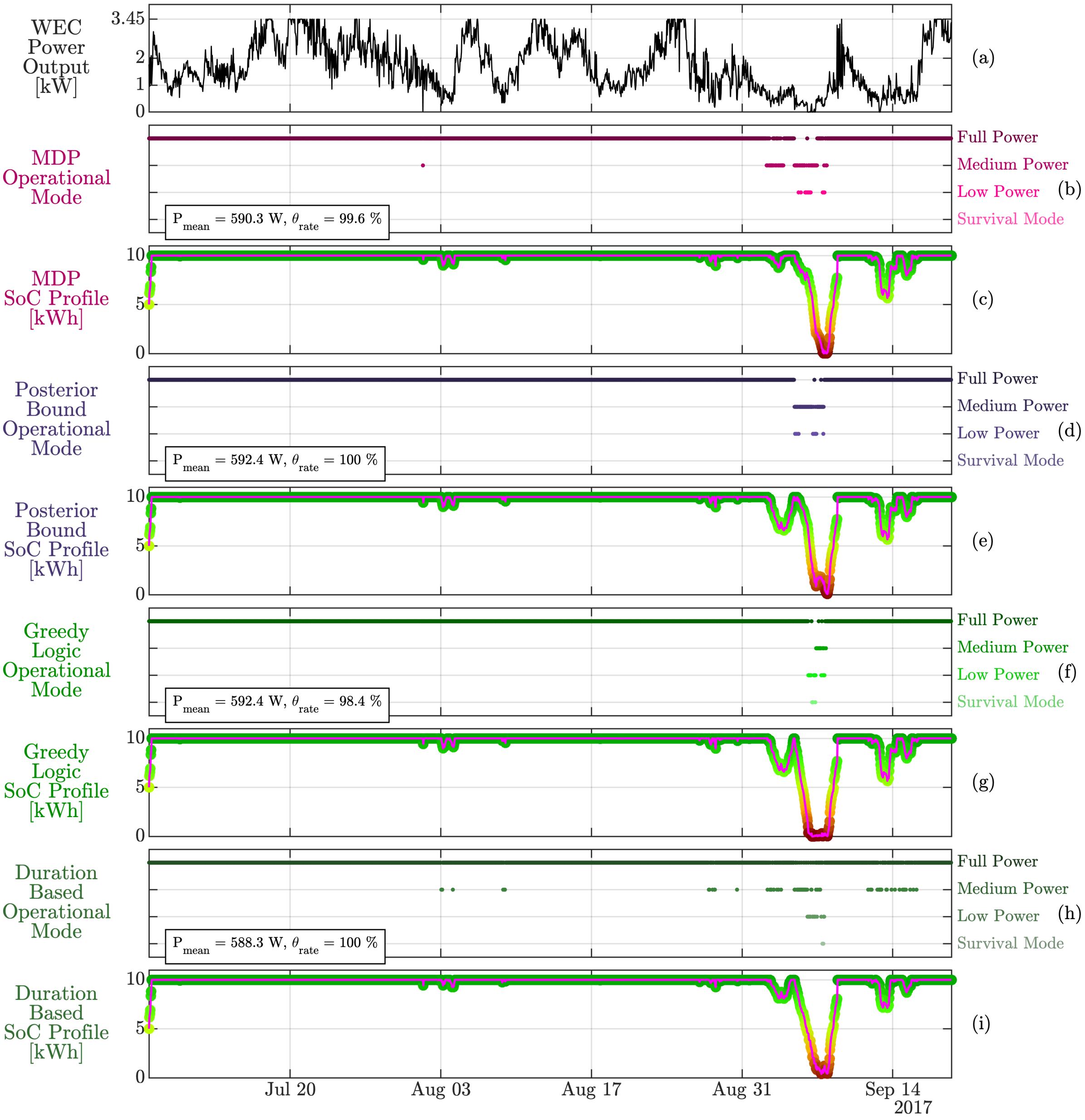

Figure B.2: Time series, over the entire simulation window, of (a) WEC power output, operational mode, and battery state of charge of forward simulations under (b, c) MDP, (d, e) Posterior Bound, (f, g) Greedy, and (h, i) Duration-Based decision-making. Annotations show two performance metric values: mean power consumption (P_{mean}) and theta rate (θ_{rate}) for each decision schema. The pink lines (c, e, g, i) show the discretization validation discussed in Appendix B.1.

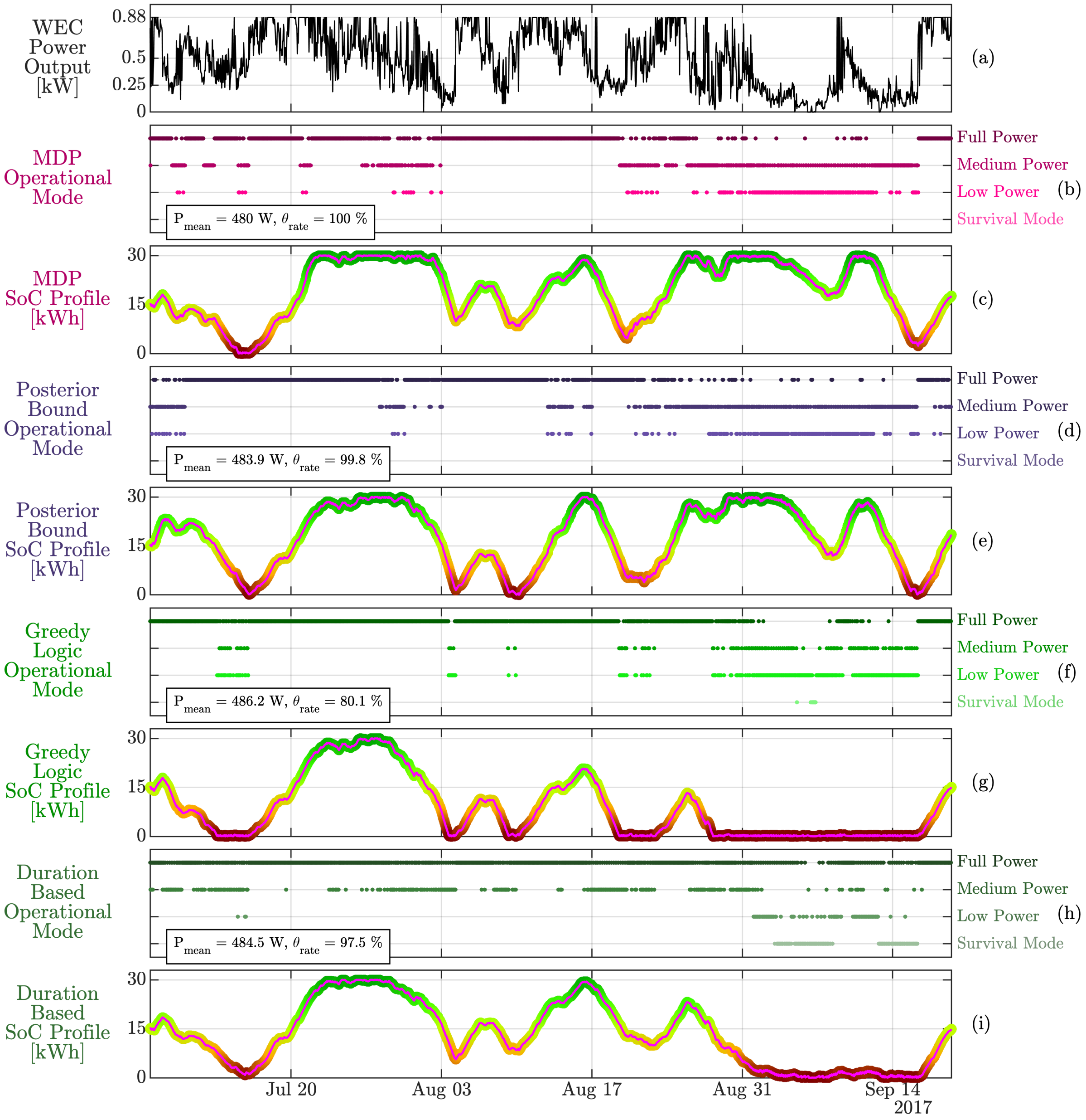

Figure B.3: Time series, over the entire simulation window, of (a) WEC power output, operational mode, and battery state of charge of forward simulations under (b, c) MDP, (d, e) Posterior Bound, (f, g) Greedy, and (h, i) Duration-Based decision-making. Annotations show two performance metric values: mean power consumption (P_{mean}) and theta rate (θ_{rate}) for each decision schema. The pink lines (c, e, g, i) show the discretization validation discussed in Appendix B.1.

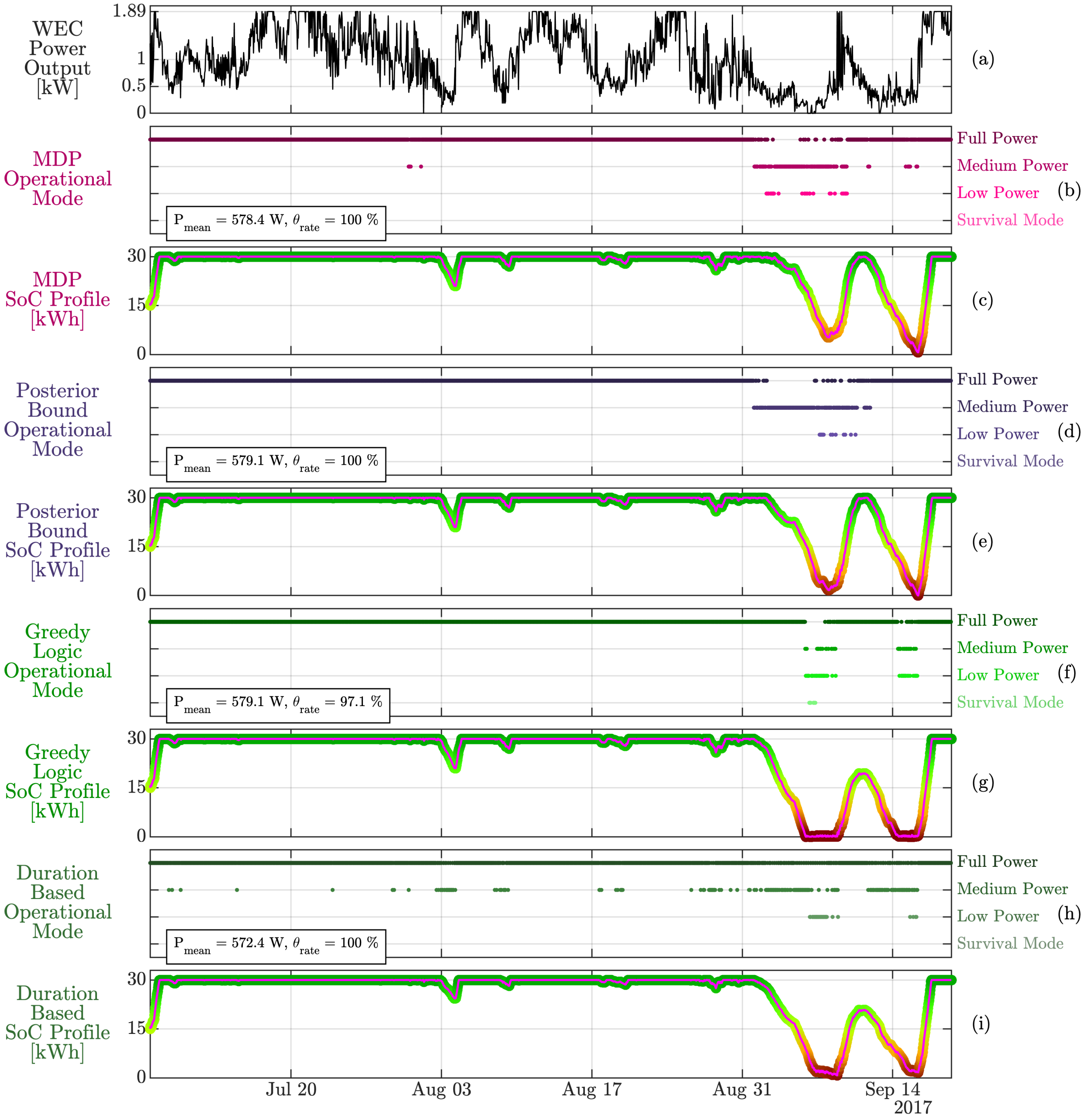

Figure B.4: Time series, over the entire simulation window, of (a) WEC power output, operational mode, and battery state of charge of forward simulations under (b, c) MDP, (d, e) Posterior Bound, (f, g) Greedy, and (h, i) Duration-Based decision-making. Annotations show two performance metric values: mean power consumption (P_{mean}) and theta rate (θ_{rate}) for each decision schema. The pink lines (c, e, g, i) show the discretization validation discussed in Appendix B.1.

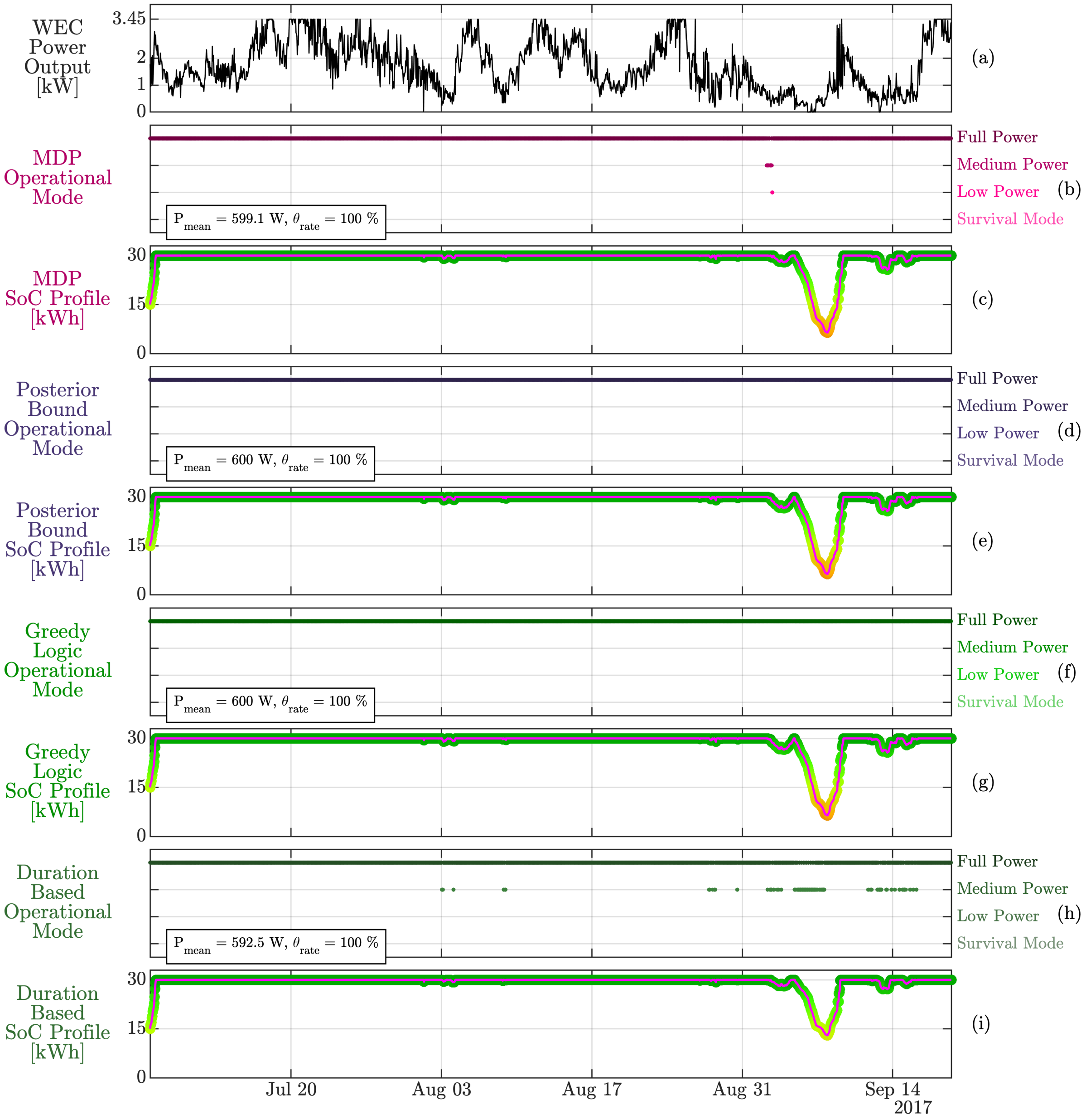

Figure B.5: Time series, over the entire simulation window, of (a) WEC power output, operational mode, and battery state of charge of forward simulations under (b, c) MDP, (d, e) Posterior Bound, (f, g) Greedy, and (h, i) Duration-Based decision-making. Annotations show two performance metric values: mean power consumption (P_{mean}) and theta rate (θ_{rate}) for each decision schema. The pink lines (c, e, g, i) show the discretization validation discussed in Appendix B.1.

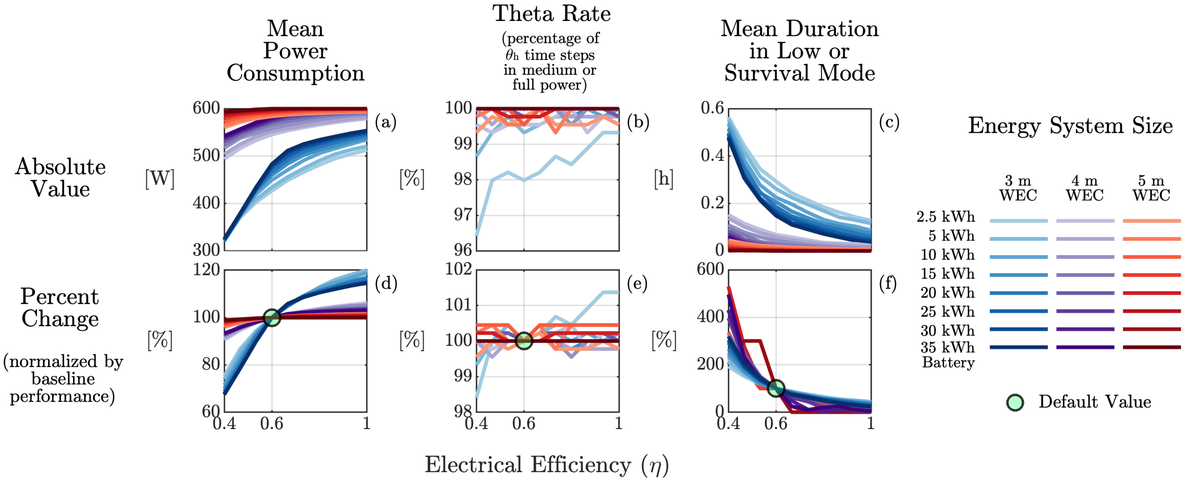

Figure B.6: MDP performance sensitivity to electrical conversion efficiency (η) used in Equation 2.18 (x-axes) in terms of (a,b) mean power consumption, (b,e) theta rate and (c,f) mean duration in low or survival mode. Performance is shown as (a-c) absolute and (d-e) percent changes, determined by normalizing the sensitivity output by baseline performance (i.e., when $\eta = 0.6$). Combinations of WEC size and battery capacity are indicated by coloration, with the primary distinction between WEC size and increasing storage capacities represented as darker shading within that color scheme. The default sensitivity value ($\eta = 0.6$) is indicated by the filled circle in the percentage change representations (d-e).

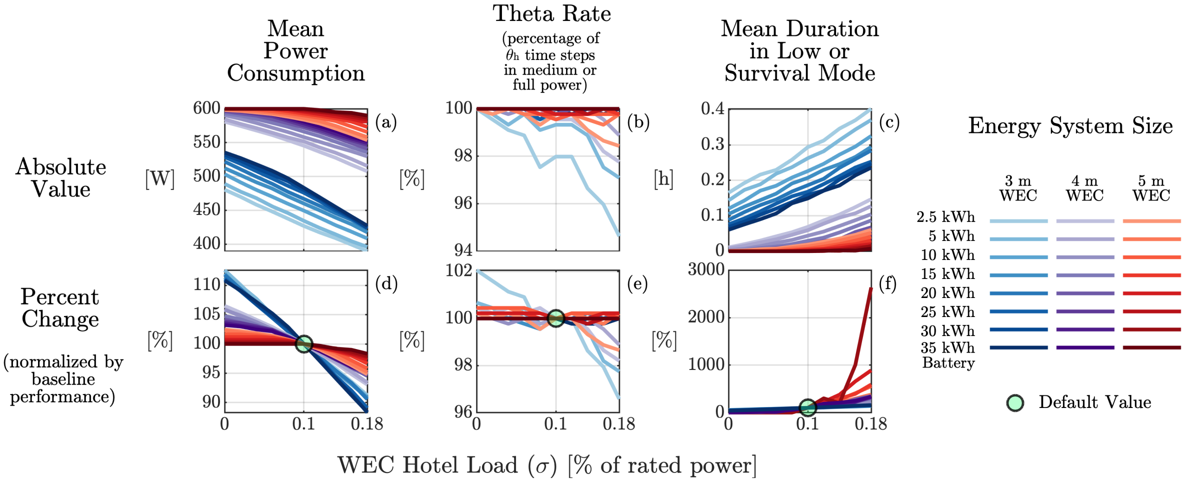

Figure B.7: MDP performance sensitivity to the percent of the WEC's rated power allocated for hotel loads (σ) used in Equation 2.18 (x-axes) in terms of (a,b) mean power consumption, (b,e) theta rate and (c,f) mean duration in low or survival mode. Performance is shown as (a-c) absolute and (d-e) percent changes, determined by normalizing the sensitivity output by baseline performance (i.e., when $\sigma = 10\%$). Combinations of WEC size and battery capacity are indicated by coloration, with the primary distinction between WEC size and increasing storage capacities represented as darker shading within that color scheme. The default sensitivity value ($\sigma = 10\%$) is indicated by the filled circle in the percentage change representations (d-e).

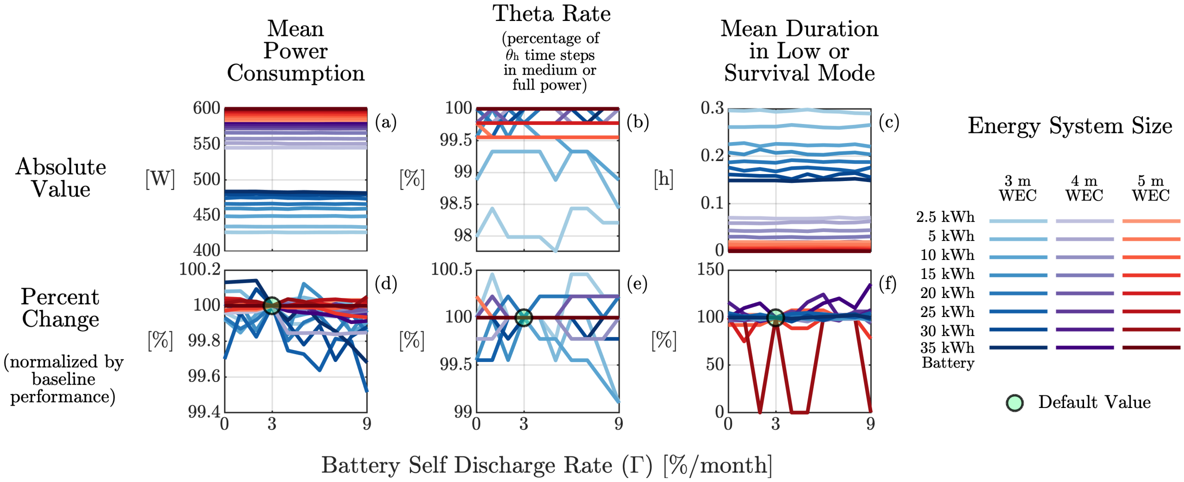

Figure B.8: MDP performance sensitivity to the self-discharge rate of the battery (Γ) used in Equation 2.12 (x-axes) in terms of (a,b) mean power consumption, (b,e) theta rate and (c,f) mean duration in low or survival mode. Performance is shown as (a-c) absolute and (d-e) percent changes, determined by normalizing the sensitivity output by baseline performance (i.e., when $\Gamma = 3\%$ loss per month). Combinations of WEC size and battery capacity are indicated by coloration, with the primary distinction between WEC size and increasing storage capacities represented as darker shading within that color scheme. The default sensitivity value ($\Gamma_h = 3\%$ loss per month) is indicated by the filled circle in the percentage change representations (d-e).

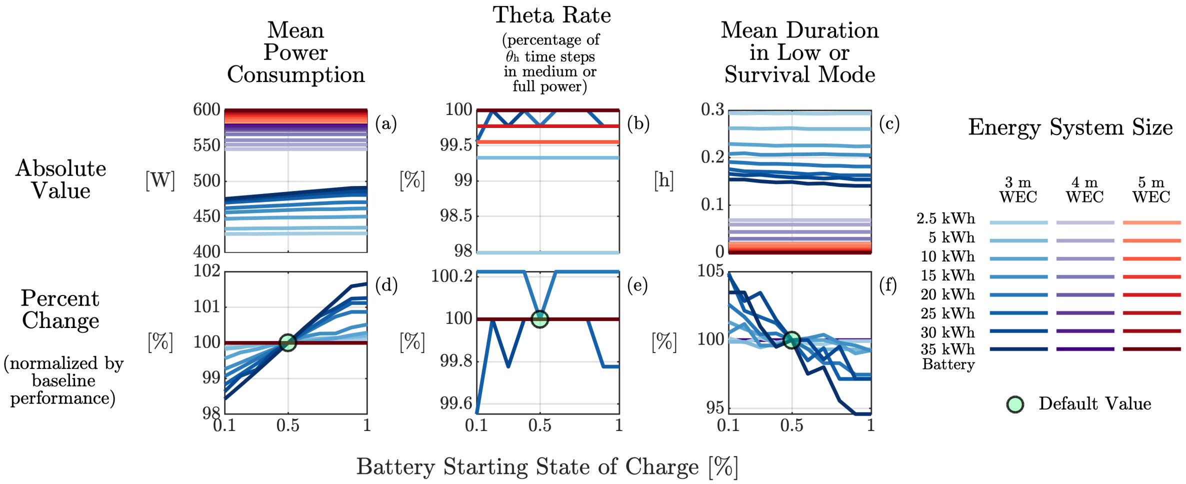

Figure B.9: MDP performance sensitivity to the starting charge of the battery (in percent relative to the battery's maximum capacity) in time-domain simulation (x-axes) in terms of (a,b) mean power consumption, (b,e) theta rate and (c,f) mean duration in low or survival mode. Performance is shown as (a-c) absolute and (d-e) percent changes, determined by normalizing the sensitivity output by baseline performance (i.e., when starting battery charge is 50%). Combinations of WEC size and battery capacity are indicated by coloration, with the primary distinction between WEC size and increasing storage capacities represented as darker shading within that color scheme. The default sensitivity value (50%) is indicated by the filled circle in the percentage change representations (d-e).

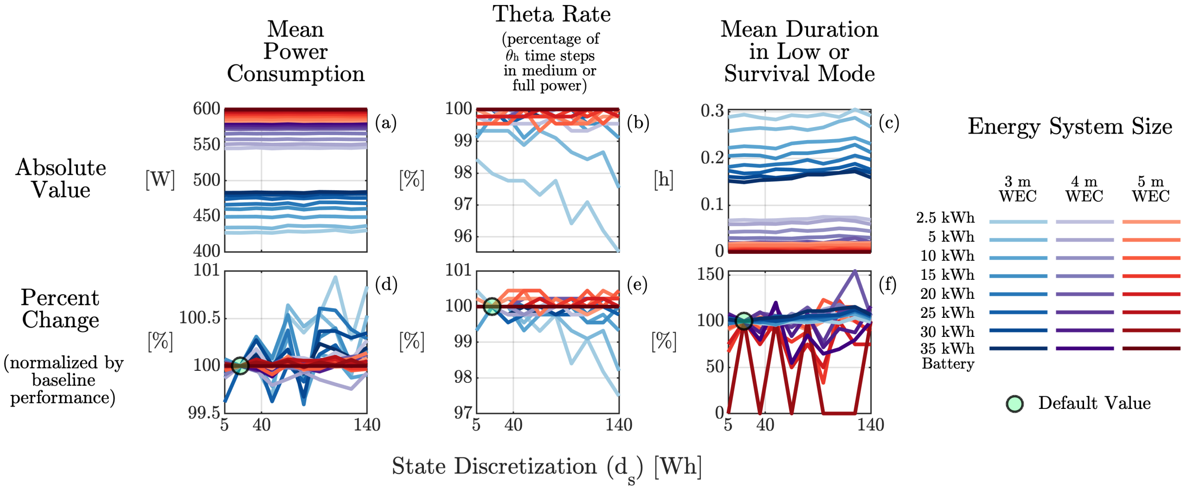

Figure B.10: MDP performance sensitivity to state space discretization (d_s) discussed in Section 3.3.1 (x-axes) in terms of (a,b) mean power consumption, (b,e) theta rate and (c,f) mean duration in low or survival mode. Performance is shown as (a-c) absolute and (d-e) percent changes, determined by normalizing the sensitivity output by baseline performance (i.e., when $d_s = 20$ Wh). Combinations of WEC size and battery capacity are indicated by coloration, with the primary distinction between WEC size and increasing storage capacities represented as darker shading within that color scheme. The default sensitivity value ($d_s = 20$ Wh) is indicated by the filled circle in the percentage change representations (d-e).

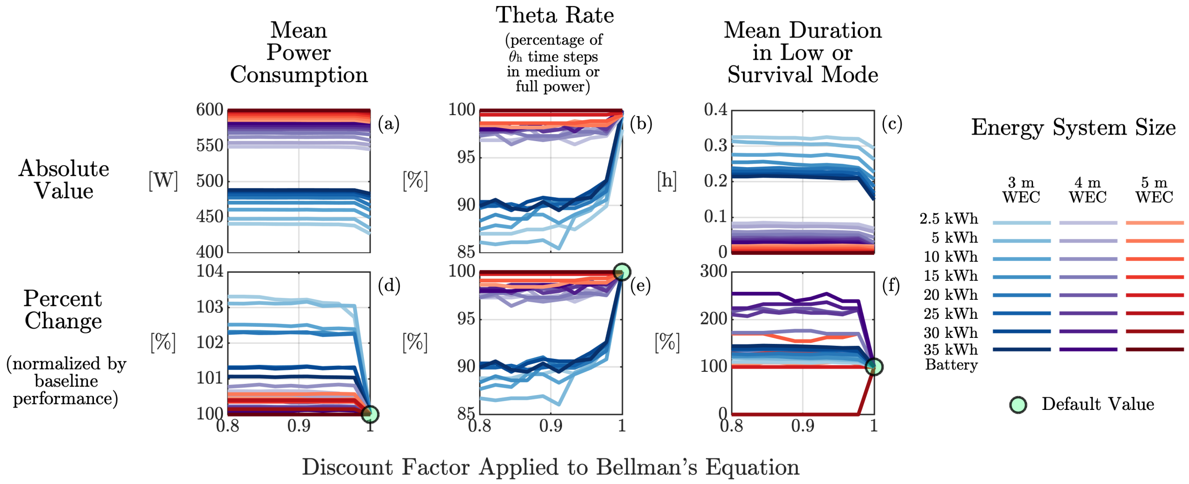

Figure B.11: MDP performance sensitivity to discount factor (α) used in Equation 3.6 (x-axes) in terms of (a,b) mean power consumption, (b,e) theta rate and (c,f) mean duration in low or survival mode. Performance is shown as (a-c) absolute and (d-e) percent changes, determined by normalizing the sensitivity output by baseline performance (i.e., when $\alpha = 1$). Combinations of WEC size and battery capacity are indicated by coloration, with the primary distinction between WEC size and increasing storage capacities represented as darker shading within that color scheme. The default sensitivity value of α is 1, meaning its default setting is to have no influence on the objective function (Equation 3.6). This value is indicated by the filled circle in the percentage change representations (d-e).

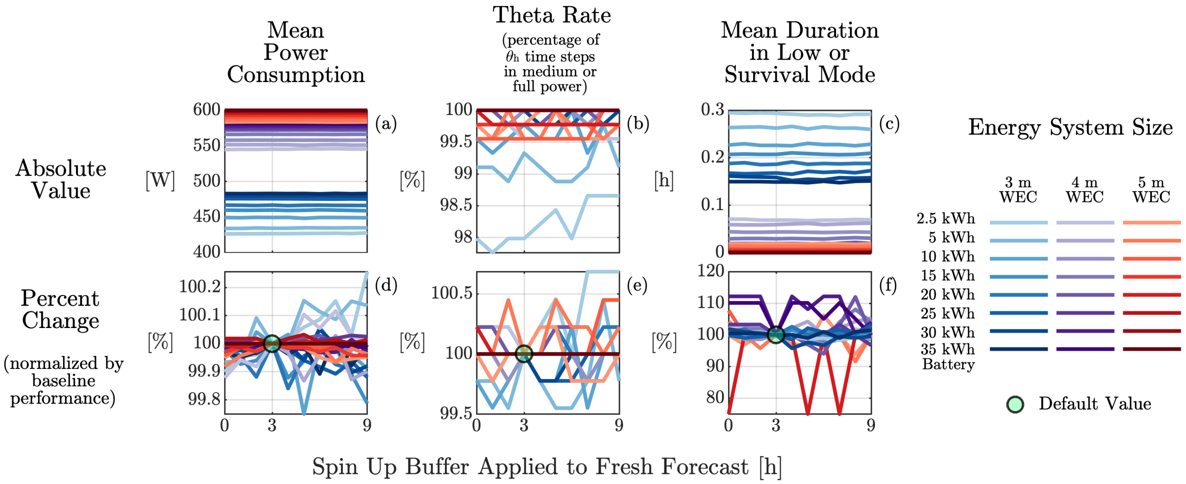

Figure B.12: MDP performance sensitivity to the spin-up buffer used to compensate for the forecast artifact discussed in Section 3.2.2 (x-axes) in terms of (a,b) mean power consumption, (b,e) theta rate and (c,f) mean duration in low or survival mode. Performance is shown as (a-c) absolute and (d-e) percent changes, determined by normalizing the sensitivity output by baseline performance (i.e., when spin-up buffer is 3 h). Combinations of WEC size and battery capacity are indicated by coloration, with the primary distinction between WEC size and increasing storage capacities represented as darker shading within that color scheme. The default sensitivity value (spin-up buffer of 3 h) is indicated by the filled circle in the percentage change representations (d-e).